The Dissertation Committee for Hari Sai Ganesh
certifies that this is the approved version of the following dissertation:

Modeling, Control, and Optimization of an Industrial Austenitization Furnace

Committee:

Michael Baldea, Supervisor

Thomas F. Edgar, Co-Supervisor

Gary T. Rochelle

Ofodike A. Ezekoye

Modeling, Control, and Optimization of an Industrial Austenitization Furnace

by

Hari Sai Ganesh

DISSERTATION

Presented to the Faculty of the Graduate School of

The University of Texas at Austin

in Partial Fulfillment

of the Requirements

for the Degree of

DOCTOR OF PHILOSOPHY

THE UNIVERSITY OF TEXAS AT AUSTIN

December 2018

Dedicated to my family, relatives, friends, and people in Trivandrum, the evergreen city of India, who shaped my life and spirit.

Acknowledgments

First and foremost, I would like to express my deepest gratitude to my supervisors Dr. Michael Baldea and Dr. Thomas F. Edgar for their support and able guidance. I consider myself extremely fortunate to have them as my advisers, who are not only great scholars and researchers but also great managers and great people to work with.

I thank my group mates, who where there to extend any help related to work and who also made my time here a pleasurable experience. I especially want to thank alumnus Vincent R. Heng, who laid a strong foundation for this project, which helped me tremendously in building on and completing the work before the end date.

I thank the Department of Energy for funding this work under the research grant DE-EE0005763: "Industrial Scale Demonstration of Smart Manufacturing ('SM') Achieving Transformational Energy Productivity Gains". It was an absolute pleasure working with an inter-disciplinary team, consisting of personnel from manufacturing plants, software engineers, and academicians from other universities and disciplines. This experience helped me in honing both my analytical skills and soft skills like group discussion and presentation.

I want to thank Dr. Ofodike A. Ezekoye for helping me with radiation modeling and Dr. Eric M. Taleff for helping with modeling microstructure

changes in parts during heating and their consequent effects on the metallurgical properties. Both of them are professors in the mechanical engineering department here at UT Austin. I also want to thank Dr. Prakashan Korambath and Dr. Jim Davis from the Institute of Digital Research and Education, UCLA, with whom I worked on demonstrating how the manufacturing industry can take advantage of cloud computing technologies for managing data and models for smart manufacturing without having to deploy an on-premise computing cluster.

The seminars and presentations on campus helped a great deal in enhancing my knowledge and broadening my perspective. I like to specifically mention the weekly seminars organized by the UT Energy Institute and those in our department.

Finally, I am grateful to Dr. Gary T. Rochelle and Dr. Ofodike A. Ezekoye for agreeing to serve on my thesis committee.

Modeling, Control, and Optimization of an Industrial Austenitization Furnace

Publication No. _____

Hari Sai Ganesh, Ph.D.
The University of Texas at Austin, 2018

Supervisors: Michael Baldea
Thomas F. Edgar

Steel production and processing is both energy-intensive (2% of overall energy consumption) and one of the biggest contributors to CO_2 emissions. Its use is projected to increase by 1.5 times that of present levels (around 1.6 billion metric tonnes per year) by 2050 to meet the needs of a growing population. The main goal of this research is to minimize the energy consumption of a steel quench hardening (or heat treating) process, currently in operation at an industrial partner, by mathematical modeling, optimization, advanced control, and heat integration.

The quench hardening processes consists of heating pre-finished metal parts to a certain temperature in a continuously operating furnace (austenitization), followed by rapid cooling (quenching) in water, brine or oil to induce desired metallurgical properties like hardness, toughness, shear strength, tensile strength, etc. The novelty of this work lies in the two-scale modeling

approach considered to solve the furnace energy consumption minimization problem. We improve a previously developed two-dimensional (2D) physics-based model of the heat treating furnace that computes the energy usage of the furnace and the part temperature distribution as a function of time and position within the furnace under temperature feedback control. We predict the effect of process variables on microstructural evolution of the parts using an empirical relation reported in the literature and their consequent effects on the metallurgical properties of the quenched product. The physics-based model combined with the empirical model is used to simulate the furnace operation for a batch of parts processed sequentially under heuristic temperature set points with a simple linear control strategy suggested by the operators of the plant. We then minimize the energy consumption of the furnace without compromising the product quality by real-time optimization (RTO), model predictive control (MPC), and heat integration using radiant recuperators. Energy savings of 3.7%, 15.93%, and 20.88% were obtained under model predictive control, heat integration, and optimized set points respectively compared to reference heuristic operation case without heat integration and MPC.

Table of Contents

List of Tables

List of Figures

xiv

Chapter 1

Introduction

This chapter is based on material published in papers "V. R. Heng, H. S. Ganesh, A. R. Dulaney, A. Kurzawski, M. Baldea, O. A. Ezekoye, and T. F. Edgar. Energy-oriented modeling and optimization of a heat treating furnace. Journal of Dynamic Systems, Measurement, and Control, 139(6):061014, 2017" [48] and "H. S. Ganesh, T. F. Edgar, and M. Baldea. Modeling, optimization and control of an austenitization furnace for achieving target product toughness and minimizing energy use. Journal of Process Control, 2017. doi: 10.1016/j.jprocont.2017.09.008" [36]. In Heng *et al.* [48], I developed the dynamic burner model, improved the part model, ran the furnace simulations and analyzed the results. I am the primary contributor of paper Ganesh *et al.* [36].

1.1 Background and motivation

Steel is an iron-carbon alloy containing between 0.02% to 2% carbon, not found in nature but produced in bloomery furnaces for thousands of years [18, 58]. The earliest known production of steel are the ironware pieces unearthed from Anatolia in Turkey that are about 4000 years old, dating from 1800 BC [3]. Prior to the industrial revolution, steel was very expensive to

produce and hence it was mostly used in small expensive items such as swords, armour and cutlery; all large metal structures were made of wrought or cast iron. A new era of mass-production of steel began in late 1850s as a result of Henry Bessemer's development of the *Bessemer converter* [14, 103, 106, 126]. Since then, steel has been basic to the world's industrial economy with applications in infrastructure, buildings, ships, automobiles, tools, machines, appliances, and weapons [6, 76, 142]. Today, steel is one of the most common materials used in the world with production of around 1.6 billion metric tonnes per year [137]. Due to the population growth and increased global wealth, predictions for steel use show a 50% increase from the present levels by 2050 [8].

Manufactured steel that is cooled at a slow rate is quite soft and is not ideal for many applications. Steel parts are thus often heat treated to induce desired metallurgical properties such as hardness, toughness, shear strength and tensile strength [18, 43, 124, 128]. Hardness and strength are typically improved via quench hardening, a heat treating process which consists of heating finished or pre-finished parts to a specific temperature (inducing austenitization) in an inert atmosphere (to prevent surface oxidation), followed by rapidly quenching in oil or water to introduce a hardened phase called *martensite* [10, 68, 102, 128]. Martensitic steel is highly resistant to deformation, a property desired in many applications. The austenitization step in the quench hardening process consumes significant amounts of energy (typically natural gas) to heat the parts from ambient temperature to about 1050 K [124].

In the United States, the metal processing industry is the fourth largest industrial user of energy with yearly demands of 2 quadrillion BTU (quads), which is roughly 2% of the overall domestic energy consumption (100 quads) [120, 131, 133]. For an individual steel processing plant, reheating and heat treating furnaces account for 65% to 80% of the overall energy use [92, 123]. The energy use is intensified by inherent furnace inefficiencies (20%-60%) and ineffective control strategies [123]. Part temperatures, especially the core, cannot be sensed and measured. Hence, in practice, the operators tend to overheat the parts such that a minimum temperature threshold required for processing is reached, thereby causing excess fuel consumption. Another reason for overheating is that even if only some portions of the fabricated part are not heated sufficiently, then the entire part will not meet the quality standards resulting in waste. Therefore, the monetary gain in energy minimization while heating will be counter-balanced by the loss due to scrapping of defective parts. The temperature sensing limitations, combined with high energy usage make austenitization furnace a primary target for advanced model-based reconfiguration, optimization, and control.

1.2 Literature review

During the heat treating process, the part temperature increases, the phase transformation of steel to austenite takes place, and there are microstructural changes depending on the temperature and the rate of heating. All these phenomena determine the metallurgical properties of the quenched

3

product. The heat treating process has been studied both at the macroscopic level (i.e., furnace and part length-scales) and at the microscopic level, considering the microstructural evolution of the parts.

At the **macroscopic** level, several furnace modeling studies [11, 54, 66, 86, 117, 132, 140, 143] have focused on determining the temperature profile of the parts as a function of time (and position) in the furnace.

Many studies on metal processing furnaces are focused on pusher-type slab reheating systems (e.g., Ramamurthy *et al.* [98]). Although reheating furnaces are geometrically similar to heat treating furnace considered in this work, the parts processed in reheating furnaces are heated directly, whereas during heat treating, the parts are heating indirectly by radiant tube burners. Therefore, while developing mathematical models for direct-fired reheating furnaces, gas-to-surface radiation interactions must be considered, whereas in indirect-fired heat treating furnaces, as will be discussed later, these interactions are negligible and the predominant mode of heat transfer is surface-to-surface radiation. Since reheating is a pre-finishing step, contact between parts (or slabs) are allowed. On the other hand, heat treating is done to harden finished parts. Hence, parts are placed at some distance from each other. As a consequence, surface-to-surface radiation interactions between like surfaces are critical and must be captured by the models along with those between burner and part surfaces.

In addition to capturing long-range, non-linear radiation interactions, complex furnace and part geometries add to the modeling challenges. Hence,

4

modeling efforts reported in the literature have followed three main approaches:

1. **Data-driven modeling**

   Liao *et al.* [74] predicted the furnace tempeture with respect to varying operating conditions using a neural network algorithm. However, temperature of the workpieces (or slabs) as a function of time or position and the energy consumed by the system were not calculated. Xuegang *et al.* [139], Kim *et al.* [64], and Laurinen and Röning [70] followed a similar path, and proposed using pattern swarm and particle swarm optimization to train neural network and principal component analysis to reduce model dimensionality. Since parts are heated usually beyond 1000 K, the part temperatures, especially the interiors, cannot be sensed directly. Therefore, completely data-driven models such as neural-networks typically cannot accurately predict the part temperatures when measurements are unavailable. This is a significant drawback of this modeling approach since inhomogeneous part temperature distribution determines the quality of the furnished product [89].

2. **High-fidelity modeling**

   Tang *et al.* [122] and Triebl *et al.* [129] used Computational fluid dynamics (CFD) to predict part and blanket gas temperature distribution for a pusher-slab furnace. Pan *et al.* [89] calculated details such as thermal stresses of parts during heating and phase transformation of steel into

their different allotropes. Although CFD simulations can predict the dynamics and the temperature distribution of furnace systems with good accuracy, they are computationally expensive. It can take several days of simulation time to finish the calculations, even with high-performance computing clusters. Moreover, details such as blanket gas velocity profiles and flow patterns are not required in applications intended in this work such as real-time temperature control and optimal energy management. This modeling approach would be ideal for detailed design of furnaces. However, in this work, the high computation costs involved limit the use of such models.

3. **Equation-oriented modeling**

It is a semi-empirical modeling approach, wherein the model equations are based on the underlying physics but with several assumptions and approximations to reduce computational costs. Balbis *et al.* [11] predicted the part temperature at furnace exit by discretizing the furnace into a series of control volumes, disregarding long-range heat interactions. In the work of Yang and Yu [140], a linearized version of the radiation heat transfer relations was used and the measurements from the top and bottom regions of the furnace were combined into a single variable. Steinboeck *et al.* [117] assumed the part temperature profile to be one-dimensional and used a Galerkin-based approach to predict product temperature values. Yoshitani *et al.* [143], Mochida *et al.* [80], and Kang *et al.* [60] simplified radiation relationships by either neglecting long-range

interactions or using empirical coefficients obtained from experimental results lumped into the emissivity term in the radiation heat transfer terms in the energy balance equations. These type of semi-empirical models are developed for on-line control and optimization applications. However, note that the simplifications such as omitting long-range radiation can result in inaccurate predictions. These simplifications are not valid in this work where long-range surface-to-surface radiation is the dominant mode of heat transfer.

Several other studies have focused exclusively on the **microstructural** changes and their effect on mechanical properties [7, 71, 75, 104] without considering the furnace dynamics. Liu *et al.* [75] used finite-element analysis tools to study the metallo-thermo-mechanical behaviors during heat treatment of a part. The review article by Roters *et al.* [104] details the application of crystal plasticity finite-element analysis for predicting the microstructure based mechanical properties of heterogeneous crystalline matter. Anelli [7] reported constitutive relations that predict microstructural changes as a function of specific thermal evolution to simulate hot rolling and controlled cooling of wire rods and bars. In the work of Lee and Lee [71], the effect of alloying elements on austenite grain size (AGS) was investigated and an empirical relation for predicting the AGS was proposed for global low alloy steels.

We note that, to date, the two length scales have not –to our knowledge– been considered simultaneously. The novelty of this work lies in the considered two-scale modeling approach wherein we capture both the dominating

radiation interactions as well as the microstructural changes when optimizing the energy input to the furnace system to ensure that the quality targets of the quenched product are met.

1.3   Guide to chapters

The rest of the dissertation is organized as follows.

In Chapter 2, we describe the system considered in this work, an austenitization furnace, currently in operation at an industrial partner and develop a semi-empirical model of the furnace. The furnace operates in a continuous manner under temperature feedback control. The furnace temperatures exceed 1000 K. Therefore, long-range radiation is the dominant mode of heat transfer. Moreover, when parts are heated, in addition to the changes in temperature, the microstructure also changes. This has consequences in the metallurgical properties of the quenched product. Therefore, the model we developed captures the physics at both the aforementioned length scales: long-range radiation and microstructure transformation.

In Chapter 3, we present the optimization problem that aims to identify the operating conditions of the furnace that minimize the total energy consumption without compromising product quality. The parts must be heated past the desired threshold with minimal inhomogeneous temperature variations with the part. There is also a constraint on the microstructure changes to ensure desired metallurgical properties of the quenched product. Surrogate models are used for solving the optimization problem to greatly reduce

computation costs.

In Chapter 4, we develop and deploy model predictive control (MPC) as a supervisory control strategy for on-line optimization of the furnace operation. The inner-level feedback controller maintains the conditions of the furnace close to the set points. The supervisory MPC controller calculates the optimal set points of the feedback controller at each time instant of the MPC controller (longer than that of the feedback controller) that would drive the product conditions close to their respective lower bounds.

In Chapter 5, we estimate the fuel reduction in the system due to heat integration using recuperators, a special purpose feed-effluent heat exchangers. Furnace simulations and observations in the plant indicate that a considerable amount of energy input to the system is wastefully discharged in the burner exhaust. This heat loss is minimized by transferring some of the exhaust heat to pre-heat inlet air to the burners, thus reducing the amount of fuel required for combustion. The temperatures of exhaust gases are usually greater than 1000 K. Hence, radiation is the dominant mode of heat transfer in the recuperator. We model a concentric-tube recuperator, capturing local convection and geometry-dependent, long-range radiation.

Finally, future directions are recommended and conclusions are drawn in Chapter 6.

Chapter 2

Austenitization furnace modeling

This chapter is based on material published in papers "V. R. Heng, H. S. Ganesh, A. R. Dulaney, A. Kurzawski, M. Baldea, O. A. Ezekoye, and T. F. Edgar. Energy-oriented modeling and optimization of a heat treating furnace. Journal of Dynamic Systems, Measurement, and Control, 139(6):061014, 2017" [48] and "H. S. Ganesh, T. F. Edgar, and M. Baldea. Modeling, optimization and control of an austenitization furnace for achieving target product toughness and minimizing energy use. Journal of Process Control, 2017. doi: 10.1016/j.jprocont.2017.09.008" [36]. In Heng *et al.* [48], I developed the dynamic burner model, improved the part model, ran the furnace simulations and analyzed the results. I am the primary contributor of paper Ganesh *et al.* [36].

2.1 Process and system description

The heat treating furnace considered in this work operates in a continuous manner under temperature feedback control. A prototype furnace schematic for heat treating furnace based on an AFC Holcroft [50] system in operation at an industry partner is shown in Figure 2.1. The finished or pre-finished metal parts are loaded onto trays and placed on a conveyor belt

that transports the parts through the furnace, which is heated indirectly by natural gas-fired radiant U-tube burners located on the ceiling and the floor (see Figure 2.2 for burner schematic). The parts are immediately quenched in an oil bath after exiting the furnace to to induce the crystal structure change and give the parts mechanical properties such as hardness, toughness, shear strength and tensile strength. Nitrogen, an inert blanket gas, introduced in the furnace to prevent surface oxidation, flows counter-current to the movement of the parts. Due to sensing limitations, the part temperatures are controlled indirectly by controlling the furnace temperature distribution - a scheme that is effectively open-loop with respect to part temperature control. The furnace is divided into four *temperature control zones* and the mass flow rates of fuel (natural gas) to all the burners of a zone are adjusted simultaneously to control the temperature of that particular zone. Long range zone-to-zone radiation interactions affect the temperatures of other zones as well when fuel flow rate of a particular zone is adjusted. The furnace operates at temperatures in excess of 1000 K and the residence time of the parts within the furnace is in the order of a few hours.

2.2 Macroscopic model: prediction of part exit conditions and energy

Below, we present an overview of the two-dimensional (2D) model of the heat treating furnace developed in Heng *et al.* [48]. As the system operates at temperatures above 1000 K, radiation is the dominant mode of heat transfer
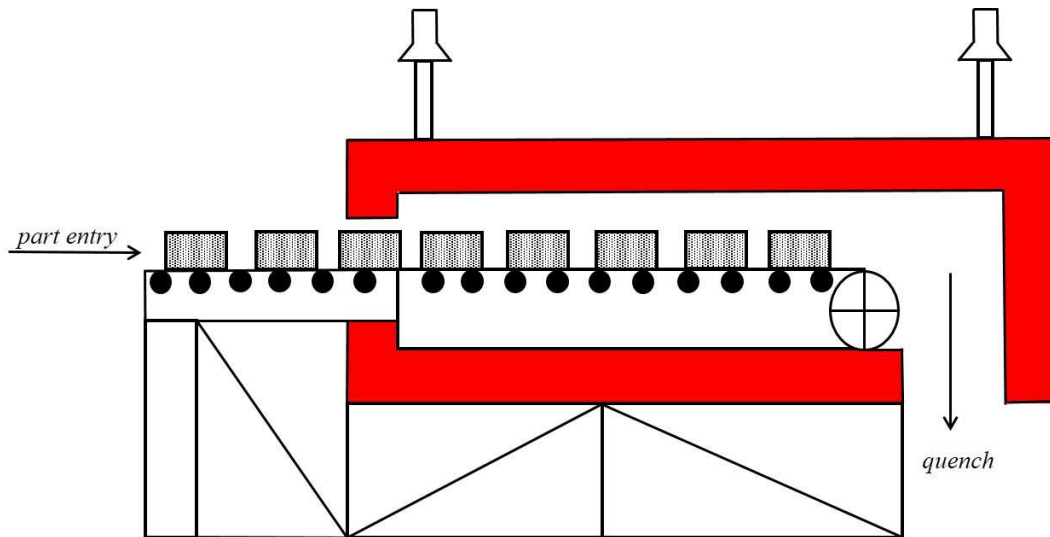
Figure 2.1: Prototype furnace schematic for roller hearth furnace based on schematic by AFC-Holcroft [50]. The hatched rectangles are the parts that are heated in the furnace.
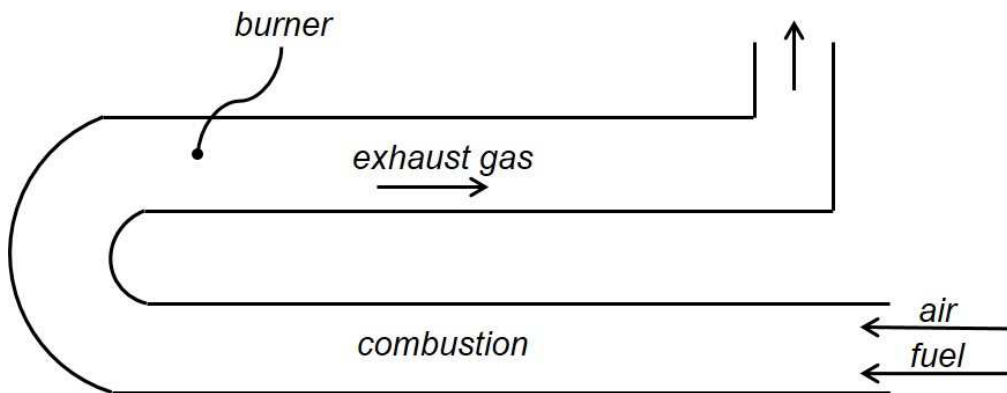
Figure 2.2: Schematic of U-tube burner where fuel (natural gas) is mixed with air for combustion. Heat from the burner is transferred indirectly to the parts in the furnace predominantly by radiation.

inside the furnace. In this radiation-based model, the furnace is discretized into three types of surfaces depending upon its geometric elements, namely, *burner*, *insulation* and *load* or *part*. A schematic of the discretized 2D furnace is shown in Figure 2.3. The geometric details of the furnace and the parts and physical properties used in this work are listed in Table 3.1. The following assumptions are made in developing the model:

2.2.1 Model assumptions

A.1 The mass of the conveyor belt is much lower than that of the parts. Hence, the conveyor belt is neglected in the model. Nevertheless, the movement of the parts within the furnace is captured.

A.2 In the industrial system, cylindrical with ogive top shaped parts are loaded onto a tray and placed on the conveyor belt. An idealized rectangular geometry with equivalent metal mass is considered for the ensemble of a tray and the parts in it and is referred to as a *part*.

A.3 Since nitrogen is a diatomic gas, there is no gas-to-surface radiation heat transfer [55]. The gas-to-surface heat transfer occurs only through convection and surface-to-surface heat transfer occurs only through radiation.

A.4 For modeling purposes, the furnace is discretized into a series of *control volumes* for calculating the gas temperature profile along the length of the furnace. There is no spatial variation in the nitrogen temperature

within a control volume.

While the parameters of our model are based on literature values, we note that, in practice, they could be estimated based form data: the zone temperatures can be measured as a function of time using thermocouples placed on the middle insulation surfaces of each zones, while the part temperature distribution at the exit of the furnace can also be measured by non-contact ultra sonic measurements [69, 107, 135].

2.2.2 Overall energy balance relations

The overall energy balance of surface i in the furnace is given by the expression:

$$Q_{net,i} = Q_{radiation,i} + Q_{convection,i} \quad i = 1, \ldots, N \tag{2.1}$$

where N is the total number of surfaces. Note that N changes as the parts enter and exit the furnace. $Q_{net,i}$ is the overall heat transfer rate for surface i, $Q_{radiation,i}$ is the radiation heat transfer rate for surface i and $Q_{convection,i}$ is the convective heat transfer rate for surface i. The radiation heat transfer, $Q_{radiation,i}$, is given by the following expressions [55]:

$$Q_{radiation,i} = \frac{\sigma T_i^4 - J_i}{\frac{1-\epsilon_i}{\epsilon_i A_i}} \tag{2.2}$$

$$Q_{radiation,i} = \sum_{j=1}^{N} \frac{J_i - J_j}{(A_i F_{i,j})^{-1}} \tag{2.3}$$

where σ is the Stefan-Boltzmann constant, T_i is the temperature of surface i, J_i is the radiosity of surface i, ϵ_i is the emissivity of surface i, A_i is the area of surface i, and $F_{i,j}$ is the view factor from surface i to surface j. View factor $F_{i,j}$ is defined as the fraction of the radiation that leaves surface j and strikes surface i. Radiosity J_i is defined as the net amount of heat flux leaving surface i via radiation.
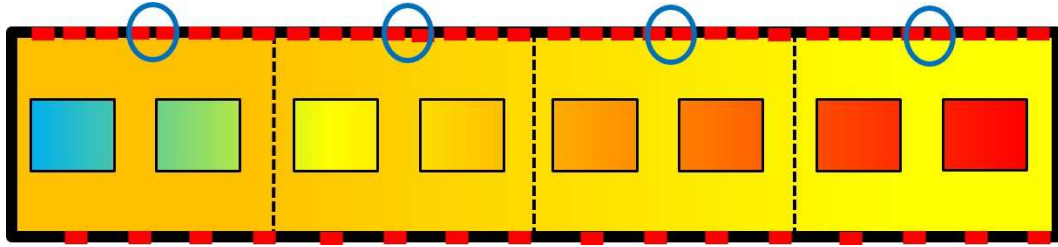
Figure 2.3: The schematic of the 2D model of the austenitization furnace (side view). The red and black lines on the furnace wall represent burner and insulation surfaces respectively. The rectangles within the furnace are the parts that are heated in the furnace. Each side of a part is a load or part surface. Cold parts enter from the left hand side of the furnace schematic and hot parts exit from the right hand side. Nitrogen, the inert gas, flows counter-current to the direction of movements of the parts. The furnace is divided into four control zones. The vertical dotted lines represent the boundaries between subsequent zones. The insulation surfaces that are circled host the temperature sensors for zone temperature control.

2.2.2.1 Burner

For burner surfaces, the first expression of the radiation term eq. (2.2) is substituted into the overall energy balance eq. (2.1) to yield:

$$Q_{net,i} - h_{furn} A_i (T_i - T_w^\infty) = \frac{\sigma T_i^4 - J_i}{\frac{1-\epsilon_i}{\epsilon_i A_i}} \qquad (2.4)$$

where h_{furn} is the furnace heat transfer coefficient and T_w^∞ is the temperature of nitrogen gas in control volume w. The surface i to gas control volume w convective heat transfer is captured by the term: $h_{furn} A_i (T_i - T_w^\infty)$. The furnace heat transfer coefficient, h_{furn}, is calculated from a Nusselt number correlation for forced convection in turbulent pipe flow [55]:

$$Re = \frac{\rho_{N_2} u_{N_2} A}{D_h \, \mu} \qquad (2.5)$$

$$Nu = 0.023 \, Re^{0.8} \, Pr^{0.4} \qquad (2.6)$$

$$h_{furn} = \frac{k_{N_2} \, Nu}{D_h} \qquad (2.7)$$

$$D_h = \frac{4A}{P} \qquad (2.8)$$

where Re is the Reynolds number, Pr is the Prandtl number, D_h is the hydraulic diameter, ρ_{N_2} is the density of nitrogen, u_{N_2} is the velocity of nitrogen, μ is the viscosity of nitrogen, k_{N_2} is the thermal conductivity of nitrogen, A is the cross sectional area of the furnace perpendicular to mass flow, and P is the wetted perimeter of the cross-section. Since the model is two dimensional, the hydraulic diameter D_h is the length of the cross-section (or the height)

of the furnace. The Prandtl number, Pr, is assumed to be a property of the gas [55].

For burner surfaces, the surface temperature and heat duty are input variables. To compute the heat duty, $Q_{net,i}$, and burner surface temperature T_i, we use a dynamic burner model based on the work of Niederer et al [87]. In this model, the dynamics of the burner walls are included, and they are approximated with a system of differential algebraic equations (DAE). The model considers two gases, the inlet gas (IG) to the burner, containing $[CH_4, O_2, N_2] \in IG$, and outlet gas (OG), containing $[CO_2, H_2O, O_2, N_2] \in OG$. The IG and OG capture the components involved in the combustion of methane in air, governed by the equation $CH_4 + 2O_2 \rightarrow CO_2 + 2H_2O$, where N_2 is an inert gas which does not contribute to the reaction. We assume fuel-lean operation, such that all methane is consumed.

The heat to the burner provided by the inlet gases is the heat of formation less the specific enthalpy of the gases, given by the following equation [87]:

$$Q_{IG} = \sum_{\xi \in IG} \frac{\dot{m}_\xi}{MW_\xi} (\Delta H_{form,\xi} - \bar{h}^{Ent}(\xi, T_{IG})) \tag{2.9}$$

where $\dot{m}_\xi$ is the mass flow rate, MW_ξ is the molecular weight, $\Delta H_{form,\xi}$ is the heat of formation, and $\bar{h}^{Ent}(\xi, T_{IG})$ is the specific enthalpy, all for gas $\xi \in IG$. In this equation, it is assumed the temperature of the inlet gases, T_{IG} is known a priori.

Similarly, the heat out the exhaust in the outlet gases OG, is given by the following equation [87]:

$$Q_{OG} = \sum_{\eta \in OG} \frac{\dot{m}_\eta}{MW_\eta}(\Delta H_{form,\eta} - \bar{h}^{Ent}(\eta, T_{OG})) \qquad (2.10)$$

which is equivalent equation to Equation (2.9) for gases $\eta \in OG$. We assume that stoichiometric amounts of CO_2 and H_2O were formed after CH_4 is consumed. The heat that leaves the burner, Q_{burner}, is given by:

$$Q_{burner} = Q_{IG} - Q_{OG} - V_{burner}\rho_{burner}C_{p,burner}\frac{dT_{burner}}{dt} \qquad (2.11)$$

The change in the burner wall temperature, T_{burner}, and the outlet gas temperature, T_{OG}, are represented by the following equations:

$$
\begin{aligned}
V_{burner}\rho_{burner}C_{p,burner}\frac{dT_{burner}}{dt} &= h_{OG}A(T_{OG} - T_{burner}) \\
&\quad + \gamma\,\sigma(T_{OG}^4 - T_{burner}^4) - Q_{burner}
\end{aligned}
\qquad (2.12)
$$

$$
\begin{aligned}
V_{OG}\rho_{OG}C_{p,OG}\frac{dT_{OG}}{dt} &= -h_{OG}A(T_{OG} - T_{burner}) \\
&\quad - \gamma\,\sigma(T_{OG}^4 - T_{burner}^4) \\
&\quad + \sum_{\xi \in IG}\frac{\dot{m}_\xi}{MW_\xi}(T_{IG} + \Delta H_{form,\xi}) \\
&\quad - \sum_{\eta \in OG}\frac{\dot{m}_\eta}{MW_\eta}T_{OG}
\end{aligned}
\qquad (2.13)
$$

18

$$\gamma = 1 - \exp(\alpha \, L_{mb}) \tag{2.14}$$

where the $_{burner}$ subscript denotes burner wall characteristics (density, heat capacity, temperature, volume and heat). h_{OG}, σ, α, L_{mb} and A represent the average heat transfer coefficient of outlet gas, the Stefan-Boltzmann constant, the absorptivity of the burner wall, the mean beam length of the radiating outlet gas in the burner and the surface area of the burner wall respectively. The mean beam length, L_{mb}, was calculated based on the assumption that the burner tubes are perfect cylinders with a constant diameter. Defining a ratio of the heat capacities and densities of the outlet gas to the burner wall, $\epsilon = \frac{\rho_{OG} \, C_{p,OG}}{\rho_{burner} \, C_{p,burner}}$, and applying the limit as ϵ approaches zero yields the following equation for the rate of change of the outlet gas temperature:

$$
\begin{aligned}
0 = &-h_{OG}A(T_{OG} - T_{burner}) - \gamma \, \sigma(T_{OG}^4 - T_{burner}^4) \\
&+ \sum_{\xi \in IG} \frac{\dot{m}_\xi}{MW_\xi}(T_{IG} + \Delta H_{form,\xi}) - \sum_{\eta \in OG} \frac{\dot{m}_\eta}{MW_\eta} T_{OG}
\end{aligned}
\tag{2.15}
$$

which, when coupled with Equation (2.12), yields the DAE system that is solved to give T_{OG} and T_{burner} at each time step in the furnace, granting the model its dynamic nature. To improve computational efficiency, Q_{burner} used in Equation (2.12) is assumed to be from the previous time step of the furnace, and is considered constant for the time scale of the burner at each furnace iteration.

19

This burner model allows for simulations of the closed-loop control of the system to be performed as described later. We note that modeling radiant tube burners is a research topic in its own right [80, 127], and the assumptions made in this model are necessary in order to obtain a simple input/output burner model that is easily tractable in computational simulations.

2.2.2.2   Part and insulating wall

For insulation and part surfaces, $Q_{net,i}$ and T_i are output variables. For insulation surfaces, the second expression of the radiation term eq. (2.3) is substituted into the overall energy balance eq. (2.1) to yield:

$$Q_{net,i} - h_{furn}A_i\left(T_i - T_w^\infty\right) = \sum_{j=1}^{N} \frac{J_i - J_j}{\left(A_iF_{i,j}\right)^{-1}} \tag{2.16}$$

The equation for part surfaces are similar to that of insulation surfaces, except that the furnace heat transfer coefficient, h_{furn}, is replaced by the part heat transfer coefficient h_{part}:

$$Q_{net,i} - h_{part}A_i\left(T_i - T_w^\infty\right) = \sum_{j=1}^{N_s} \frac{J_i - J_j}{\left(A_iF_{i,j}\right)^{-1}} \tag{2.17}$$

For the heat transfer coefficient, h_{part}, calculation, the length scale, D_p, is the height of a part. The speed of the conveyor belt is much slower than the velocity of the blanket gas. Hence, the relative velocity of the gas with respect to a part is approximately equal to the velocity of the flowing nitrogen. The

equivalent equation for Reynolds number for flow over a part, Re_p, is given by:

$$Re_p = \frac{\rho_{N_2} u_{N_2} A}{D_p \mu}$$ (2.18)

The Nusselt number, Nu_p, and the heat transfer coefficient, h_{part}, for flow over a part are given by the following equations:

$$Nu_p = 0.158 \, Re_p^{0.66} \, Pr^{0.33}$$ (2.19)

$$h_{part} = \frac{k_{N_2} \, Nu_p}{D_p}$$ (2.20)

Note that the Nusselt number in Equation (2.19) is obtained from the empirical correlation for the flow over a square cylinder [55] since the part model is in 2D geometry.

The view factor matrix, $F_{i,j}$, is calculated using Hottel's crossed string method [26], detailed in section 2.2.3. Equations (2.4), (2.16) and (2.17) are solved using using a dual iterative numerical scheme explained in section 2.2.4 to obtain heat duties and surface temperatures of part and insulation surfaces. The calculated heat duties are used in the boundary conditions of the unsteady state heat equation to determine the insulating wall temperature distribution and the part temperature distribution for all the parts processed in the furnace.

The insulating wall has heat capacity and is modeled as a solid material with uniform thickness. The wall temperature distribution is calculated by solving the one-dimensional unsteady state heat equation by an implicit Euler finite difference scheme. The inner surface of the insulating wall boundary condition is:

21

$$Q_{net,i} = -k_{ins} A_i \frac{dT_i}{dx_i} \tag{2.21}$$

where $Q_{net,i}$ is the solution of the aforementioned radiation-based dual iterative numerical algorithm. k_{ins} is the thermal conductivity of insulating material (brick), A_i is the area of insulation surface i, T_i is the temperature of the inner surface of insulation i, and x_i is the distance in the inward direction perpendicular to the insulating surface i. The outer surface of the insulating wall boundary condition is the balance between heat conduction through the wall and the convective heat transfer between the surface and the ambient air:

$$k_{ins} A_i \frac{dT_{ins,out,i}}{dx_i} = -h_{air} A_i (T_{ins,out,i} - T_{air}) \tag{2.22}$$

where $T_{ins,out,i}$ is the temperature of the outer surface of insulating wall i and h_{air} and T_{air} are the convective heat transfer coefficient and the temperature respectively of the ambient air.

A part is assumed to be a uniform solid. The two-dimensional unsteady state heat equation is solved by a second-order accurate Crank-Nicolson finite difference numerical scheme. The net heat flux, $Q_{net,i}$, of the four surfaces encompassing a part are used to define the boundary conditions:

$$Q_{net,i} = -k_{part} A_i \frac{dT_i}{dn_i} \tag{2.23}$$

where k_{part} is the part thermal conductivity, T_i and A_i are the temperature

and area of part surface i respectively, and n_i is the distance in the inward direction perpendicular to part surface i.

2.2.2.3   Blanket gas

To account for the heat transferred to the blanket gas by convection from hot burner surfaces and from blanket gas to insulation and part surfaces, we discretize the fluid in the furnace into a set of control volumes. A control volume is assumed to be well mixed, i.e., there is no spatial variation in temperature within a control volume. Note that these control volumes are different from the temperature control zones for feedback control. For each control volume, heat is transferred from the top and bottom furnace surfaces within the control volume. Additionally, if there is a part present in the control volume, then heat is transferred to/from the top and bottom part surfaces to the fluid well. As the flow is in one direction, heat gained in one control volume w is transferred to the next control volume $w + 1$ in the direction of flow. The heat exchange in control volume w is calculated via the enthalpy as a function of temperature of the fluid. Therefore, the heat exchange rate in control volume $w + 1$ is the sum of heat transferred from the furnace and part surfaces and from the previous control volume w:

The blanket gas inside the furnace is assumed to be well-mixed within each control volume (equivalently, the gas temperature inside the control volume is uniform), and the gas flow is assumed to be in one direction. We assume a uniform velocity profile in the cross section of the furnace. The

23

change in temperature of the flowing fluid is found by accounting for the heat transferred by convection from the top and bottom furnace surfaces and the design surfaces of a control volume to the fluid. As flow is in one direction, the heat gained one control volume w is transferred to the next control volume $w + 1$. The heat exchange in control volume w is calculated via the enthalpy as a function of temperature of the fluid. The heat exchange in the next control volume $w + 1$ is given by the addition of the heat from control volume w with the heat of convection from the ceiling and floor in control volume w. Then, the temperature of control volume $w+1$ can be found from the resulting enthalpy. Specifically:

$$Q_{w+1} = \sum_{i \in furnace\ surfaces} h_{furn} A_i \left(T_i - T_w^\infty\right)$$

$$+ \sum_{i \in part\ surfaces} h_{part} A_i \left(T_i - T_w^\infty\right) + Q_w = \frac{H(T_w^\infty)}{\dot{m}_{N_2}} \tag{2.24}$$

Now, the temperature of the control volume $w + 1$ can be found from the resulting enthalpy:

$$T_{w+1}^\infty = G\left(\frac{Q_{w+1}}{\dot{m}_{N_2}}\right) \tag{2.25}$$

Here, the assumption is that nitrogen is the only gas flowing in the furnace. Also, the system is leak free. Enthalpy to temperature and temperature to enthalpy calculations are performed from a look up table. Under the usual range of temperatures in the furnace, nitrogen does not undergo any phase

24

transformation. Therefore, the enthalpy is a monotonically increasing function of temperature.

2.2.3 View factor calculation

We calculate the view factor matrix $F_{i,j}$ between surfaces using Hottel's crossed string method [26]. We first discretize each surface into a set of k sub-surfaces. The view factor between each sub-surface and full surface is given by:

$$F_{i,j} = \frac{AD + BC - AC - BD}{2A_i} \tag{2.26}$$

where AC and BD are the edge to edge distances and AD and BC are the distances between end points of surfaces A_i and A_j where the lines cross (see Figure 2.4). In the limit as the area of surface i approaches zero, the view factor expression becomes:
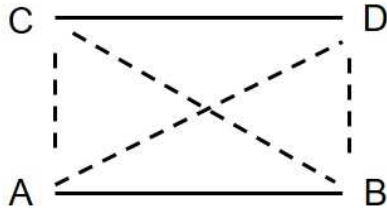
Figure 2.4: Schematic of surfaces for view factor calculation. The solid lines AB and CD represent the surfaces. The dotted lines AC and BC represent the edge to edge distances and AC and BD represent the distances between the end points of the surfaces where the lines cross.

$$F_{i,j} = \frac{sin\psi_2 - sin\psi_1}{2} \qquad (2.27)$$

where ψ_l are the angles between surface i and the edges of surface j. This principle is applied to each sub-surface and the total view factor is the sum of the sub-surface view factors weighted by their corresponding surface areas:

$$F_{i,j} = \sum_k \frac{F_{ik,j}}{A_{ik}} \qquad (2.28)$$

To calculate the angles, ψ_l, ν rays from each sub-surface are traced and the surface each ray intersects first is determined. The angles ψ_1 and ψ_2 can be estimated from two adjacent rays that encounter two different surfaces where:

$$\psi = \frac{\psi_l + \psi_{l+1}}{2} \qquad (2.29)$$

A simple example for three surfaces is shown in Figure 2.5. The angles ψ_a, ψ_b, and ψ_c are calculated from rays originating from the kth sub-surface of surface A_1 (A_{1k}). The view factors from sub-surface A_{1k} to surfaces A_2 and A_3 are:

$$F_{1k2} = \frac{\sin \psi_c - \sin \psi_b}{2}, \quad F_{1k3} = \frac{\sin \psi_b - \sin \psi_a}{2} \qquad (2.30)$$

Now, the total view factors between surfaces $A_1 - A_2$ and $A_1 - A_3$ can be calculated by adding the view factors of the sub-surfaces in A_1 using Equation (2.28).

26
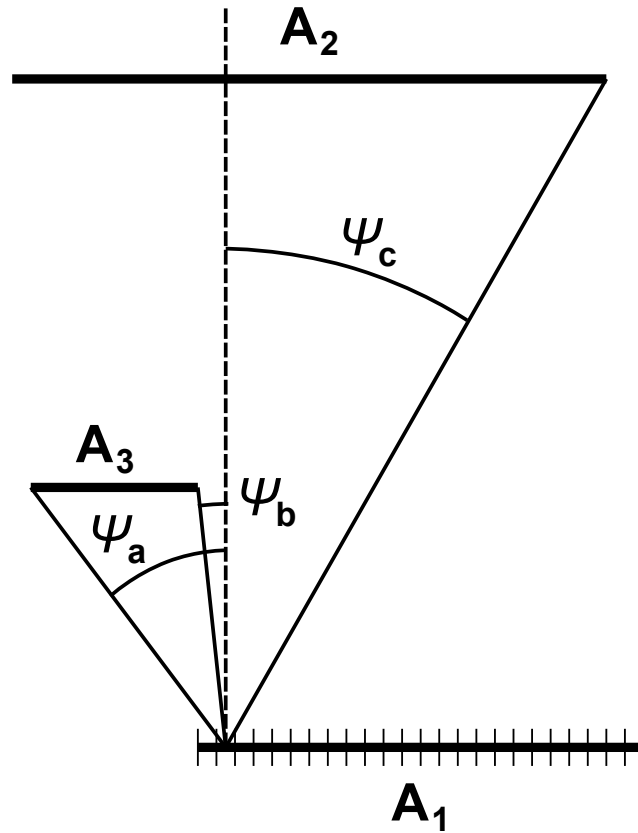
Figure 2.5: Angles between a sub-surface of A_1 and the visible areas of surfaces A_2 and A_3. (Image source: Heng *et al.* [48])

The percentage error of this approach with sufficiently small surface and ray angle discretization compared to the analytical solution is less than 1%. Moreover, the algorithm can be easily parallelized, which reduces computation time significantly for larger number of surfaces or discretizations.

The furnace is partitioned into four *temperature control zones* to indirectly control the part temperatures by controlling the zone temperatures. Note that these control zones and the control volumes of the blanket gas are

different. The middle insulating surfaces on the ceiling of each zone (see Figure 2.3) are assumed to host the temperature sensors for feedback control. Each control zone has eight adjacent burners on the furnace ceiling and four adjacent burners on the floor. A simple linear control strategy is adopted, wherein a proportional-integral (PI) controller adjusts the mass flow rate of fuel of the twelve burners of each zone simultaneously to control the temperature of that particular zone. However, zone-to-zone long range radiation interactions will affect the temperatures of other zones as well. The temperature set points of the PI controllers directly affect the temperature distribution of the parts in the furnace and thus the energy consumption of the system.

The inputs to the model are the geometric details of the furnace and the parts, the inlet temperatures of the parts and the blanket gas, and the physical properties of the steel parts (see Table 3.1). The model evaluates the energy input to the furnace system and the temperature distribution of the part within the furnace at each time step.

2.2.4 Solution algorithm

In this section, we describe the iterative solution procedure to solve the heat transfer and heat balance equations of the furnace presented in the previous subsection (section 2.2.2). The movement of the parts in the furnace is approximated as a series of discrete events. Part velocity is determined by the speed of the conveyor belt. The time step (and hence the distance a part travels in one time step) to simulate the furnace is fixed at a value that

captures meaningful changes in the temperature field at minimal computation costs. The geometry dependent view factor matrix is computationally expensive to calculate. In order to improve speed, view factors between different surface pairs were pre-calculated and tabulated. In this work, the geometry of the parts are fixed. Therefore, the pre-tabulated view factor matrix can be used to simulate the furnace at different operating conditions. Once the view factors are computed, the energy balance equations are solved by the following procedure (also explained in a flowchart in Figure 2.6) to calculate the temperature and heat profiles of the furnace as a function of time:

1. Initialize system with temperatures and heat duties of all the furnace surfaces, including part surfaces.

2. Identify the parts that are currently under processing inside the furnace by accounting for part that have been removed and parts that have been newly introduced

3. Solve burner model to calculate temperatures and heat duties of all the burner surfaces for a given mass flow rate of fuel, determined by the feedback controller

4. Solve for radiosities from given surface temperatures

5. Using radiosites of part and insulation surfaces, calculate the updated temperatures and heat duties of part and insulation surfaces

6. Repeat steps (3)-(5) until the system converges to a desired tolerance

29

7. Using the heat duties of the part surfaces, calculate the inhomogeneous temperature distribution of all the active parts using Crank-Nicolson finite difference scheme

8. Using the heat duties of the insulation surfaces, calculate the heat lost to the ambient via insulation walls

9. Control the zone temperatures (see Figure 2.3) to the desired set-points by manipulating the fuel flow rates to the burners (feedback control)

10. Advance tray to the next location, increment time by one time step, and repeat steps (2)-(9) until a batch of parts are processed sequentially in the furnace

To obtain a defect-free and structurally sound product, one should not only control the macroscropic properties like temperature but also control the microscopic properties like austenite grain size. The microstructural changes occurs at a much smaller length scale (micro-scale) compared to the macro-scale temperature evolution. Therefore, we adopt a two-scale modeling approach for calculating the grain size distribution of the parts in addition to the temperature distribution during austenitization process and their consequences on the metallurgical properties of the quenched product.

2.3 Microscopic model: prediction of austenite grain sizes

Steel is composed of many crystallites or *grains* of varying size and orientation, and is thus a *polycrystalline* material. The orientation of the grains can be random or directed. The crystallinity of a solid has important effects on its physical properties. The *grain boundary* is a single-phase interface with identical crystals on each side of the boundary, except in orientation. The grain boundary contains the atoms that have been displaced from their original lattice sites and the impurities present in the crystal. A grain boundary is a crystal structure defect and so is a region of high energy. The higher the free energy of a system, the lower is its thermodynamic stability. As a result, there is a thermodynamic driving force to decrease the free energy by reducing the total area of the grain boundary. *Grain growth* is the process by which the average grain size increases. Grain growth takes place by diffusion and not coalescence like in water droplets (that merge together to form a larger bubble) [53]. Since diffusivity is a function of temperature and the length scale of diffusion is proportional to the square root of diffusivity, grain growth occurs when the temperature is high enough and the amount of time the material is subjected to high temperature (specifically, heat treatment) is long enough. During grain growth, the number of gains per unit volume decreases, the average grain size per unit volume increases and the energy per unit volume decreases resulting in a state of higher thermodynamic stability [53].

The austenite grain size at the exit of the furnace determines the tough-

ness of the quenched product. Larger grain sizes make the product brittle. We use the time-dependent empirical model reported in Anelli [7] for predicting the average size of austenite grains (d_γ in μm) which results from a specific thermal history. The austenite grain size is calculated from the following equations:

$$d_{\gamma,i+1} = k_1 \left(t^* + \Delta t\right)^{k_2} \exp\left(-Q_o/RT_{i+1}\right) \tag{2.31}$$

$$t^* = \left(d_{\gamma,i}/\left(k_1 \exp\left(-Q_o/RT_{i+1}\right)\right)\right)^{1/k_2} \tag{2.32}$$

where $d_{\gamma,i+1}$ and T_{i+1} are the current grain size and current temperature respectively, Δt is the time interval, R is the gas constant, and t^* is the fictitious time in hours required to reach the previous grain size, $d_{\gamma,i}$, at the current temperature. k_1, k_2, and Q_o are the empirical constants. The values of the constants are taken for FF82 steel having composition 0.85% C, 0.62% Mn, 0.25% Si, 0.03% Cr, and 0.03% Al [7].

To embed the above relations in the furnace model described in Section 2.2, we discretize the part into a set of *regions* (see Figure 2.7). The temperature T_{i+1} for a region is the average of all the node temperatures of the Crank-Nicolson finite difference scheme used to determine part temperature distribution (cf. Section 2.2) within the region at the current time step. The time difference Δt for austenite grain size prediction is the same as that for evaluating the part temperature distribution in the furnace simulation. The size of a region is selected such that the temperature differences within it

is minimal and the grain size calculated at the maximum permissible furnace operation temperature is less than the dimensions of the region. Based on the above two criteria, we divide the part having dimensions 1.25 m $\times$ 0.5 m into 6×3 regions. The transformation of steel to austenite is rapid and occurs over a time span in the order of a few seconds, much smaller than the simulation time step size of four minutes. Therefore, during furnace simulation, from the time instant at which the temperature of a region exceeds the austenite transformation temperature, $T_{austenite}$, the average grain size, $d_{\gamma,i+1}$, for that region is predicted using eqs. (2.31) and (2.32).
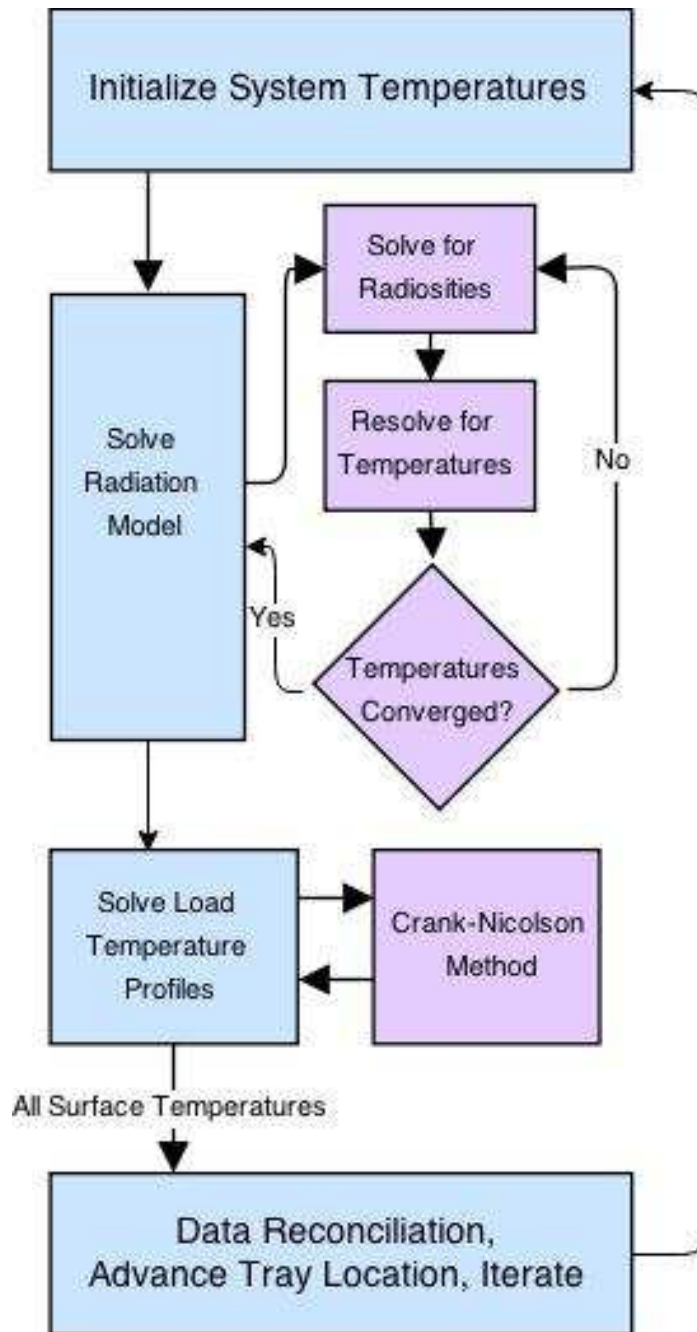
Figure 2.6: Solution algorithm to calculate temperatures and heat duties of all the surfaces in the furnace and using the heat duties of part surfaces to calculate the inhomogeneous part temperature distributions. (Image source: Heng *et al.* [48])

34
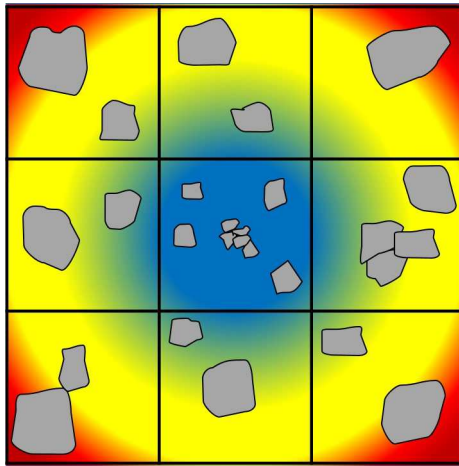
Figure 2.7: An illustrative part temperature and grain size distribution diagram. The precipitated austenite grains are represented by the shapes filled in gray. The regions close to the part surface, which are heated via radiation, have higher temperatures and thus larger grains. On the other hand, the interior regions, which are heated only via conduction, have lower temperatures thus smaller grains.

Chapter 3

Surrogate model-based optimization

This chapter is based on material published in papers "V. R. Heng, H. S. Ganesh, A. R. Dulaney, A. Kurzawski, M. Baldea, O. A. Ezekoye, and T. F. Edgar. Energy-oriented modeling and optimization of a heat treating furnace. Journal of Dynamic Systems, Measurement, and Control, 139(6):061014, 2017" [48], "H. S. Ganesh, E. M. Taleff, T. F. Edgar, and M. Baldea. Simultaneous optimization of material properties and energy efficiency of a steel quench hardening process. In American Control Conference (ACC), 2017, pages 22192224. IEEE, 2017. doi: 10.23919/ACC.2017.7963282" [38] and "H. S. Ganesh, T. F. Edgar, and M. Baldea. Modeling, optimization and control of an austenitization furnace for achieving target product toughness and minimizing energy use. Journal of Process Control, 2017. doi: 10.1016/j.jprocont.2017.09.008" [36]. In Heng *et al.* [48], I developed the dynamic burner model, improved the part model, ran the furnace simulations and analyzed the results. I am the primary contributor of papers Ganesh *et al.* [38] and Ganesh *et al.* [36].

3.1 Optimization problem formulation

In this section, we combine the physics-based furnace model and the empirical austenite grain growth prediction model described in Chapter 2, to formulate and solve an optimization problem that identifies the zone temperature set points such that the energy consumption of the system is minimized without compromising product quality. The parts must be heated beyond the phase transformation temperature, $T_{austenite}$, with minimum variation in temperature distribution in order to make sure that the transformation is effected throughout the part. Additionally, overheating of parts makes the quenched product very brittle (less tough). Austenite grain size determines how tough the quenched product is. Therefore, in order to ensure toughness of the product, the austenite grain size must be within an upper limit. The objective and constraints described above can be described as the following optimization problem:

$$\underset{\boldsymbol{T}_{sp}}{\text{minimize}} \quad Energy\ Input\ Per\ Part = f(\boldsymbol{T}_{sp})$$

subject to

$$T_{sp,lb} \leq T_{sp,l} \leq T_{sp,ub},\ l \in [1,4]$$

$$T_{sp,l} + T_{sp,diff} \leq T_{sp,l+1},\ l \in [1,3] \tag{3.1}$$

$$T_{part,min,lb} \leq T_{part,min}$$

$$\frac{\sigma_{part,T}}{\mu_{part,T}} \leq COV_{part,ub}$$

$$d_{\gamma,max} \leq d_{\gamma,ub}$$

where $T_{sp,l},\ l \in [1,4]$ are the zone temperature set points of each individual

zone l, $T_{sp,lb}$ and $T_{sp,ub}$ are the lower and upper bounds of the zone temperature set points respectively, $T_{sp,diff}$ is the minimum allowed enforced temperature difference between consecutive zones. $f(\boldsymbol{T}_{sp})$ is the energy input to the system per part processed. The part variables described below represent the conditions at the exit of the furnace. $T_{part,min}$ and $T_{part,min,lb}$ are the minimum part temperature and its lower bound respectively, $\sigma_{part,T}$ is the standard deviation in temperature, $\mu_{part,T}$ is the average temperature, $COV_{part,ub}$ is the upper bound of the coefficient of variation $(\frac{\sigma_{part,T}}{\mu_{part,T}})$, $d_{\gamma,max}$ is the maximum of average grain size among all portions in a part and $d_{\gamma,ub}$ is the upper bound of the grain size.

The control objective for this system is to achieve a minimum part temperature and quality in face of periodic disturbances caused due to periodic input of parts into the furnace and periodic removal of parts from the furnace. As a consequence, we represent the operation of the furnace in the constant input/constant output regime as a "steady-state"/continuous process with the respective average values of the state variables [54, 119, 132]. Therefore, the part variables at the exit of the furnace in problem (3.1) is calculated for the inhomogeneous distribution of each part and then averaged over all the parts processed under the steady-state operating regime of the furnace.

The quantity that we aim to minimize is the energy input per part. The zone temperature set points are bounded from above and below to obtain realistic solutions around the region of austenite phase. A temperature difference between consecutive zones is enforced in the problem formulation so

38

that the average part temperature increases monotonically with time within the furnace and there is no heat loss from the parts to the furnace walls. The ratio of the part standard deviation and its mean value is a measure of the temperature spread and must be within a threshold to ensure uniformity in heating. Finally, the maximum of the average grain sizes of all the portions of a part must be less than an upper bound to ensure toughness of the quenched product.

3.2   Surrogate model building

The radiation-based furnace model described above is procedural, i.e., it contains an algorithm – the dual-iterative solution algorithm explained in Heng *et al.* [48], for the calculation of part and insulation surface temperatures and heat duties– rather than explicit expressions for computing the model variables, which precludes the calculation of the gradient entities required by optimization solvers [15]. On the other hand, a derivative-free optimization approach would significantly increase the computational costs. Consequently, we make use of *surrogate models* to approximate the input-output behavior of the system for the purpose of solving problem (3.1). The surrogate model functional form is based on the physical characteristics of the system, aiming particularly to capture the radiation heat transfer and the zone-to-zone interactions. The general functional form of the surrogate model is:

$$
z = \beta_1 T_{sp,1} + \beta_2 T_{sp,2} + \beta_3 T_{sp,3} + \beta_4 T_{sp,4} + \beta_5 T_{sp,1}^4 + \beta_6 T_{sp,2}^4 + \beta_7 T_{sp,3}^4 + \beta_8 T_{sp,4}^4
$$
$$
+ \beta_9 T_{sp,1}^3 + \beta_{10} T_{sp,2}^3 + \beta_{11} T_{sp,3}^3 + \beta_{12} T_{sp,4}^3 + \beta_{13} T_{sp,1} T_{sp,4} + \beta_{14} T_{sp,2} T_{sp,4}
$$
$$
+ \beta_{15} T_{sp,3} T_{sp,4} + \beta_{16} T_{sp,1} T_{sp,3} + \beta_{17} T_{sp,2} T_{sp,3} + \beta_{18} T_{sp,1} T_{sp,2}
$$

$$(3.2)$$

where z is the output variable, $T_{sp,l}$, $l \in [1,4]$ are the temperature set points of each individual zone l, and β_m, $m \in [1,18]$ are the coefficients for the surrogate model found by linear regression. The input variables are the four zone temperature set points $T_{sp,l}$, $l \in [1,4]$. The output variables are the minimum temperature of part at exit $T_{part,min}$, coefficient of variation of part at exit $\frac{\sigma_{part,T}}{\mu_{part,T}}$, the maximum grain size of part at exit $d_{\gamma,max}$, and the energy input to the system per part processed $f(\boldsymbol{T}_{sp})$. For all the output variables, the surrogate model form remains the same, however with different model coefficients. Other variables such as part input temperatures, material properties of input part, the conveyor belt speed, etc., may influence the temperature profile of the part at the furnace exit. However, in the industrial system under consideration, (i) the parts are always at ambient temperature prior to being processed, with the influence of this temperature on the output being relatively small, (ii) the conveyor belt speed cannot by varied by the control system and hence does not change during the production run. As a consequence, we chose to not explicitly capture the impact of these variables on the surrogate models.
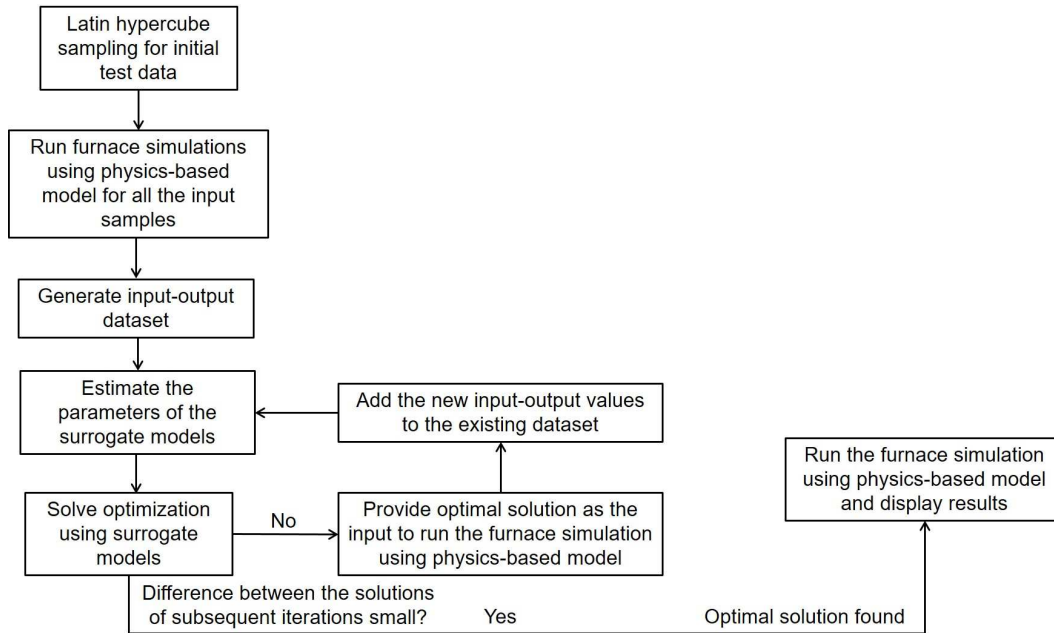
Figure 3.1: The iterative procedure for simultaneous estimation of surrogate model coefficients and solution of optimization problem. (Image source: Korambath *et al.* [67])

3.3 Optimization solution using surrogate-models

The flow chart for estimation of surrogate model coefficients and solution of the optimization problem (eq. (3.1)) to identify the optimal zone temperature set points is presented in Figure 3.1. We use Latin Hypercube Sampling to build an input space. 100 data points were sampled across the plausible range for the four zone temperature set points. The furnace is simulated for a batch of 40 parts for each of the input samples and the output variables are calculated. Next, the surrogate model coefficients are determined by linear regression using the input-output data. The optimization problem

uses the surrogate model. The optimal solution is provided as the input to the detailed model to perform the furnace simulation. The optimal solution and the outputs of the simulation are added to the existing input-output data set and the surrogate model coefficients are re-identified. Note that both the values of the model coefficients and the objective function change with each iteration as the least squares regression is performed using a revised data set. This approach increases the fidelity of the surrogate models in the region where optimal solution is likely to be found. The aforementioned iterative procedure for simultaneous model identification and optimization is repeated until the difference between the solutions of two consecutive iterations is within a predefined tolerance. The values of the constraints used in the optimization problem are listed in Table 3.1.

3.4 Furnace simulation case 1: Target grain size of 90 μm

Table 3.1 lists the values of the inequality constraints in eq. (3.1). The geometric details of the furnace and the furnace parameters can be obtained from our previous publications [32, 48]. The interior-point optimization solver *IPOPT* [134] in Matlab is used to solve the nonlinear optimization problem. The optimal solution for the zone temperature set points is [1012 K, 1042 K, 1184 K, 1214 K] for zones 1 to 4 respectively. It takes 25 simulations to converge to the solution and each simulation takes less than 10 minutes of CPU time (using a computer running Windows 10 with a 2.4 GHz Intel Core

42

Furnace details	
Length of the furnace	16 m
Height of the furnace/length of the side walls	2 m
Length of each discretized furnace surface except the side walls	0.25 m
Total number of furnace surfaces	130
Length of a part	1.25 m
Ordinate of a part	0.75 m
Height of a part	0.5 m
Process conditions	
Number of parts processed	40
Part residence time	4 hrs
Simulation time step	4 min
Inlet temperature of parts	300 K
Inlet temperature of blanket gas	400 K
Number of points in x-direction for Crank-Nicolson method	6
Number of points in y-direction for Crank-Nicolson method	6
Total time of furnace operation	25 hrs
Grain growth prediction	
k_1	4.1×10^7
k_2	0.12
Q_o	141 KJ/mol
$T_{austenite}$	1065 K
Number of portions in the x-direction for grain size prediction	3
Number of portions in the y-direction for grain size prediction	6
Set point optimization	
$T_{sp,lb}$	1000 K
$T_{sp,ub}$	1300 K
$T_{sp,diff}$	30 K
$T_{part,min,lb}$	1100 K
$COV_{part,ub}$	0.05
$d_{\gamma,ub}$ (Case 1)	90 μm
$d_{\gamma,ub}$ (Case 2)	50 μm

Table 3.1: List of parameters for furnace simulation and set point optimization.

i5 Processor and 6 GB RAM).

The zone temperatures and the fuel flow rates are plotted in Figure 3.2

for processing a batch of 40 parts. The closed-loop control system maintains the zone temperatures close to the set points indicated by the dashed lines in the top row plots of Figure 3.2. Cold parts periodically enter zone 1 and create a heat sink. Hence, zone 1 temperature oscillates around its set point. The temperature disturbances are propagated to the other zones because of the long range zone-to-zone radiation interactions. Additional oscillations are caused due to parts exiting zone 4. The bounds of fuel flow rates are indicated by the dashed lines in the bottom row plots of Figure 3.2.
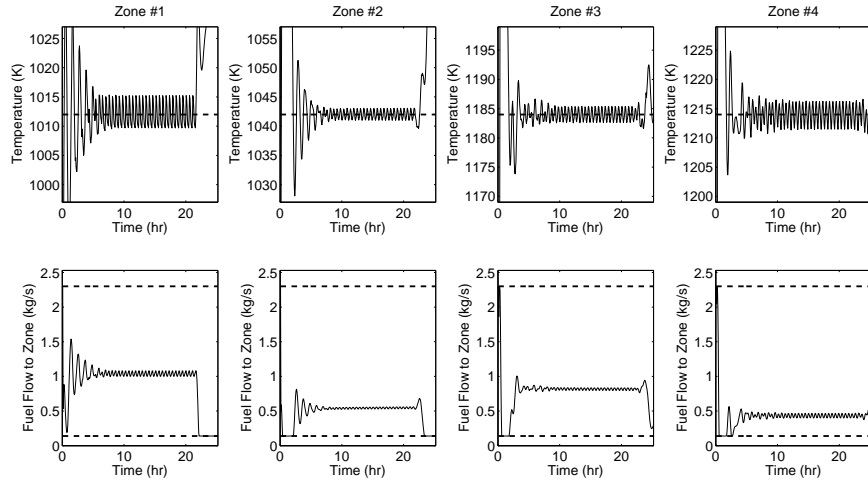
Figure 3.2: The zone temperature and mass flow rate of fuel to the burners as a function of the time of furnace operation for a batch of 40 parts.

Figure 3.3 shows the exit conditions of all the 40 parts processed sequentially. The system stabilizes to the steady state value, where the minimum part temperature is 1088 K, the average part temperature is 1155 K, the standard deviation of temperature is 50.5 K, and the total enthalpy change is 1114

MJ. It is observed that the minimum temperature is 12 K lower than the lower limit of 1100 K, set as a constraint in the optimization formulation, due to inaccuracies in the surrogate model. The coefficient of variation (standard deviation over mean) in temperature of the part at exit is 0.044 which is within the desired value of 0.05. Therefore, the temperature differences within the part are minimal.
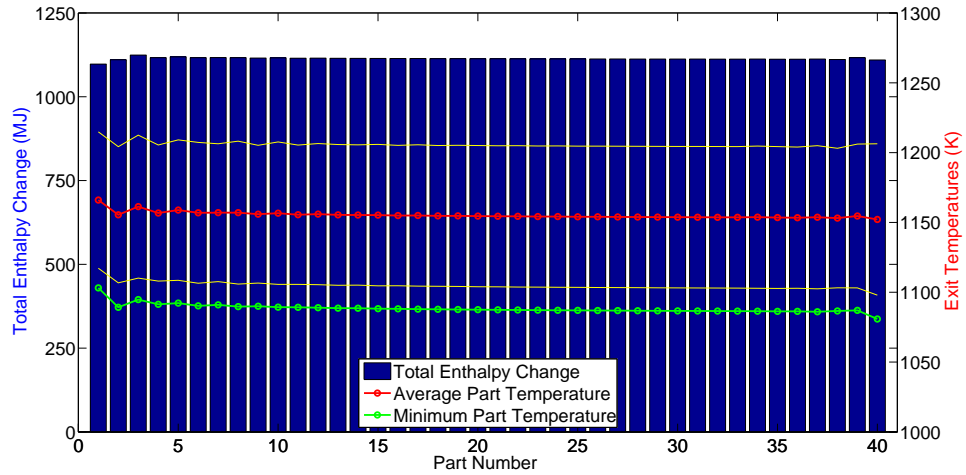
Figure 3.3: The exit conditions of all the 40 parts processed sequentially in the heat treating furnace.

Figure 3.4 shows the grain size distribution of the 20th (middle of the batch) part as a function of its processing time. As the radiation from the burner panel primarily influences the surfaces of the part, the outer portions of the part will have higher temperatures. On the other hand, the core is heated only through conduction. Hence, the interiors of the part will have lower temperatures that increase gradually. Grain size is proportional to the

45

temperature and time of heating (see eqs. (2.31) and (2.32)). Therefore, the regions that are close to the part surface will have larger grain sizes and those in the core will have smaller grains. The grain size begins to increase from zero in a region only when the region is heated past the austenite transformation temperature $T_{austenite}$. At exit the maximum grain size is 73.80 μm, which is within the threshold of 90 μm. The minimum grain size of the part at exit is greater than zero, which means that all the regions of the part have been completely transformed to austenite.
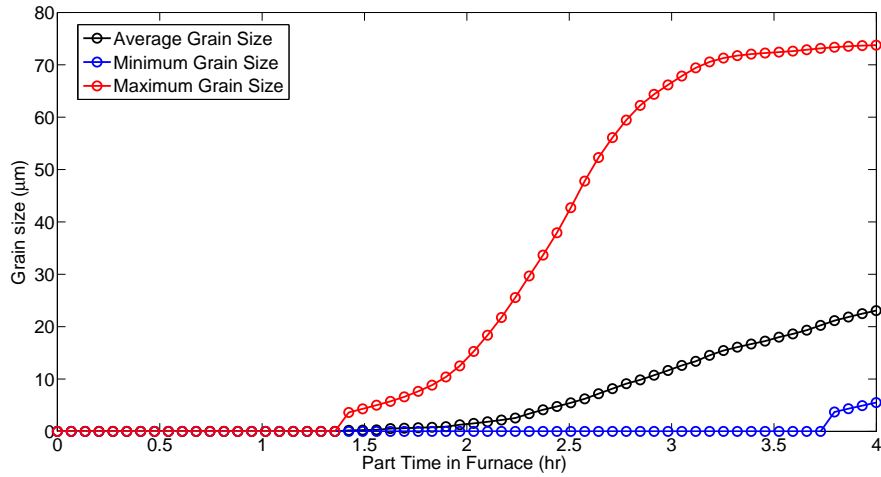
Figure 3.4: The grain size distribution of the 20th part as as function of its processing time.

3.4.1 Energy efficiency comparison

Table 3.2 compares the energy consumption and exit conditions of the parts operated under optimized zone temperature set points with that of the heuristic case reported in Heng *et al.* [48]. The energy input per part, our important energy metric, is 3.63 GJ in the optimized case as compared to 3.76

Heat Sources and Sinks	Heuristic Set Points	Optimized Set Points
Total Energy Input Per Part (GJ)	3.76 GJ	3.63 GJ
Part Minimum Temperature (K)	1126 K	1088 K
Coefficient of variation	0.043	0.044
Maximum grain size (μm)	93.60 μm	73.80 μm
Energy to Parts (%)	54.2%	53.5%
Energy Out the Exhaust (%)	42.7%	43.4%
Energy to Flowing Nitrogen (%)	0.5%	0.5%
Energy Through Insulation (%)	2.6%	2.6%

Table 3.2: Comparison of the exit conditions and energy consumption of the optimal furnace operation with the heuristic operation reported in Heng *et al.* [48].

GJ in the heuristic case. Hence, the optimal operation mode has 3.5% increase in the energy efficiency compared to the heuristic operation mode. The energy gain is mainly achieved by operating at the minimum part temperature at exit constraint. Additional gains are due to the nonlinear contributions to the energy efficiency from a different zone-to-zone radiation interactions due to varied zone temperature set points. The coefficient of variation in temperature of the parts at furnace exit are similar in both cases indicating that the parts are uniformly heated in the optimized operating mode. The maximum grain size in the optimal operation mode is 73.80 μm compared to 93.60 μm in the heuristic operation mode. Hence, the quenched product in the optimized case is tougher or less brittle than the heuristic operation case. The percentage of energy input to parts, exhaust, blanket gas, and insulation are similar between the two operation modes. The set points of the existing feedback controllers in the actual plant should therefore be changed to the optimized values to lower the energy consumption of the system and improve the quenched product toughness.

3.5 Furnace simulation case 2: Target grain size of 50 μm

We solve two optimization problems: the original formulation (i.e., equation 3.1) and a "conventional" formulation as discussed in Heng et al. which is similar to the former but does not impose any grain size restrictions. In each case, the nonlinear optimization problem is solved using the interior-point optimization solver *IPOpt* in Matlab [134].

For the original formulation (problem (3.1)), the optimal zone temper-

ature set points are [1091 K, 1121 K, 1151 K, 1181 K]. For processing a batch of 40 parts under optimal zone temperature set points, the zone temperatures and mass flow rate of fuel as a function of time are plotted in Figure 3.5. The feedback controller maintains the zone temperatures with minimum variations from the set points, as shown by the top row plots in Figure 3.5. The periodic oscillations seen in the zone temperatures are attributed to the periodic entry and exit of the parts during furnace operation. The absolute temperatures are greater than 1000 K, while the variation in temperature is less than about 5 K at the steady-state (constant input/output rate of parts) operating regime. The practical impact of these oscillations is negligible. However, the first part takes about 4 hours to exit the furnace. Until the first part exits the furnace, the operation is *pre-steady state* where there are fewer heat sinks (parts) in the furnace compared to the number present at steady-state furnace operation. Similarly, the processing of the 32nd to 40th part is post-steady state operation with fewer heat sinks in the furnace. During the pre- and post-steady state operating regimes of the furnace, due to absence of heat sinks and lower bound for fuel flow rate in the burners, the zone temperature set points cannot be tracked well. These start/end effects are not important in production runs, when hundreds of parts may be processed.

The corresponding mass flow rates of the fuel to the burners are shown in the bottom row plots in Figure 3.5. We can see that the mass flow rate of the fuel is highest in zone 1, which is due to the heat sink created by the entry of cold parts in zone 1. Long range zone-to-zone radiation interactions affect the zone temperatures and thus in the mass flow rates of fuel to the burners of other zones as well.

The exit conditions of all the 40 parts processed in the furnace sequentially are shown in Figure 3.6. The exit conditions of the parts operating at steady state furnace operating regimes are averaged and analyzed. The average energy input to parts, estimated as the total enthalpy change, is 1090 MJ per part. The average of minimum temperatures of parts at exit is 1087 K, which is slightly less than the 1100 K lower bound constraint of the optimization problem formulation (eq. (3.1)). This discrepancy in the minimum temperature values can be attributed to the inaccuracies in the surrogate model. Finally, the average coefficient of variation is 0.036, which is within the upper bound of 0.05.

The heat input and temperature variation of part number 20 (middle
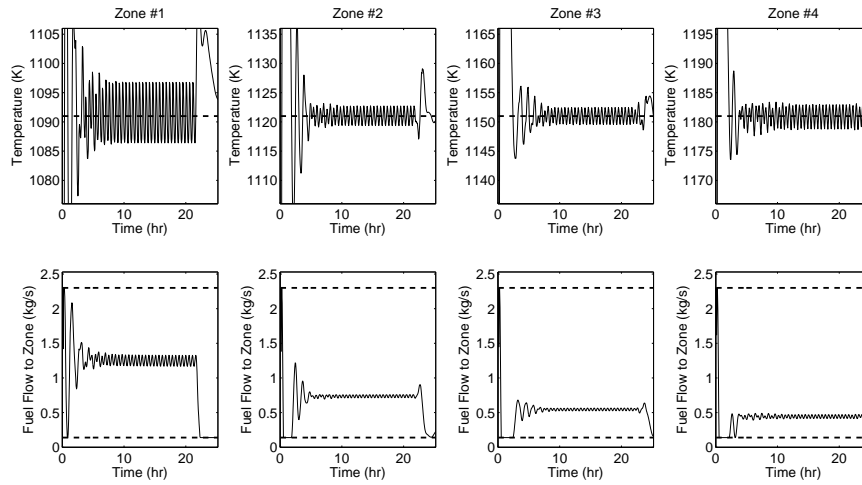
Figure 3.5: The solid lines in the plots of top row represent zone temperatures and in bottom row represent fuel flow rates to the burners as a function of time for zones 1 to 4. The dashed lines in the plots of top row indicate the zone temperature set points and the dashed lines in the plots of bottom row indicate the bounds of fuel flow rates to the burners.

of the batch part), processed under steady-state furnace operation regime, as a function of time of processing is shown in Figure 3.7. It is to be noted that the part residence time is four hours and there are four control zones in the furnace. Therefore the time of processing also corresponds to the position (zone number) within the furnace. As expected, the heat input to the part decreases with time as a result of reduced forcing function or temperature difference between the part and the burner surfaces. The oscillation in the heat input is due to the disturbance created by the periodic entry and exit of parts in the furnace. We see seven peaks in the heat to part curve indicating entry of seven parts into the furnace during the residence time of a single part. The maximum temperature occurs at the surface of the part and hence shows a rapid rise to its saturation value. On the other hand, the minimum temperature (and thus average temperature) is at the interior of the part, which is heated only via conduction. Therefore, the rise in minimum temperature with time of processing is gradual.
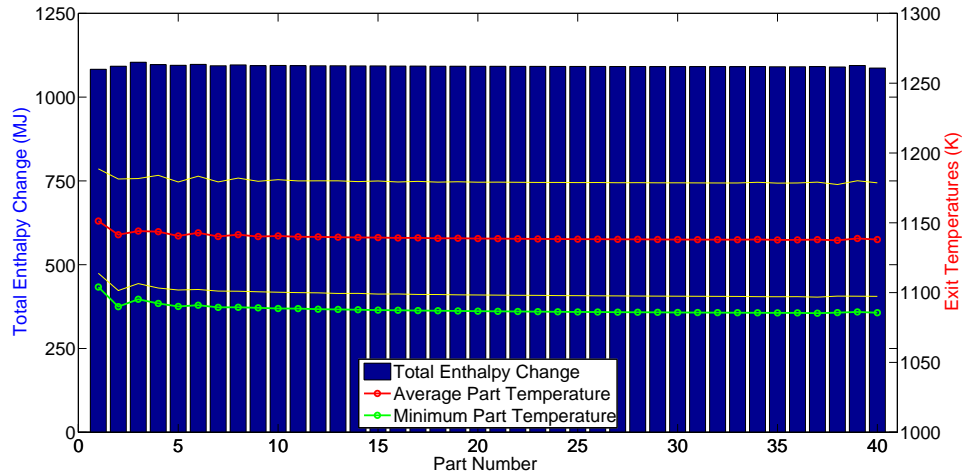
Figure 3.6: Part exit conditions for a batch of 40 parts processed under optimized zone temperature set points. The red line is the part average exit temperature and the green line is the part minimum temperature at exit. The yellow lines indicate the standard deviation of the part exit temperatures from its mean.

Finally, we examine the evolution of the grain sizes for the 20th part as a function of time under optimal temperature set points in Figure 3.8. The austenite grain size of a region in the part increases from zero only when the temperature of the region is greater than the austenite transformation temperature $T_{austenite}$. The maximum grain size occurs in regions where is temperatures are higher, i.e, the outer surfaces of the part. The minimum grain size occurs at the core of the part. The maximum grain size is 41.75 μm and the minimum grain size is greater than zero at the exit of the furnace indicating that all the portions of the part have completely transformed to austenite.

Switching now to the "conventional" formulation of Heng *et al.* [48], we examine the grain size distribution under the optimized zone temperature set points, whereby the optimization problem only accounts for part temperature control. In this case, the optimized setpoints are [1000 K, 1030 K, 1191 K, 1221 K] (Figure 3.9). The reader is referred to Heng *et al.* [48] for more extensive
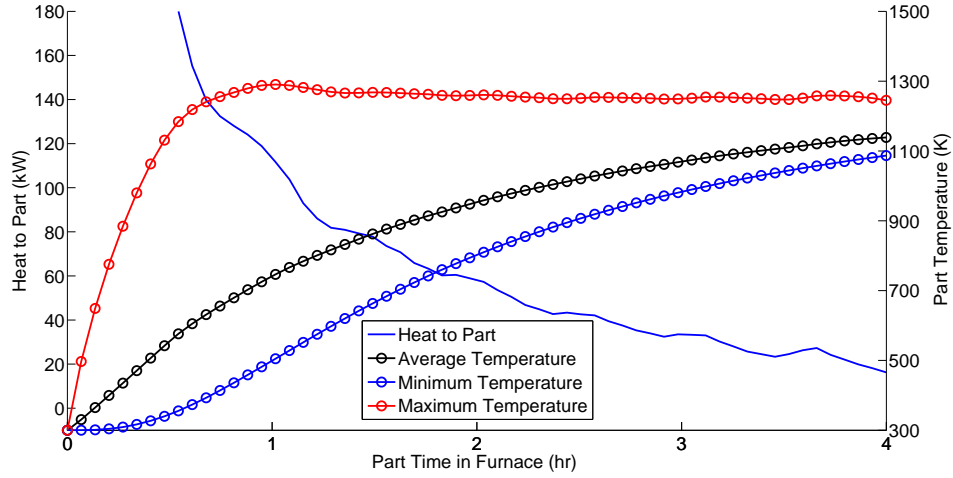
Figure 3.7: Heat input to the 20th part and its temperature distribution details as a function of its time (and thus position) of processing.

simulation details. In this case, the maximum grain size at the exit of the furnace is 83.67 μm, higher than the desired value of 50 μm by 33.67 μm, resulting in a product that is very brittle.

3.5.1 Energy efficiency comparison

Heat Sources and Sinks	Conventional Formulation	Original Formulation
Total Energy Input Per Part (GJ)	3.58 GJ	4.03 GJ
Part Minimum Temperature (K)	1088 K	1087 K
Coefficient of variation	0.045	0.036
Maximum grain size (μm)	83.67 μm	41.75 μm
Energy to Parts (%)	54.4%	46.5%
Energy Out the Exhaust (%)	42.5%	50.7%
Energy to Flowing Nitrogen (%)	0.5%	0.5%
Energy Through Insulation (%)	2.6%	2.3%

Table 3.3: Total energy input to the furnace and part exit conditions under the temperature set points determined by solving the original optimization formulation and the conventional formulation.

The results presented in the previous section afford some interesting insights in the impact of material quality constraints (notably, grain size) on the operation of the furnace. To this end, we compare the energy consumption

51
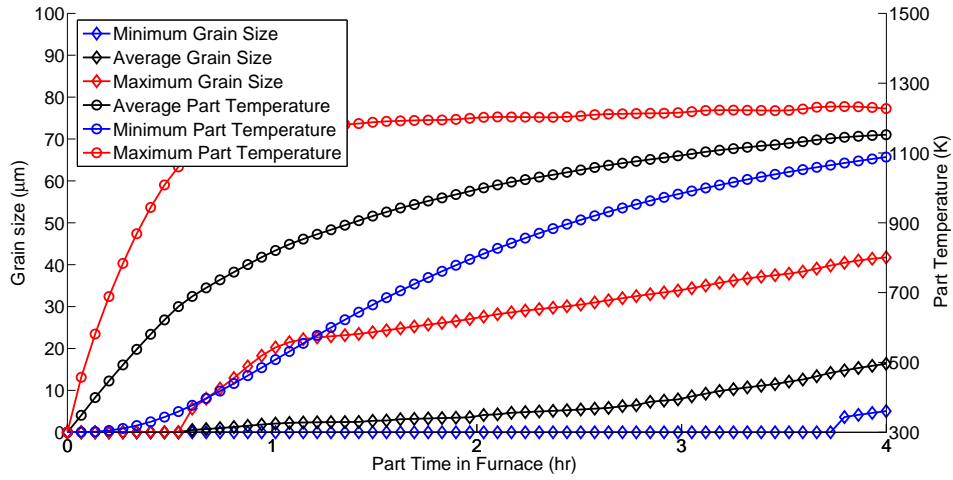
Figure 3.8: The average, minimum, and maximum grain sizes of part number 20 as a function of the time of processing under optimal temperature set points.
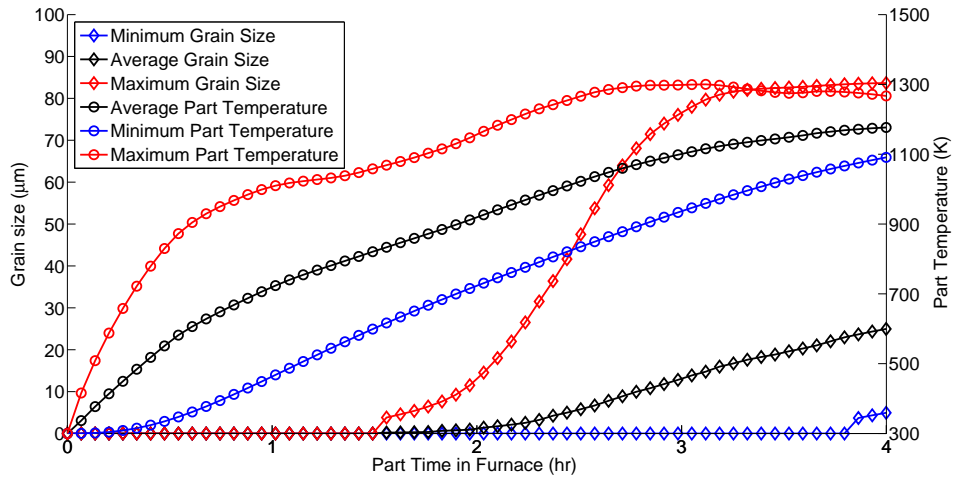
Figure 3.9: The average, minimum, and maximum grain sizes of part number 20 as a function of the time of processing under optimized temperature set points of Heng *et al.* [48] that do not account for grain size restriction.

of the system and exit conditions of the parts under optimized operation mode with (original formulation) and without (conventional formulation) grain size constraints (we will refer to these as "Case A" and "Case B," respectively). We consider as a performance metric the energy input to the system per part processed. We see that this quantity has increased from 3.57 GJ in Case B to 4.03 GJ for Case A (a 12.57% change). Nevertheless, Case A represents the operating mode that requires minimum energy input to the system without violating product toughness requirement compared to all other heuristic based operation modes.

In order to control the austenite grain size, the temperature set points must be higher in zones 1 and 2 and lower in zones 3 and 4 in Case A compared to those in Case B. As a consequence, the parts are heated rapidly in the first two hours of processing and slowly in the remaining hours under the optimized operation mode compared to Case B. This results in the minimum and average temperatures of the parts to be higher during the first few hours of processing in Case A as seen in Figure 3.10, which leads to additional fuel consumption. The coefficient of variation of the parts at the exit of the furnace has decreased from 0.045 in Case B to 0.036 in Case A, i.e, the temperature is more uniform in Case A. The austenite transformation of the hotter regions of the parts happens quickly, as the maximum grain size increases from zero within the first hour of processing, in Case A (see Figure 3.8) compared to Case B (see Figure 3.9). Nevertheless, at the exit of the furnace, the maximum grain size is smaller (41.75 μm) in Case A, within the desired value of 50 μm, compared to the 83.67 μm in Case B, making the quenched product meet the toughness requirement. In both cases, the proportion of energy input to the system lost as exhaust is significant, suggesting that system reconfiguration by using a recuperator at the burner exhaust to preheat inlet fuel or air will improve energy efficiency.
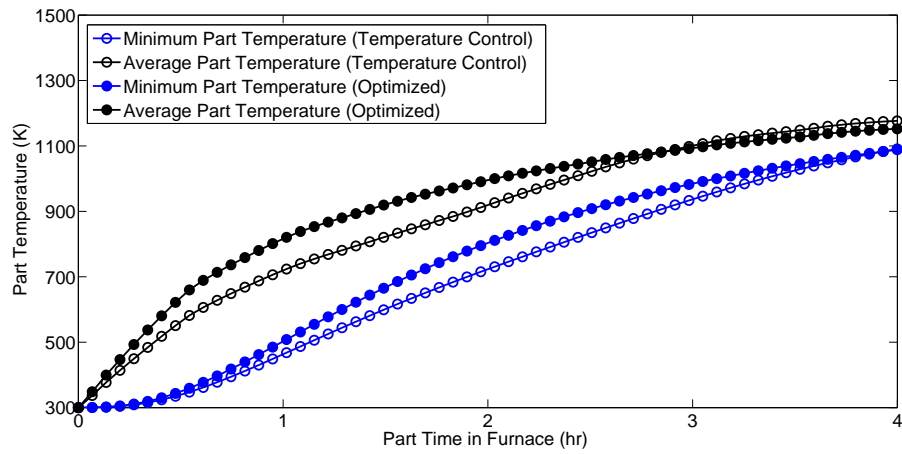
Figure 3.10: The minimum and average part temperatures of part number 20 as a function of the time of processing under optimized temperature set points and temperature control.

Chapter 4

Model predictive control

This chapter is based on material published in paper "H. S. Ganesh, T. F. Edgar, and M. Baldea. Model predictive control of the exit part temperature for an austenitization furnace. Processes, 4 (4):53, 2016" [32]. I am the primary contributor of the aforementioned paper.

The steady-state optimization procedure described in the previous chapter offers optimal operating conditions of the furnace in the nominal case. However, the optimality of the scheme is no longer guaranteed in the presence of disturbances. Therefore, in this chapter we develop and deploy model predictive control (MPC) as a supervisory control strategy to control part temperature at the exit of the furnace by varying the temperature set points of the feedback controllers.

4.1 Introduction

Model predictive control, originally developed to meet specialized control needs of oil refineries and power plants, has now found applications in food processing, pharmaceutical, polymer, automotive, metallurgical, chemical and aerospace industries [24, 96, 101]. The success of MPC can be attributed, as

summarized by Qin *et al.* [96], to its ability to solve complex multiple-input, multiple-output (MIMO) control problems,

1. without violating input, output and process constraints,

2. accounting for disturbances,

3. by preventing excess movement of input variables, and

4. by controlling as many variables as possible in case of faulty or unavailable sensors or actuators.

In this work, we describe the development and implementation of an MPC system for controlling the temperatures of the parts exiting an industrial austenitization furnace. The key to our approach is feedback control of the temperature of the metal parts (which can be measured in practice via a combination of infrared/pyrometric sensing and soft sensing/state observation). We show that in this manner the energy usage of the system is reduced considerably compared to the current regulatory control scheme (which is effectively open-loop with respect to product temperatures). To this end, we rely on the radiation-based nonlinear model of the furnace developed in Heng *et al.* [48] to develop a hierarchical, multi-rate control structure, whereby the setpoints of regulatory controllers are set by a multiple input, single output MPC that is computed at a much lower frequency than the regulatory control moves.

Model predictive controller is implemented to control minimum part temperature at exit and prevent it from overheating by appropriately varying

the zone temperature set points of the feedback controller. Model predictive control uses a dynamical model of the process to predict the effect of future control actions by using the current state of the plant as the initial state [19, 41, 83, 99, 109]. The control algorithm usually uses a finite-impulse or step-response models to anticipate the future behavior of the process. Then, a control sequence is determined, subject to input, output and process constraints, so that the predicted response moves to the set point in an optimal manner and the first control in this sequence is sent to the plant. The entire calculation is repeated at subsequent control intervals. In order to obtain offset-free MPC, the real-time measurements of the process is also made use of along with the model predictions. Step response models are obtained by performing step tests on the detailed 2D model. For the purpose of MPC, in our system, there are four inputs: four zone temperature set points, and one output: the average of minimum part temperatures at exit.

4.2   Model predictive control development

In our system, model predictive control is implemented as a two layer hierarchy of control functions. The inner layer is the regulatory control that manipulates the mass flow rate of fuel to control the zone temperatures and in the outer later, the model predictive controller adjusts the temperature set points of the regulatory control to control the minimum temperatures of parts at exit. Note that the time interval for control action of model predictive control is larger than that of regulatory control. The block diagram of the

implementation of model predictive control on our heat treating furnace is shown in Figure 4.1.
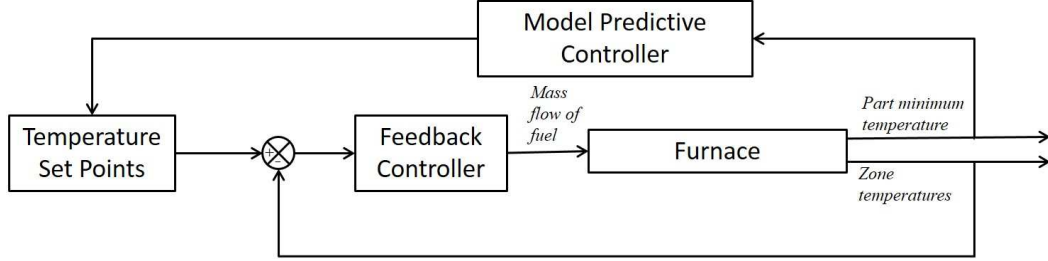
Figure 4.1: Block diagram for model predictive control implementation in the heat treating furnace. For the regulatory controller, zone temperatures are the controlled variables and the fuel flow rates to the burners are the manipulated variables. In case of the model predictive controller, the part minimum temperature at exit is the controlled variable and the zone temperature set points of the feedback controller are the manipulated variables.

Let $T_{sp,\psi}(k)$, $\forall\ \psi \in [1,4]$, be the temperature set point of zone ψ at sampling instant k and $T_{min}(k)$ be the part minimum temperature at exit of the furnace. Let $T_{sp,ss,\psi}$, $\forall\ \psi \in [1,4]$ be the steady-state temperature set point of zone ψ and $T_{min,ss}$ be the steady-state part minimum temperature. Additionally, let $y(k)$ be the deviation variable of part minimum temperature at time instant k, defined as: $y(k) \triangleq T_{min}(k) - T_{min,ss}$ and $u_\psi(k)$ be the deviation variable of zone ψ temperature set point at k, defined as: $u_\psi(k) \triangleq T_{sp,\psi}(k) - T_{sp,ss,\psi}$, $\forall\ \psi \in [1,4]$.

Next, we explain the model predictive control algorithm that uses a step-response model for predicting future outputs for a four-input (four zone temperature set points), single-output (exit part minimum temperature) pro-

58

cess and solves a quadratic program that minimizes the weighted prediction error and the weighted change in manipulated variables at each control time step [109].

4.2.1 Step-response model

The step-response model of a stable process with four inputs and one output can be written as:

$$
\begin{aligned}
y(k+1) = y(0) &+ \sum_{i=1}^{N-1} S_{1,i}\Delta u_1(k-i+1) + S_{1,N}u_1(k-N+1) \\
&+ \sum_{i=1}^{N-1} S_{2,i}\Delta u_2(k-i+1) + S_{2,N}u_2(k-N+1) \\
&+ \sum_{i=1}^{N-1} S_{3,i}\Delta u_3(k-i+1) + S_{3,N}u_3(k-N+1) \\
&+ \sum_{i=1}^{N-1} S_{4,i}\Delta u_4(k-i+1) + S_{4,N}u_4(k-N+1)
\end{aligned}
\tag{4.1}
$$

where $y(k+1)$ is the output variable at the $k+1$ sampling instant, $y(0)$ is the initial value of the output variable, and $\Delta u_\psi(k-i+1)$ for $\psi \in [1,4]$ denotes the change in the input ψ from one sampling instant to the next: $\Delta u_\psi(k-i+1) = u_\psi(k-i+1) - u_\psi(k-i)$. Both u and y are deviation variables defined earlier in this paper. The model parameters are the N step-response coefficients, $S_{\psi,i}$ to $S_{\psi,N}$, for each input ψ, $\forall \psi \in [1,4]$. Therefore, the total number of step-response coefficients are $4N$, where N is selected based on the process time constants.

4.2.1.1   Step-response coefficients calculation

Here, we describe the step-by-step algorithm for calculating the step response coefficients, $S_{1,1}$ to $S_{1,N}$, that relate the output variable $y(k)$ with the first input variable $u_1(k)$. To obtain the rest of the step response coefficients, $S_{\psi,1}$ to $S_{\psi,N}$, $\forall \, \psi \in [2, 4]$, the same procedure described below is followed.

S.1 Simulate the furnace under feedback control using heuristic zone temperature set points (ref: Heng *et al.*). These set points are the steady state values of the input variables $T_{sp,ss,\psi}$, $\forall \, \psi \in [1, 4]$.

S.2 When the furnace reaches a steady-state operating regime, and if there is a part at the exit of the furnace, set the value of k as zero and give a step input of magnitude ΔT_{step} to zone 1 temperature set point $T_{sp,1}(0)$. Note that this steady-state operating regime of the furnace exhibits periodic oscillations in furnace heat duties and temperatures due to periodic input of cold parts to the furnace and periodic removal of hot parts from the furnace. The deviation variable of the first input $u_1(0)$, used in the step-response model (eq. (4.1)) is the difference between the zone 1 temperature set point and its steady state value, which is same as the magnitude of step change: $u_1(0) = T_{sp,1}(0) - T_{sp,ss,1} = \Delta T_{step}$. Moreover, the measured minimum temperature of the part that is exiting the furnace is its steady state value: $T_{min}(0) = T_{min,ss}$. Hence, the output deviation variable: $y(0) = T_{min}(0) - T_{min,ss} = 0$.

60

S.3 When the next part exits the furnace, increment the value of k by 1 and measure its minimum temperature $T_{min}(k)$. The output deviation variable used in the step-response model (eq. (4.1)) is the difference between the measured temperature and its steady state value: $y(k) = T_{min}(k) - T_{min,ss}$.

S.4 Repeat S.3 for all the subsequent parts processed under the steady-state operating regime of the furnace.

S.5 Note that $\Delta u_1(k) = 0$, $\forall\, k \neq 0$ and $\Delta u_1(0) = \Delta T_{step}$. Also, $\Delta u_\psi(k) = 0$, $\forall\, k$ and $\psi \in [2, 4]$. Under these conditions, the step-response coefficients in eq. (4.1) are: $S_{1,i} = y(i)/\Delta T_{step}$, $\forall\, i \in [1, N]$.

The response of the output variable $y(k)$ for a step input ΔT_{step} of 20 K in each zone temperature set point is shown in Figure 4.2. The furnace takes about 25 hours to process a batch of 40 parts with part residence time being roughly 4 hours. The time difference between the exit of successive parts is the control time step Δt_{MPC}, which is around 32 minutes. The design variable N, which is the number of step-response coefficients for each control input was taken as 19. The step-response coefficients can be calculated from the step-response data in Figure 4.2 using the method described in S.5. It can be inferred from Figure 4.2 that zone 3 temperature set point has the dominant effect on the part exit temperature and zone 1, the least.
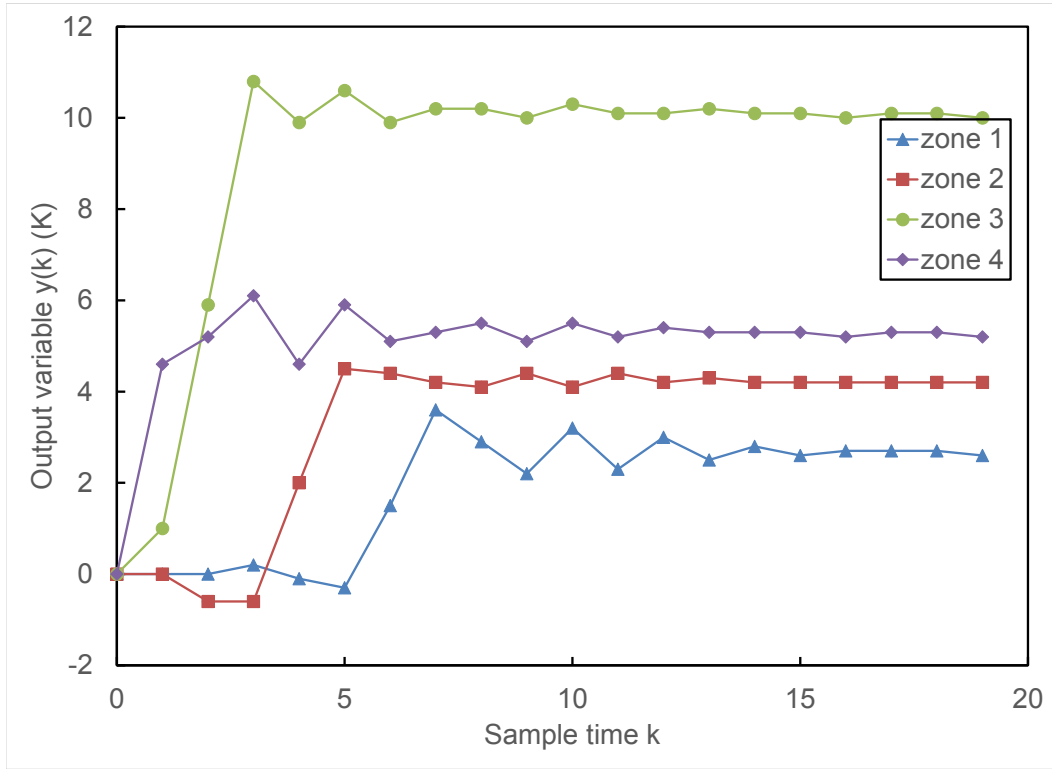
Figure 4.2: The response of the output variable $y(k)$ (deviation variable of part minimum temperature at exit) for a step input ΔT_{step} of 20 K for each of the zone temperature set points. k is the sampling time that increments with every control time step of around 32 minutes.

4.2.2 Model predictions

Let $\hat{y}(k+1)$ denote the prediction of $y(k+1)$ that is made at the current sampling instant k. Then, the output prediction of the next sampling instant can be obtained from eq. (4.1) by replacing $y(k+1)$ with $\hat{y}(k+1)$:

$$\hat{y}(k+1) = \sum_{i=1}^{N-1} S_{1,i}\Delta u_1(k-i+1) + S_{1,N}u_1(k-N+1)$$
$$+ \sum_{i=1}^{N-1} S_{2,i}\Delta u_2(k-i+1) + S_{2,N}u_2(k-N+1)$$
$$+ \sum_{i=1}^{N-1} S_{3,i}\Delta u_3(k-i+1) + S_{3,N}u_3(k-N+1) \qquad (4.2)$$
$$+ \sum_{i=1}^{N-1} S_{4,i}\Delta u_4(k-i+1) + S_{4,N}u_4(k-N+1)$$

Now, rearranging the above equation by separating out the effect of current manipulated input $u(k)$ from past inputs $u(i)$, $\forall\, i < k$ yields:

$$\hat{y}(k+1) = S_{1,1}\Delta u_1(k) + S_{2,1}\Delta u_2(k) + S_{3,1}\Delta u_3(k) + S_{4,1}\Delta u_4(k)$$
$$+ \sum_{i=2}^{N-1} S_{1,i}\Delta u_1(k-i+1) + S_{1,N}u_1(k-N+1)$$
$$+ \sum_{i=2}^{N-1} S_{2,i}\Delta u_2(k-i+1) + S_{2,N}u_2(k-N+1)$$
$$+ \sum_{i=2}^{N-1} S_{3,i}\Delta u_3(k-i+1) + S_{3,N}u_3(k-N+1) \qquad (4.3)$$
$$+ \sum_{i=2}^{N-1} S_{4,i}\Delta u_4(k-i+1) + S_{4,N}u_4(k-N+1)$$

The above equation can be rewritten as:

$$\hat{y}(k+1) = S_{1,1}\Delta u_1(k) + S_{2,1}\Delta u_2(k) + S_{3,1}\Delta u_3(k) + S_{4,1}\Delta u_4(k) + \hat{y}^o(k+1) \quad (4.4)$$

where $\hat{y}^o(k+1)$ is the *predicted unforced response*, since it represents the predicted response when there are no current or future control actions. It is defined as:

$$
\begin{aligned}
\hat{y}^o(k+1) \triangleq & \sum_{i=2}^{N-1} S_{1,i}\Delta u_1(k-i+1) + S_{1,N}u_1(k-N+1) \\
& + \sum_{i=2}^{N-1} S_{2,i}\Delta u_2(k-i+1) + S_{2,N}u_2(k-N+1) \\
& + \sum_{i=2}^{N-1} S_{3,i}\Delta u_3(k-i+1) + S_{3,N}u_3(k-N+1) \\
& + \sum_{i=2}^{N-1} S_{4,i}\Delta u_4(k-i+1) + S_{4,N}u_4(k-N+1)
\end{aligned}
\tag{4.5}
$$

Now, we define vectors of predicted responses and predicted unforced responses for the next P sampling instants as:

$$
\hat{\boldsymbol{Y}}(k+1) \triangleq col[\hat{y}(k+1), \hat{y}(k+2), \dots, \hat{y}(k+P)]
\tag{4.6}
$$

$$
\hat{\boldsymbol{Y}}^o(k+1) \triangleq col[\hat{y}^o(k+1), \hat{y}^o(k+2), \dots, \hat{y}^o(k+P)]
\tag{4.7}
$$

where *col* denotes a column vector. Next, we first group the inputs into a vector $\boldsymbol{u}(k) \triangleq col[u_1(k), u_2(k), u_3(k), u_4(k)]$ and then define a vector of control actions for the next M sampling instants as:

$$
\Delta\boldsymbol{U}(k) \triangleq col[\Delta\boldsymbol{u}(k), \Delta\boldsymbol{u}(k+1), \dots, \Delta\boldsymbol{u}(k+M-1)]
\tag{4.8}
$$

The key design parameters of MPC are the predicted horizon P and the control horizon M. Equation (4.4) can be expressed in a vector-matrix notation using eqs. (4.6) to (4.8) as:

$$\hat{\boldsymbol{Y}}(k+1) = \boldsymbol{S}\Delta\boldsymbol{U}(k) + \hat{\boldsymbol{Y}}^o(k+1) \qquad (4.9)$$

where $\boldsymbol{S}$ is a $P \times M$ dynamic matrix of step-response coefficients, defined as:

$$\boldsymbol{S} \triangleq \begin{bmatrix} \boldsymbol{S}_1 & \boldsymbol{0} & \ldots & \boldsymbol{0} \\ \boldsymbol{S}_2 & \boldsymbol{S}_1 & \ldots & \vdots \\ \vdots & \vdots & \ddots & \boldsymbol{0} \\ \boldsymbol{S}_M & \boldsymbol{S}_{M-1} & \ldots & \boldsymbol{S}_1 \\ \boldsymbol{S}_{M+1} & \boldsymbol{S}_M & \ldots & \boldsymbol{S}_2 \\ \vdots & \vdots & \ddots & \vdots \\ \boldsymbol{S}_P & \boldsymbol{S}_{P-1} & \ldots & \boldsymbol{S}_{P-M+1} \end{bmatrix}$$

where $\boldsymbol{S}_i$ is the row vector of step-response coefficients for the ith time step:

$$\boldsymbol{S}_i \triangleq \begin{bmatrix} S_{1,i} & S_{2,i} & S_{3,i} & S_{4,i} \end{bmatrix}$$

For offset free MPC, the latest measurement $y(k)$ is made use of to improve the model predictions and this strategy is called *output feedback*. Adding *bias correction*, $[y(k) - \hat{y}(k)]\boldsymbol{1}$, to the predicted response, $\hat{\boldsymbol{Y}}(k+1)$, yields the *corrected prediction*, $\tilde{\boldsymbol{Y}}(k+1)$, defined as:

$$\tilde{\boldsymbol{Y}}(k+1) = \boldsymbol{S}\Delta\boldsymbol{U}(k) + \hat{\boldsymbol{Y}}^o(k+1) + [y(k) - \hat{y}(k)]\boldsymbol{1} \qquad (4.10)$$

where $\boldsymbol{1}$ is a column vector of length P with each element having a value of one.

4.2.3 Predicted error

Let $y_{sp}(k+1)$ be the set-point of the model predictive controller at sampling instant $k+1$. Then, the set-point vector over the prediction horizon P, $\boldsymbol{Y}_{sp}(k+1)$, is defined as:

$$\boldsymbol{Y}_{sp}(k+1) \triangleq col[y_{sp}(k+1), y_{sp}(k+2), \ldots, y_{sp}(k+P)] \tag{4.11}$$

In our case, the set point of model predictive controller, the deviation variable of part minimum temperature at exit $(y_{setpoint})$, does not vary with time. Hence, $\boldsymbol{Y}_{sp}(k+1)$ is simply a constant vector of length P expressed as:

$$\boldsymbol{Y}_{sp}(k+1) = y_{setpoint}\boldsymbol{1} \tag{4.12}$$

The *predicted error* vector is defined as:

$$\hat{\boldsymbol{E}}(k+1) \triangleq \boldsymbol{Y}_{sp}(k+1) - \tilde{\boldsymbol{Y}}(k+1) \tag{4.13}$$

4.2.4 Optimization formulation

The vector of control actions $\Delta\boldsymbol{U}(k)$ is calculated at each sampling instant k by minimizing the objective function shown below, subject to the input, output and process constraints. The optimization formulation is:

$$\underset{\Delta \boldsymbol{U}(k)}{\text{minimize}} \quad \boldsymbol{J} = \hat{\boldsymbol{E}}(k+1)^T \boldsymbol{Q} \hat{\boldsymbol{E}}(k+1) + \Delta \boldsymbol{U}(k)^T \boldsymbol{R} \Delta \boldsymbol{U}(k)$$

subject to $\quad u_\psi(k+j) \geq u_{min}, \ \psi \in [1,4] \text{ and } j \in [0, k+M-1]$

$\qquad\qquad u_\psi(k+j) \leq u_{max}, \ \psi \in [1,4] \text{ and } j \in [0, k+M-1]$

$\qquad\qquad u_\psi(k+j) - u_{\psi+1}(k+j) \leq u_{diff}, \ \psi \in [1,3] \text{ and } j \in [0, k+M-1]$

$\qquad\qquad \textit{System Model}$

$$(4.14)$$

where $\boldsymbol{Q}$ and $\boldsymbol{R}$ are the output and input weighting matrices respectively that allow the output and input variables to be weighted according to their relative importance. u_{min} and u_{max} are the lower and upper bounds of the zone temperature set points u_ψ, $\psi \in [1,4]$ respectively, and u_{diff} is the enforced temperature difference between subsequent zones in order to prevent loss of heat from parts to the furnace while processing. Note that u_{min}, u_{max} and u_{diff} are deviation variables. Once $\Delta \boldsymbol{U}(k)$ is computed, the furnace simulation proceeds for the control time interval Δt_{MPC}, at which the sample time is updated from k to $k+1$ and the entire procedure from eqs. (4.1) to (4.14) is repeated.

4.3 Operation under model predictive control

We simulate the furnace for a batch of forty parts using the same parameters and operating conditions as those in Heng *et al.* [48] under temperature feedback control. Additionally, instead of operating at a constant heuristic temperature set points suggested by the operators of the plant, the supervi-

sory model predictive controller changes the zone temperature set points to control the part temperature at exit of the furnace (see Figure 4.1). The lower layer temperature tracking controllers use the above trajectory as the control target. At this lower level, zone temperatures are sensed and are compared against the temperature set points determined by the higher level model predictive controller. A linear control strategy is adopted wherein the fuel mass flow rate of a zone is manipulated to minimize the error between the measured value of the respective zone temperature and its set point determined by the MPC. All the burners in a zone are adjusted simultaneously, i.e, the furnace has only four control valves for regulatory control. In practice, a butterfly valve is used to manipulate the fuel flow rate. This valve does not close fully, i.e., the mass flow rate of fuel to the burners does not drop below a certain lower limit. Also, when the valve is fully open, the upper bound of fuel flow rate is reached. Each control zone operates independently of other zones. However, adjustments to fuel flow rate of one zone will affect the temperatures of other zones due to long range radiation interactions. The furnace operating conditions and the parameters used in the simulation are listed in Table 4.1. The local control sampling time is 4 minutes for the 25 hours furnace operation. The upper level model predictive controller functions at a much longer time interval, with a sampling time of 32.5 minutes, correlated with the rate of input/output of parts to the furnace. Within this time period, there are about 8 control moves for the inner level temperature tracking controller to bring the zone temperatures closer to the trajectory determined by the MPC.

68

Furnace details	
Length of the furnace	16 m
Height of the furnace/length of the side walls	2 m
Length of each discretized furnace surface except the side walls	0.25 m
Total number of furnace surfaces	130
Length of a part	1.25 m
Ordinate of a part	0.75 m
Height of a part	0.5 m
Process conditions	
Number of parts processed	40
Inlet temperature of parts	300 K
Inlet temperature of blanket gas	400 K
Number of points in x-direction for Crank-Nicolson method	6
Number of points in y-direction for Crank-Nicolson method	6
Total time of furnace operation	25 hrs
Feedback control time interval	4 min
Model predictive control details	
Target minimum part temperature at exit	1088 K
Lower bound of temperature set points	900 K
Upper bound of temperature set points	1300 K
Temperature set point difference between subsequent zones	30 K
Model predictive control time interval	32.5 min

Table 4.1: List of parameters used in the heat treating furnace simulation under model predictive control.

The setpoint for the MPC controller is the part minimum temperature at exit of the furnace. Note that non-contact ultrasonic measurements can be used to measure the value of minimum part temperature while deploying MPC on the actual furnace operating at the industrial partner [69, 107, 135]. We use a constant target value of 1088 K, a temperature that ensures complete transformation from pearlite (mixture of ferrite and cementite) to austenite for a steel with 0.85% carbon content.

As a base case, we consider a simulation where only the regulatory

control layer is employed, with the temperature set points, $T_{sp,ss,\psi} \; \forall \; \psi \in [1,4]$, were taken to be same as the heuristic temperature set points of Heng *et al.* [48]: 1000 K, 1150 K, 1200 K, 1250 K for zones 1 to 4 respectively. Furnace operation under these set points results in an exit part minimum temperature at constant-input and constant-output operating regime of 1126 K. This is the steady state value of the output variable $T_{min,ss}$.
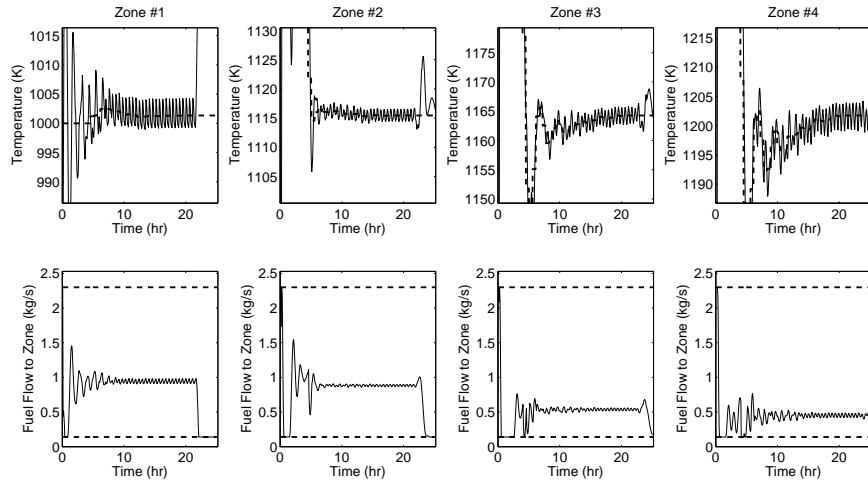
Figure 4.3: Zone temperatures and mass flow rate of fuel to the burners as a function of time for zones 1 to 4 (solid lines). The dashed lines in the plots of top row indicate the zone temperatures setpoints and the dashed lines in the plots of bottom row indicate the upper and lower bounds of fuel flow rate to the burners.

Then, we consider the furnace operation under the proposed MPC scheme. Figure 4.3 illustrates the variation of output and input variables with respect to time of furnace operation in this case. The model predictive controller is turned on only after about 4 hours of furnace operation when the

first part exits the furnace, at which point the furnace begins to operate in a regime characterized by constant rates of input and output of parts. The plots in the top row of Figure 4.3 show the zone temperature setpoints (as set by the MPC) and the zone temperatures maintained by the regulatory control layer at these setpoints within minimal variations (in general within 5 K). The step-response plot in Figure 4.2 indicates that zone 3 and zone 4 temperature set points have dominant effects on exit part temperature. This aspect is also reflected in Figure 4.3, where it can be seen that the set point variations are higher in zones 3 and 4 to meet the target. It is also observed that the zone temperatures exhibit periodic oscillations around their set points. This effect can be attributed to the periodic entry of cold parts into the furnace in zone 1 and periodic removal of hot parts from the furnace in zone 4. The thermal gradient is the maximum when a cold part enters the furnace. Therefore, the part acts as a heat sink resulting in a rapid decrease in the temperature of zone 1. This disturbance is propagated to other zones of the furnace due to long range zone-to-zone radiation interactions. Moreover, additional harmonics in the temperature variations are caused by parts exiting the furnace. The plots in the bottom row of Figure 4.3 show the corresponding changes in the manipulated variable, i.e., the mass flow rate of fuel to the burners. The dashed lines in these plots represent the lower and upper bounds of the fuel flow rate.

Figure 4.4 shows the exit conditions of all the processed parts exiting the furnace sequentially. The quantities plotted are the total change in part enthalpy and its temperature distribution details. The red curve represents the

71
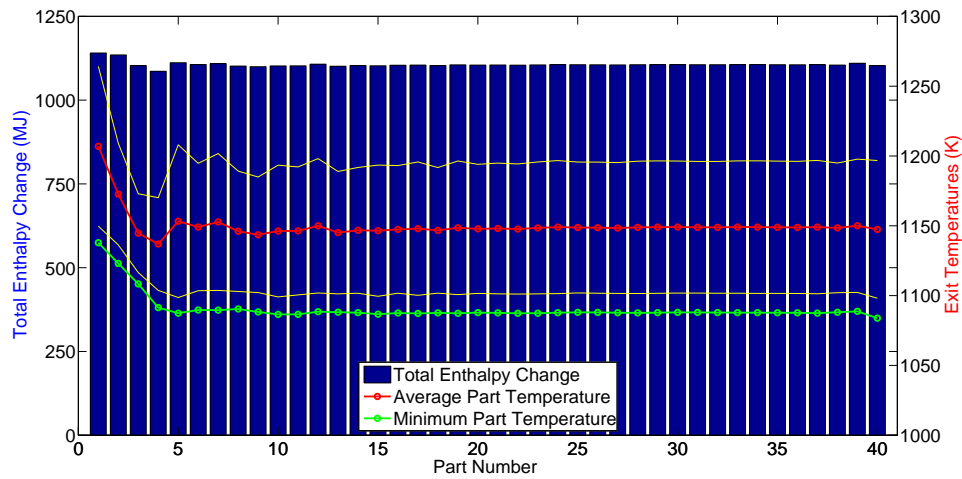
Figure 4.4: Part exit conditions of all the 40 parts processed under model predictive control. The yellow lines indicate the standard deviation of the part exit temperatures from its mean. The model predictive controller is turned on immediately after the first part exits the furnace. The variations in the total enthalpy change of the first five parts is due to the MPC varying the set points of the feedback controllers to drive the minimum part temperatures to their target The MPC controller keeps part exit temperatures relatively stationary once the target is reached.

average of part temperature distribution of all parts at exit, yellow curves are its standard deviation and the green curve is the minimum of the temperature distribution of all the parts at exit, which is the target for the model predictive controller. The temperature set point changes made by the model predictive controller drive the part minimum temperature from around 1125 K for the first part to the target value of 1088 K. The two-tiered control strategy maintains the exit conditions relatively stationary once part minimum temperature reaches its target.
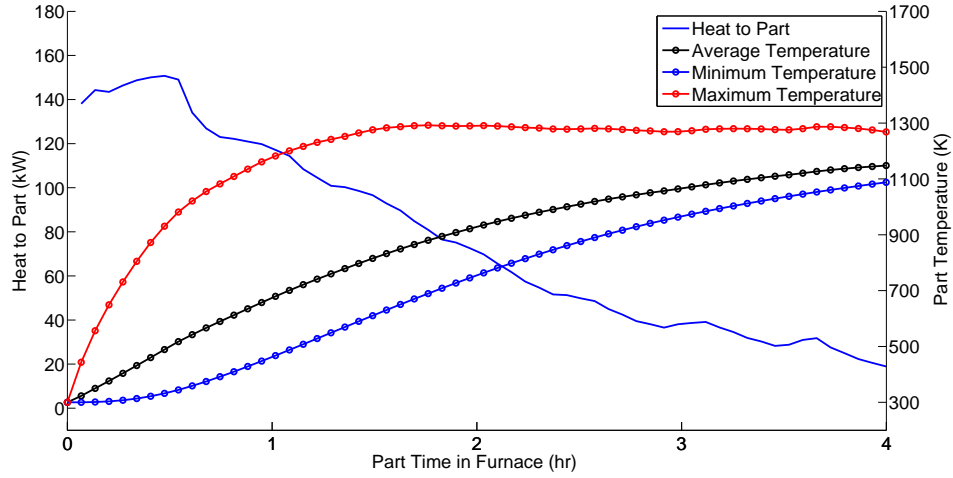
Figure 4.5: Heat input to the 20th part and its temperature distribution details as a function of its time (and thus position) of processing.

Finally, we plot the heat input to the 20th part and the parameters of the part temperature distribution with respect to processing time in Figure 4.5. Note that a part's residence time is roughly 4 hours. Therefore, the time spent within the furnace also corresponds to the zone in which the part is getting heated. As expected, the amount of heat transferred to a part decreases with time since as the part becomes hotter the temperature difference between the part and the burners becomes smaller. The maximum temperature of a part is at its boundary/exterior. Intuitively, the minimum temperature occurs at the interior that is heated only via conduction and hence the corresponding temperature gradually raises to its target value at exit of the furnace.

4.3.1 Energy efficiency comparison

In Table 4.2, we compare the furnace operation under regulatory control with heuristic zone temperature set points reported in Heng *et al.* [48] and under model predictive control. In heuristic operation mode, the minimum temperature of parts at exit, 1126 K, is higher than the desired value of 1088 K. This overheating of parts results in the furnace consuming additional fuel. Furthermore, overheating of parts results in austenite grain size growth, which adversely affects the toughness of the quenched product. However, under the two layer hierarchical control operating mode, the part exit temperature is maintained at its desired value of 1088 K. The energy metric we compare is the total energy input to the furnace per part processed. We see that the furnace operation under model predictive control requires 5.3% less energy than that under heuristic operation scenario. The energy efficiency gain is mainly due to the lowered fuel use. Moreover, additional gains can be a consequence of a different nonlinear surface-to-surface radiation interactions due to changing zone temperature set points. The standard deviation of part temperatures is similar in both these operation modes. This means that the model predictive controller has maintained the minimum temperature of part at exit to its desired value without compromising the uniformity in heating. The distribution of energy input to the furnace to parts, exhaust, nitrogen and insulation are comparable for both these operation modes.

Naturally, the heuristically-determined temperature setpoints of the distributed control system are not optimal from an energy consumption point of view. This was noted in our previous work (Heng *et al.* [48]), where we

Heat Sources and Sinks	Heuristic Set Points	Model Predictive Control
Total Energy Input Per Part (GJ)	3.76 GJ	3.56 GJ
Part Minimum Temperature (K)	1126 K	1088 K
Temperature Standard Deviation (K)	52 K	46 K
Energy to Parts (%)	54.2%	54.3%
Energy Lost with the Exhaust (%)	42.7%	42.5%
Energy to Flowing Nitrogen (%)	0.5%	0.5%
Energy Through Insulation (%)	2.6%	2.7%

Table 4.2: Total energy input to the furnace and part temperature distribution at the exit of the furnace under heuristic operation mode of Heng *et al.* [48] and two-level hierarchical control. We also show the energy distribution of the heat input to process a batch of 40 parts.

proposed a model-based optimization strategy to determine the optimal set-points that would yield the desired part outlet temperature of 1088 K. This strategy offered (locally) optimal operation in the nominal case; however, the optimality of this approach is no longer guaranteed in the presence of disturbances. To illustrate this point, we consider a scenario where a slight change in the properties of the material being processed (specifically, a raise in thermal conductivity from 63 W/(m K) to 73 W/(m K)) occurs. Table 4.3 presents a comparison of the furnace performance under the distributed control scheme with optimized setpoints as proposed by Heng *et al.* [48], and operation under MPC. As expected, the MPC is capable of maintaining the part exit temperatures at the desired value, while the distributed scheme (which is in effect open-loop with regard to controlling *part* temperatures) leads to a significant offset.

Heat Sources and Sinks	Optimized Set Points	Optimized Set Points with Disturbance	MPC with Disturbance
Total Energy Input Per Part (GJ)	3.58 GJ	3.63 GJ	3.49 GJ
Part Minimum Temperature (K)	1088 K	1117 K	1088 K
Temperature Standard Deviation (K)	52 K	42 K	37 K
Energy to Parts (%)	54.4%	54.5%	54.5%
Energy Lost with the Exhaust (%)	42.4%	42.4%	42.3%
Energy to Flowing Nitrogen (%)	0.5%	0.5%	0.5%
Energy Through Insulation (%)	2.6%	2.6%	2.7%

Table 4.3: Total energy input to the furnace and part temperature distribution at the exit of the furnace under optimized operation mode of Heng *et al.* [48] and MPC in the presence of disturbances. For the nominal performance of MPC, see Table 4.2

Chapter 5

Heat integration using recuperators

This chapter is based on material published in papers "H. S. Ganesh, O. A. Ezekoye, T. F. Edgar, and M. Baldea. Heat integration and operational optimization of an austenitization furnace using concentric-tube radiant recuperators. AIChE Journal, 2018. doi: 10.1002/aic.16414" [39] and "H. S. Ganesh, O. A. Ezekoye, T. F. Edgar, and M. Baldea. Improving energy efficiency of an austenitization furnace by heat integration and real-time optimization. In 2018 IEEE International Conference on Automation, Quality and Testing, Robotics (AQTR). IEEE, 2018. doi: 10.1109/AQTR.2018.8402763" [40]. I am the primary contributor of the aforementioned papers.

5.1   Motivation

Furnace simulations [27, 32, 36, 38, 48] and observations in the plant show that more than 40% of the available heat is wastefully discharged with the burner exhaust flue gases. In order to lower the heat loses, this work focuses on the influence of heat integration using a *recuperator*, a special purpose indirect-contact heat exchanger, on fuel savings and overall furnace system dynamics. The recuperators recover some of the waste heat from the burner

exhaust to heat the air fed to the burners (see Figure 5.2). The pre-heated air requires less fuel for combustion thus contributing to energy savings. Since the exhaust gases exit the burners at temperatures above 1000 K, long-range radiation interactions play a dominant role in heat exchange. The novel contribution of this work is the modeling of a multi-tube recuperator capturing essential physics (local convection, long-range radiation), and using the model for energy-focused analysis and optimization of the furnace operation. The deployment of recuperators shows significant reduction in fuel consumption. Furthermore, the optimal operating conditions of the furnace were identified using surrogate models and real-time optimization for energy efficiency improvement.

5.2 Radiant recuperator modeling

Recuperators are classified based on the material, i.e., ceramic or metallic, or the dominant mode of heat transfer, i.e., convection or radiation [42]. The temperatures of the exhaust gases that exit the burners of the heat treating furnace considered in this work are above 1000 K. Hence, the heat transfer between the exhaust gases and inlet air to the burners is predominantly made by radiation. This type of recuperator is called a *radiant recuperator*.

A shell and tube type recuperator is being used at our industrial partner (Figure 5.2). The detailed schematic of the recuperator is shown in Figure 5.3. Every tube has an additional concentric smaller pipe within it. A recuperator is fitted at the exhaust section of each burner. In this ensemble, the flue gases
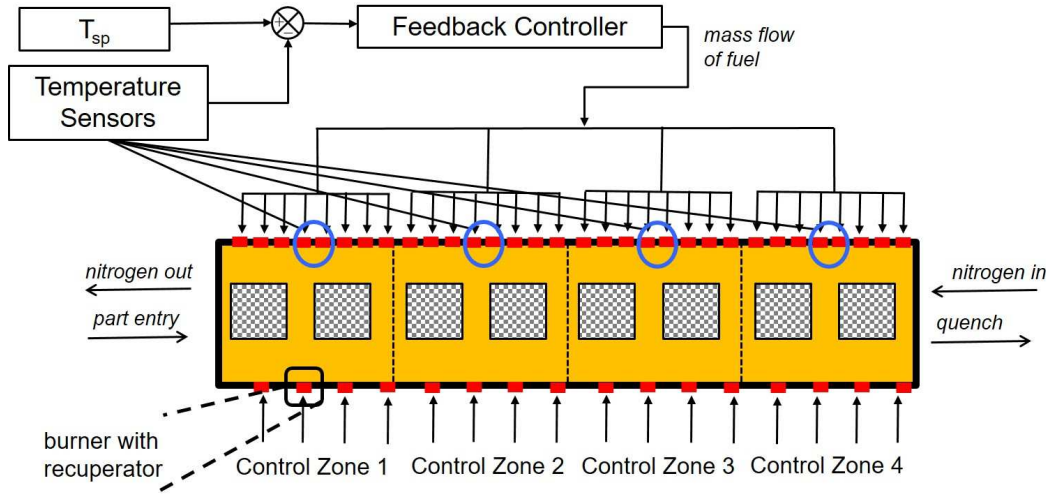
Figure 5.1: Schematic of the configuration of the austenitization furnace under temperature feedback control. The parts, represented by the hatched rectangles, enter from the left and exit at the right. Inert blanket gas (nitrogen), on the other hand, flows in counter-current direction from right to left. The red lines represent radiant tube burners and the black lines represent the insulation walls. A recuperator, a special purpose non-contact heat exchanger that transfers heat from the burner exhaust to preheat the inlet air to the burners, is attached to every burner to improve fuel efficiency. The vertical dotted lines represent boundaries between two temperature control zones. The temperature sensors for each zone are placed at the locations circled in blue.

pass through the shell side of the recuperator. The air flows in though the center pipe in every tube and flows out through the annulus. For modeling purposes, the geometry of this recuperator is simplified as a pipe and two concentric annular ducts as shown in Figure 5.4.

The recuperator model comprises of three surfaces (numbered horizontally in Figure 5.4): surface 1 is the wall between the flue gas channel and the insulation, surface 2 is the wall between the flue gas and the hot air, and
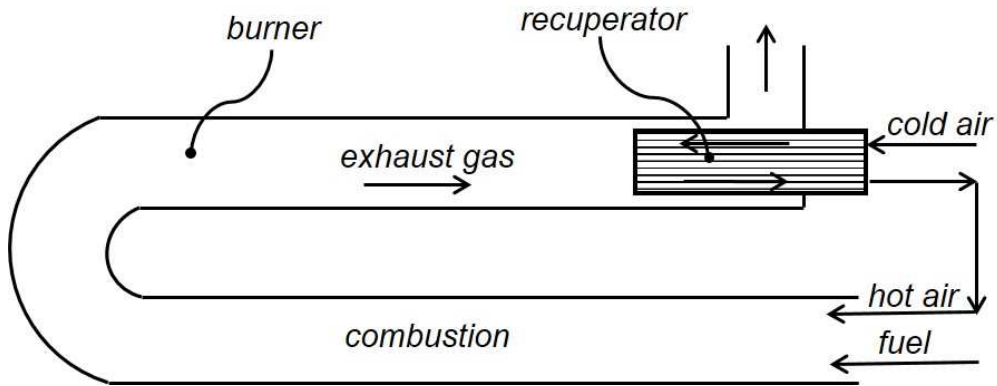
Figure 5.2: Schematic of a U-tube burner with recuperator. The shell-and-tube type recuperator is attached to the exhaust gas section. The exhaust gases flow through the shell side. The hot air is mixed with fuel (natural gas) and fed to the burner inlet for combustion.

surface 3 is the wall between the hot air and the cold air channels. The values of the parameters for the recuperator are provided in Table 5.1. The following assumptions are made in the model:

S1. The recuperator operates at steady-state.

S2. The recuperator is evenly discretized into a set of elements in the axial direction, numbered vertically in Figure 5.4 [110–112]. The gas in each element is assumed to be well mixed (and hence isothermal).

S3. The metallic surfaces in each element are assumed to be isothermal since they are thin and highly conductive.

S4. The exhaust gases are clean or free of significant particulate matter. Therefore, gas-to-surface radiation heat transfer is negligible. The gas
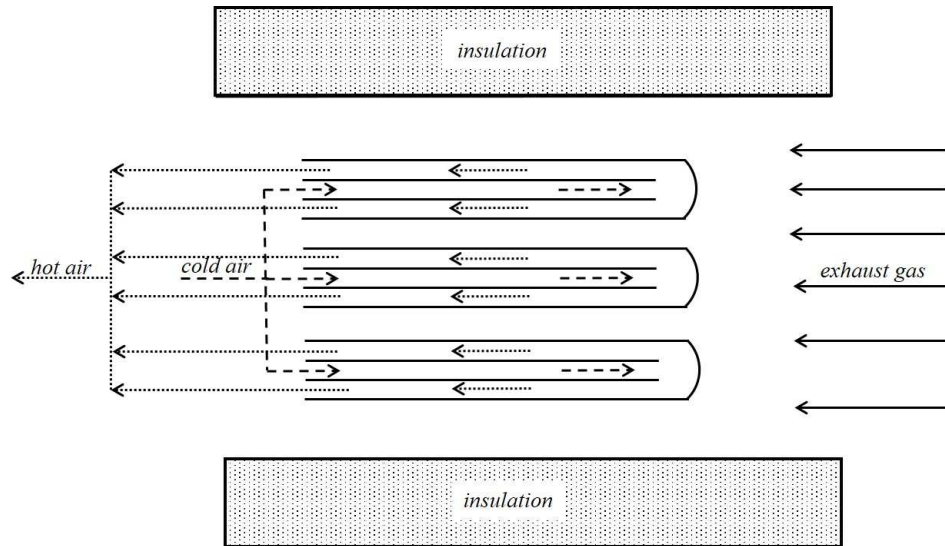
Figure 5.3: Schematic of the shell and tube-inside-tube recuperator. Only three tubes are shown for easy representation. The recuperator is installed at the exit of the radiant tube burner. The exhaust gas flows through the shell side. The air flows through the tubes. In a tube, inlet air flows through the center pipe and flows backwards through the annulus and then exits the recuperator. The heated air is now sent to the inlet section of the same burner where it gets mixed with fuel for combustion. A thick insulation separates the recuperator from the surroundings.

exchanges heat with the surfaces only via convection. The surfaces transfer heat to other surfaces via radiation.

In order to determine the temperature profile of the recuperator, the heat balance and heat transfer equations (presented below) need to be solved simultaneously. The wall temperatures are represented by $T_{w,j,i}$, where j is the index for the surface and i is the index for the element for that surface. The flue gas elements are represented by $T_{FG,i}$, the hot air elements by $T_{HA,i}$

and the cold air elements by $T_{CA,i}$.

Surface 1 exchanges heat with the ambient air by conduction through the insulation and then convection from the outer surface of the insulation. Note that convection and conduction heat transfer are local, i.e., they occur predominantly in the radial direction. The radiation interactions, however, are global, i.e., they occur in the radial as well as axial directions and impact multiple elements.

For an element i in the flue gas channel, the energy balance equation is:

$$\dot{m}_{FG}C_{p,FG}(T_{FG,i} - T_{FG,i+1}) = h_{FG}A_1(T_{FG,i} - T_{w,1,i}) + h_{FG}A_2(T_{FG,i} - T_{w,2,i})$$

$$(5.1)$$

where $\dot{m}_{FG}$ is the mass flow rate of the flue gas, $C_{p,FG}$ is the heat capacity of the flue gas, and h_{FG} is the heat transfer coefficient of the flue gas. A_1 and A_2 are the areas of an element in surface 1 and surface 2 respectively. The energy balance equations for an element i in the cold and hot air sections are:

$$\dot{m}_{air}C_{p,air}(T_{CA,i} - T_{CA,i+1}) = h_{air}A_3(T_{w,3,i+1} - T_{CA,i+1}) \qquad (5.2)$$

$$\dot{m}_{air}C_{p,air}(T_{HA,i+1} - T_{HA,i}) = h_{air}A_2(T_{w,2,i} - T_{HA,i}) + h_{air}A_3(T_{HA,i} - T_{w,3,i})$$

$$(5.3)$$
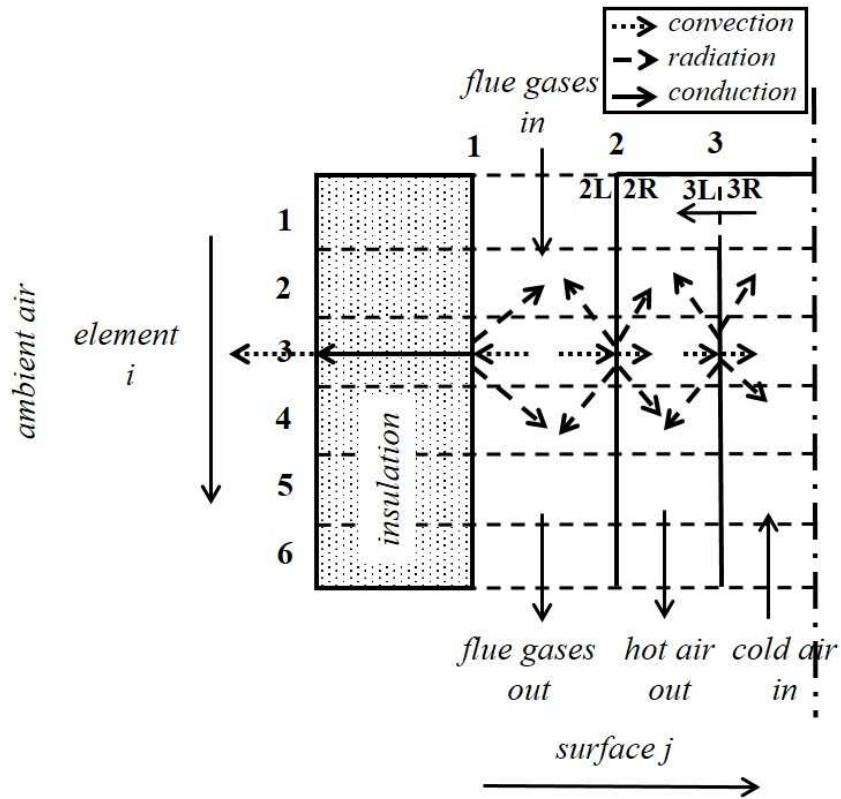
Figure 5.4: Schematic of the structure of the radiation model for a recuperator featuring a pipe and two concentric annular ducts. The dash dot line on the right is the axis of symmetry. The cold air flows though the inner pipe and exits though the first annular channel. The flue gases flow though the outermost annular channel. A thick insulation is placed between the flue gas channel and the ambient air. The convection and conduction interactions shown by the dotted and thick solid arrows, respectively, occur in the radial direction only. The surface-to-surface long-range radiation interactions shown by the dashed arrows, however, also occur in the axial direction. Convective heat transfer takes place between a gas and surface elements. Heat is transferred through the insulation via conduction. The heat transfer directions shown in this figure may change depending upon the instantaneous temperature profile of the recuperator.

where $\dot{m}_{air}$ is the mass flow rate of the air, $C_{p,air}$ is the heat capacity of the air, h_{air} is the heat transfer coefficient of the air, and A_3 is the area of an element in surface 3. The above relations capture convective heat transfer between the gas and the surfaces in the radial direction. As mentioned earlier, the surface-to-surface radiation interactions are not strictly localized, i.e., they occur both in radial and axial directions. For different elements (i, i'), radiation interactions occur between the elements of surface 1 and the left side (in Figure 5.4) of surface 2. Similarly, surface 2 right (R) and surface 3 left (L) interact by radiation heat transfer. Also, the elements in the concave surface 3 (right) interact with each other and themselves via radiation. The radiation heat transfer rates for an element i in surfaces 1, 2L (left), 2R (right), 3L, and 3R are the following:

$$\sum_{j=1}^{N_{s1,s2L}} \frac{J_i - J_j}{(A_1 F_{i,j})^{-1}} = \frac{\sigma T_{w,1,i}^4 - J_i}{\frac{1-\epsilon_i}{\epsilon_i A_1}} \tag{5.4}$$

$$\sum_{j=1}^{N_{s1,s2L}} \frac{J_i - J_j}{(A_2 F_{i,j})^{-1}} = \frac{\sigma T_{w,2,i}^4 - J_i}{\frac{1-\epsilon_i}{\epsilon_i A_2}} \tag{5.5}$$

$$\sum_{j=1}^{N_{s2R,s3L}} \frac{J_i - J_j}{(A_2 F_{i,j})^{-1}} = \frac{\sigma T_{w,2,i}^4 - J_i}{\frac{1-\epsilon_i}{\epsilon_i A_2}} \tag{5.6}$$

$$\sum_{j=1}^{N_{s2R,s3L}} \frac{J_i - J_j}{(A_3 F_{i,j})^{-1}} = \frac{\sigma T_{w,3,i}^4 - J_i}{\frac{1-\epsilon_i}{\epsilon_i A_3}} \tag{5.7}$$

$$\sum_{j=1}^{N_{s3R,s3R}} \frac{J_i - J_j}{\left(A_3 F_{i,j}\right)^{-1}} = \frac{\sigma T_{w,3,i}^4 - J_i}{\frac{1-\epsilon_i}{\epsilon_i A_3}} \tag{5.8}$$

where slL and slR are the left side and right side of surface l respectively, $N_{sl,sm}$ is the number of elements in surfaces l and m, J_i is the radiosity of surface i from the side over which the summation is defined, A_l is the surface area of an element in surface l, ϵ_i is the emissivity of surface i, and $F_{i,j}$ is the view factor between surfaces i and j. Note that the radiosities J_i are different on both sides of the surface element for the middle surfaces 2 and 3, whereas the temperatures on both sides of the surface elements $T_{w,2,i}$ and $T_{w,3,i}$ are the same due to the isothermal surface assumption.

The radiation heat transfer rates can also be expressed from the overall heat balance relations as:

$$h_{FG} A_1 (T_{FG,i} - T_{w,1,i}) - \frac{T_{w,1,i} - T_{amb}}{\frac{\ln(r_{ins}/r_1)}{2\pi k_{ins} L_1} + \frac{1}{h_{amb} A_1}} = \sum_{j=1}^{N_{s1,s2L}} \frac{J_i - J_j}{\left(A_1 F_{i,j}\right)^{-1}} \tag{5.9}$$

$$h_{FG} A_2 (T_{FG,i} - T_{w,2,i}) = \sum_{j=1}^{N_{s1,s2L}} \frac{J_i - J_j}{\left(A_2 F_{i,j}\right)^{-1}} \tag{5.10}$$

$$h_{HA} A_2 (T_{w,2,i} - T_{HA,i}) = \sum_{j=1}^{N_{s2R,s3L}} \frac{J_i - J_j}{\left(A_2 F_{i,j}\right)^{-1}} \tag{5.11}$$

$$h_{CA} A_3 (T_{HA,i} - T_{w,3,i}) = \sum_{j=1}^{N_{s2R,s3L}} \frac{J_i - J_j}{\left(A_3 F_{i,j}\right)^{-1}} \tag{5.12}$$

$$h_{CA}A_3(T_{w,3,i} - T_{CA,i}) = \sum_{j=1}^{N_{s3R,s3R}} \frac{J_i - J_j}{(A_3 F_{i,j})^{-1}} \qquad (5.13)$$

where T_{amb} is the temperature of ambient air, r_{ins} is the radius of the recuperator including the insulation, r_1 is the radius of the cylinder upto surface 1, L_1 is the length of an element in surface 1, h_{amb} is the heat transfer coefficient for heat exchange with the environment, h_{FG} is the heat transfer coefficient of the flue gas, h_{HA} is the heat transfer coefficient of the hot air, and h_{CA} is the heat transfer coefficient of the cold air.

In the first relationship, eq. (5.9), the first term represents convective heat transfer between the flue gas in element i and the surface element $(1,i)$, the second term represents the heat transfer from the surface $(1,i)$ by conduction through insulation and then convection to the ambient air, and the term on the right hand side represents surface-to-surface radiation heat transfer from the surface $(1,i)$ to all the surface elements in surfaces 1 and 2L. For an element i in surfaces 2R, 3L and 3R, eqs. (5.10) to (5.13), there are convection interactions from the gas in contact with the surface and radiation interactions with all the surfaces that the surface "sees" as defined by the relevant view factors. The view factors $F_{i,j}$ are geometry dependent and are calculated based on the analytical expressions reported in the literature for different geometry types required in this case.

5.3 View factor calculation

The expressions for the surface-to-surface view factors required for the recuperator (see Figure 5.4) are presented in this section. The following radiation heat transfer cases are considered: between concave surfaces of a cylinder, surfaces of two coaxial cylinder, and concave surfaces of a cylinder in the presence of a smaller coaxial cylinder which are representative for radiation interactions between different surfaces (i, i') of the recuperator.

Exterior of right circular cylinder of finite length to interior of coaxial outer right circular cylinder (Figure 5.5)

Figure 5.5: Dimensions of relevant geometries for capturing view factors for the recuperator model. Schematic for the case: of right circular cylinder of finite length to interior of coaxial outer right circular cylinder.

Subscripts 1 and 2 represent the inner and outer cylinders respectively

(see Figure 5.5). Let r_i be the radius and A_i be the surface area for cylinder i $\forall i \in [1, 2]$. Let h be the height of the cylinder. Let $R_1 = r_1/h$, $R_2 = r_2/h$, $A = R_2 + R_1$, and $B = R_2 - R_1$. The view factor $F_{1,2}$ is given by the following equation [5, 16]:

$$
\begin{aligned}
F_{1,2} = {} & \frac{1}{\pi R_1} \left[\frac{1}{2} \left(R_2^2 - R_1^2 - 1 \right) \cos^{-1} \frac{R_1}{R_2} \right] \\
& + \frac{1}{\pi R_1} \left[\pi R_1 - \frac{\pi}{2} AB - 2R_1 \tan^{-1} \left(R_2^2 - R_1^2 \right)^{1/2} \right] \\
& + \frac{1}{\pi R_1} \left[\left\{ \left(1 + A^2 \right) \left(1 + B^2 \right) \right\}^{1/2} \tan^{-1} \left\{ \frac{\left(1 + A^2 \right) B}{\left(1 + B^2 \right) A} \right\}^{1/2} \right]
\end{aligned}
\tag{5.14}
$$

Exterior of inner coaxial cylinder to interior of larger outer cylinder; smaller cylinder completely outside the larger cylinder (Figure 5.6)

Subscripts 1 and 2 represent the inner (smaller) and outer (larger) cylinders respectively (see Figure 5.6). Let r_i be the radius and A_i be the surface area for cylinder i $\forall i \in [1, 2]$. Let l be the height of the inner cylinder, y be the height of the larger cylinder, and d be the distance of separation between the two cylinders. Let $D = d/r_2$, $Y = y/r_2$, $L = l/r_2$, and $R = r_1/r_2$. Also, A_ξ, B_ξ, and F_ξ are defined as:

$$
A_\xi = \xi^2 + R^2 - 1
\tag{5.15}
$$

$$
B_\xi = \xi^2 - R^2 + 1
\tag{5.16}
$$

87

Figure 5.6: Dimensions of relevant geometries for capturing view factors for the recuperator model. Schematic for the case: exterior of inner coaxial cylinder to interior of larger cylinder; smaller cylinder completely outside the larger cylinder.

$$
F_\xi = \frac{B_\xi}{8R\xi} + \frac{1}{2\pi}\left\{\cos^{-1}\frac{A_\xi}{B_\xi} - \frac{1}{2\xi}\left[\frac{(A_\xi+2)^2}{R^2} - 4\right]^{1/2}\cos^{-1}\frac{A_\xi R}{B_\xi} - \frac{A_\xi}{2\xi R}\sin^{-1}R\right\}
$$
$$(5.17)$$

The governing equation for the view factor $F_{1,2}$ is given by [100]:

$$
F_{1,2} = \frac{L+D}{L}F_{L+D} + \frac{Y+D}{L}F_{Y+D} - \frac{D}{L}F_D - \frac{L+D+Y}{L}F_{L+D+Y} \quad (5.18)
$$

Figure 5.7: Dimensions of relevant geometries for capturing view factors for the recuperator model. Schematic for the case: interior of finite length right circular coaxial cylinder to itself.

Interior of finite length right circular coaxial cylinder to itself (Figure 5.7)

The self view factor of the outer cylinder in the presence of inner concentric coaxial cylinder (see Figure 5.7) $F_{1,1}$ is given by [5, 16]:

$$
\begin{aligned}
F_{1,1} =\ & \frac{1}{\pi R_2} \left\{ \pi \left(R_2 - R_1 \right) + \cos^{-1} \frac{R_1}{R_2} \right\} \\
& - \frac{1}{\pi R_2} \left\{ \left(1 + 4R_2^2 \right)^{1/2} \tan^{-1} \frac{\left[\left(1 + 4R_2^2 \right) \left(R_2^2 - R_1^2 \right) \right]^{1/2}}{R_1} \right\} \\
& + \frac{1}{\pi R_2} \left\{ 2R_1 \tan^{-1} \left[2 \left(R_2^2 - R_1^2 \right)^{1/2} \right] \right\}
\end{aligned}
\tag{5.19}
$$

Interior surface of right circular coaxial cylinder to the adjacent interior surface (Figure 5.8)

Figure 5.8: Dimensions of relevant geometries for capturing view factors for the recuperator model. Schematic for the cases: (1) Interior surface of right circular coaxial cylinder to the adjacent interior surface and (2) interior surface of right circular coaxial cylinder to an interior surface separated by a distance.

Let subscript 1 represent the interior surface of right circular coaxial cylinder, subscript 2 represent the adjacent surface, and subscript T represent the combined surface, i.e., 1 and 2 stacked together (see Figure 5.8 where $d = 0$). Let L_i be the length of surface i $\forall\, i \in [1, 2]$ and L_T be the total length of both the surfaces combined $L_T = L_1 + L_2$. The view factor between the adjacent surfaces of the shell $F_{1,2}$ is given by the following equation [130]:

$$F_{1,2} = \frac{L_T F_{T,T} - L_1 F_{1,1} - L_2 F_{2,2}}{2L_1} \qquad (5.20)$$

where $F_{1,1}$, $F_{2,2}$, and $F_{T,T}$ are the self view factors of the interior shell surfaces 1, 2, and T respectively.

Interior surface of right circular coaxial cylinder to an interior surface separated by a distance (Figure 5.8)

Let subscript 1 represent the interior surface of right circular coaxial cylinder and subscript 2 represent the surface separated from surface 1 by a distance d (see Figure 5.8). Let L_1 be the combined length of surfaces 1 and d and L_2 be the combined length of surfaces 2 and d. The view factor $F_{1,2}$ is given by [130]:

$$F_{1,2} = \frac{(L_1 + L_2 + d)F_{(L_1+L_2+d),(L_1+L_2+d)} - (L_1 + d)F_{(L_1+d),(L_1+d)}}{2L_1}$$
$$- \frac{(L_2 + d)F_{(L_2+d),(L_2+d)}}{2L_1} \qquad (5.21)$$

where $F_{(L_1+L_2+d),(L_1+L_2+d)}$, $F_{(L_1+d),(L_1+d)}$, and $F_{(L_2+d),(L_2+d)}$ are calculated from the view factor expression given in the 5.3 subsection.

Interior surface of right circular cylinder to itself (Figure 5.9)

Let 2 be the interior surface of right circular cylinder of radius r and length h (see Figure 5.9). Let $H = h/2r$. The self view factor $F_{2,2}$ is given by the following governing equation [17]:
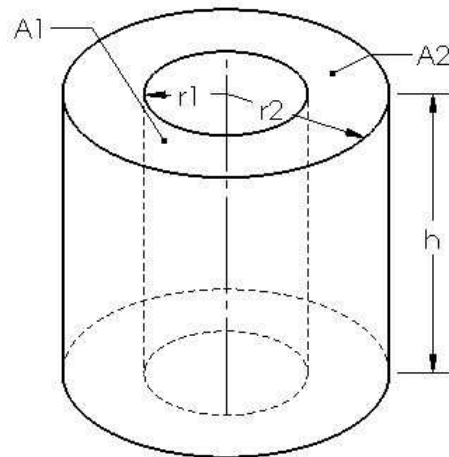
91
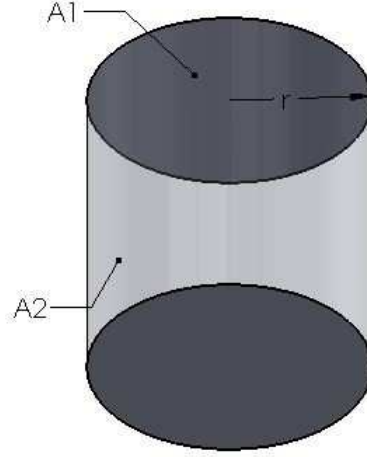
Figure 5.9: Dimensions of relevant geometries for capturing view factors for the recuperator model. Schematic for the case: interior surface of right circular cylinder to itself.

$$F_{2,2} = (1 + H) - \left(1 + H^2\right)^{1/2} \tag{5.22}$$

Interior surface of right circular cylinder to interior surface of adjacent right circular cylinder of the same diameter (Figure 5.10)

Let subscript 1 represent the interior surface of right circular cylinder of radius r and subscript 2 represent the surface of adjacent cylinder with radius r (see Figure 5.10). Let h_i be the length and A_i be the surface area for surface i $\forall\, i \in [1, 2]$. Let $H_1 = h_1/r$ and $H_2 = h_2/r$. The governing equation for the view factor $F_{1,2}$ is [73]:
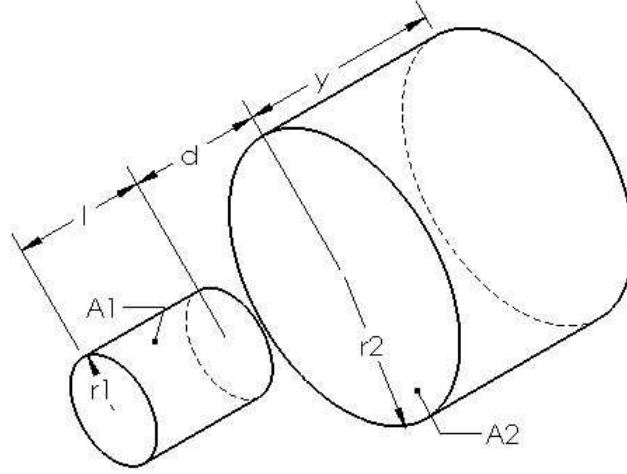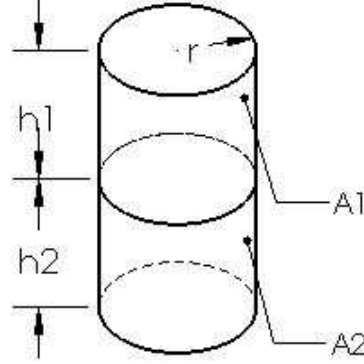
Figure 5.10: Dimensions of relevant geometries for capturing view factors for the recuperator model. Schematic for the case: interior surface of right circular cylinder to interior surface of adjacent right circular cylinder of the same diameter.

$$F_{1,2} = \frac{H_2}{2} + \frac{1}{4}\left\{\left(4 + H_1^2\right)^{1/2} + \left[\frac{H_2}{H_1}\left(4 + H_2^2\right)^{1/2}\right]\right\}$$
$$- \frac{1}{4}\left\{\left(1 + \frac{H_2}{H_1}\right)\left[4 + (H_1 + H_2)^2\right]^{1/2}\right\} \tag{5.23}$$

If $H_1 = H_2 = H$, then:

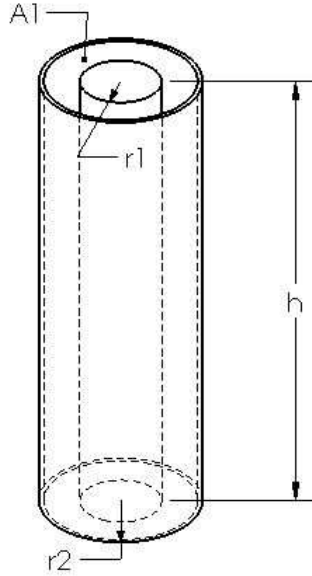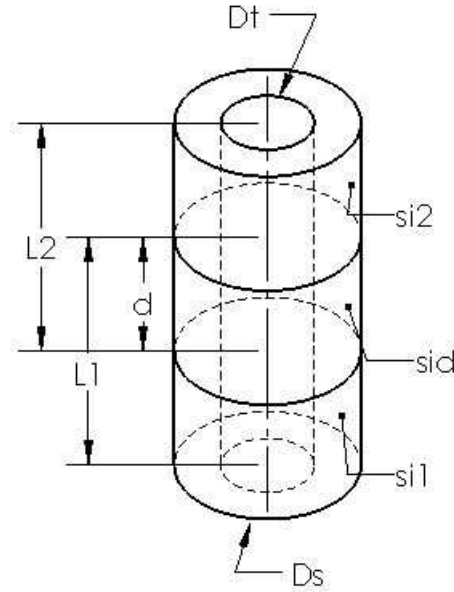$$F_{1,2} = \frac{1}{2}\left[H + \left(4 + H^2\right)^{1/2} - 2\left(1 + H^2\right)^{1/2}\right] \tag{5.24}$$
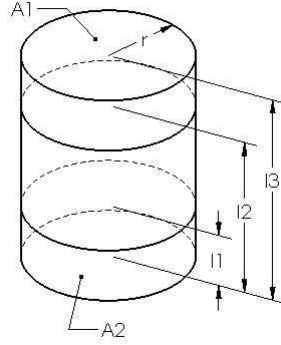
Figure 5.11: Dimensions of relevant geometries for capturing view factors for the recuperator model. Schematic for the case: finite section of right circular cylinder to separated finite section.

Finite section of right circular cylinder to separated finite section (Figure 5.11)

Let 1 be the interior surface of the finite section of right circular cylinder of radius r and let 2 be the separated finite section (see Figure 5.11). Let A_1 and A_2 be the surface areas of surfaces 1 and 2 respectively. Let l_1 be the length of section 2, l_2 be the length of section 2 plus the gap and l_3 be the combined length of sections 1, gap, and 2. Let $L = l/r$ and $X(L) = (L^2+4)^{1/2}$. The view factor $F_{1,2}$ is given by the following equation [17]:

$$
\begin{aligned}
F_{1,2} &= \frac{1}{4(L_3 - L_2)} \left[2L_1(L_3 - L_2) + (L_3 - L_1)X(L_3 - L_1) \right] \\
&- \frac{1}{4(L_3 - L_2)} \left[(L_2 - L_1)X(L_2 - L_1) - L_3X(L_3) + L_2X(L_2) \right]
\end{aligned}
\tag{5.25}
$$

Reciprocity theorem of view factors

Lastly, the reciprocity theorem allows us to calculate the view factor $F_{2,1}$ when $F_{1,2}$ is already known [55]:

$$A_1 F_{1,2} = A_2 F_{2,1} \qquad (5.26)$$

where A_1 and A_2 are the surface areas of surfaces 1 and 2 respectively.

5.4   Solution approach

An iterative algorithm is used to solve the energy conservation equations (5.1)-(5.13) to obtain the surface and gas temperature profiles. The view factors between all the surface pairs for the recuperator are precalculated since the geometry of the system is fixed.

The sequence of calculations in the solution algorithm is shown in the flow chart in Figure 5.12. The inlet flue gas and air temperatures are known. The temperature of the first element in the flue gas channel is assigned the value of the inlet flue gas temperature and the temperature of the last element in the cold air channel (due to the counter-current flow arrangement) is assigned the value of the inlet air temperature. The governing equations are uncoupled into non-radiation and radiation parts. The temperature profile of the recuperator is calculated by the following algorithm:

A1. Provide an initial guess for the surface temperatures.
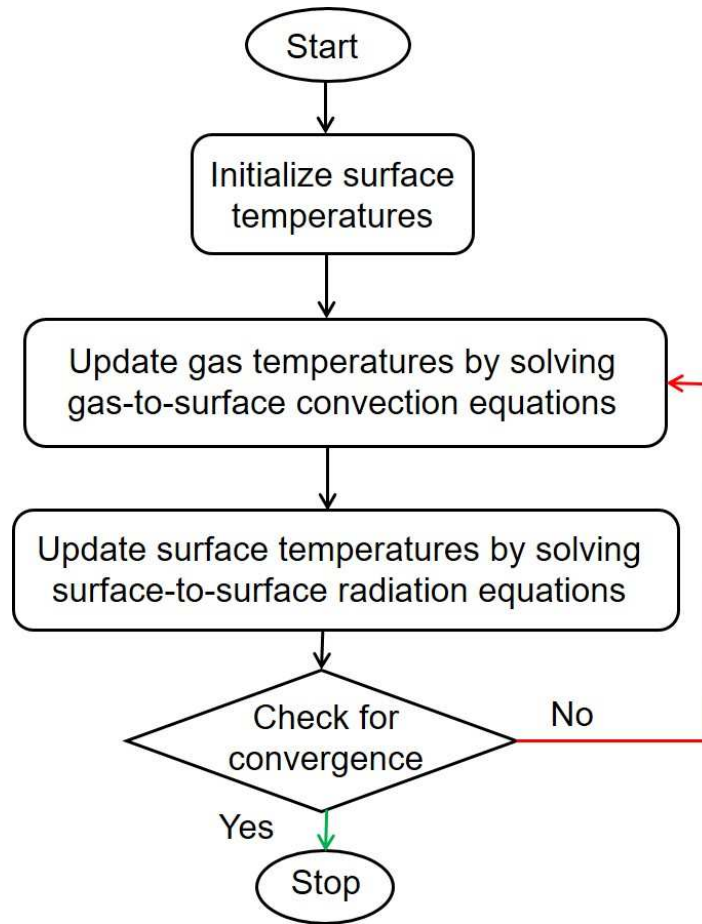
Figure 5.12: Iterative solution algorithm for determining the temperature profile of the radiant recuperator.

A2. Solve for the convection heat interactions between gases and surfaces, eqs. (5.1) to (5.3), to determine the temperature distribution of the gases in the recuperator.

A3. Solve the radiation heat transfer rate equations in the flue gas channel (eqs. (5.4) and (5.5)) to determine the radiosities for the elements in

surface 1 and 2L.

A4. Using the radiosites, calculate the updated surface temperatures for surfaces 1 and 2L using the radiation relations from the overall heat balance (eqs. (5.9) and (5.10)).

A5. Since surface 2 is isothermal, assign the temperature for surface 2R the value of the calculated temperature for surface 2L from the previous step.

A6. Calculate the radiosities and updated surface temperatures for surfaces 2R and 3L using eqs. (5.6), (5.7), (5.11) and (5.12).

A7. Since surface 3 is isothermal, assign the temperature for surface 3R the value of the calculated temperature for surface 3L from the previous step.

A8. Calculate the radiosities and updated surface temperatures for elements in surface 3R using eqs. (5.8) and (5.13).

A9. Repeat the above procedure from step 2 until the difference between the solutions of subsequent iterations converges to a predefined tolerance.

The temperature of the last element in the hot air channel is then the temperature of the inlet air to the burner in the furnace.

Since the view factors between surfaces vary significantly, the coefficient matrix of the linear system of equations for calculating radiosities which depend on these view factors can become ill-conditioned. The coefficient matrix

97

for J_i becomes ill conditioned when eqs. (5.9) to (5.13) are used to calculate radiosities instead of eqs. (5.4) to (5.8). In eqs. (5.4) to (5.8), on the other hand, the RHS terms also contain J_i which when rearranged to the LHS strengthen the diagonal terms of the coefficient matrix thus improving its condition number. Therefore, eqs. (5.4) to (5.8) are first solved to calculate the radiosities. Then, using the radiosities, eqs. (5.9) to (5.13) are solved to determine the updated surface temperatures.

In the furnace model (see Chapter 2), the parts are assumed to move in a discrete manner, with each part moving between predefined locations at each *furnace time step* (4 min). At every time step, the furnace model is solved to determine the part temperature distribution. The feedback controller, on the other hand, senses and manipulates the fuel flow rates to the burners after a different fixed time interval called the *controller time step*, which could be greater than or equal to the furnace time step. In this work, the controller time step equals the furnace time step. The mass flow rate of the burner flue gas could change whenever the feedback controller is active, i.e., after every controller time step. However, the temperature of the flue gas could change after every furnace time step because it depends on the dynamics of the furnace. Since both the mass flow rate and temperature of flue gas are inputs to the recuperator, the model equations are solved by the aforementioned iterative procedure at every furnace time step. Except the first and last few parts, the furnace operates in a constant part input-output regime. Under this condition, there are only minor changes in variables such as the flow rates

and temperatures of the burner exhaust gases. Therefore, the same initial guess for recuperator surface temperatures was provided for the calculations for all the burners at all time instants. It takes fewer than 10 iterations for the recuperator temperatures to converge from an appropriate initial solution.

5.5 Operation under heat integration

5.5.1 Recuperator simulation

First, we discuss the temperature profile of the recuperator at steady state for a constant flue gas flow rate. Our industrial partner provided the information that the air should not be heated beyond 533.15 K to limit NOx emissions. Based on the model equations (see eqs. (5.1) to (5.13)) and intuition, the maximum heating of air occurs at the minimum mass flow rate of the gases. It was verified that at the lower bound of the mass flow rate of flue gas (0.07 kg/s) this condition is met for the following model parameters, which are based on typical values for this system confirmed by the industry partner: $C_{p,FG} = 1.37$ kJ/kg-K, $C_{p,air} = 1$ kJ/kg-K, $h_{FG} = 150$ W/m^2-K, $h_{amb} = 100$ W/m^2-K, and $k_{ins} = 0.15$ W/m-K. For this condition, the predicted temperatures of the gases in the recuperator are plotted against the element index in Figure 5.13. It can be seen that the temperature of the hot air represented by the blue line at element index 6 (the exit of the recuperator) is close to but within the upper limit. The corresponding temperatures of the surface elements of the recuperator are shown in Figure 5.14. Since the upper limit of the hot gas temperature is 533.15 K for mass flow rate of 0.07 kg/s (burner

lower bound) and the temperature of the flue gas is above 1000 K, almost all of the heating occurs in the hot air channel due its proximity to the hot flue gas for this operating condition.
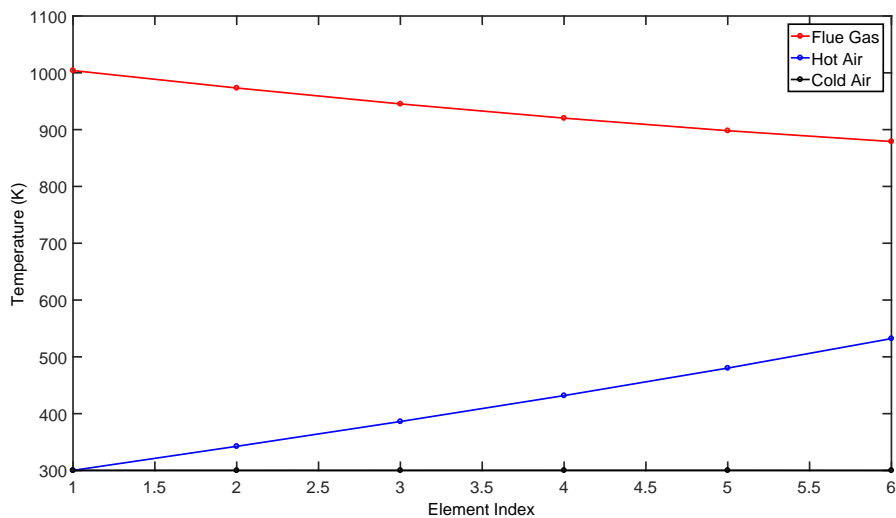
Figure 5.13: The temperature profiles of the flue gas, hot air, and cold air the recuperator under the minimum allowed fuel flow rates to the burner.

5.5.2 Furnace simulation

First, the model of the furnace embedded with a recuperator at each burner was simulated under the heuristic zone temperature set points suggested by the operators of the plant: [1000 K, 1150 K, 1200 K, and 1250 K] for zones 1 to 4 respectively. The furnace has a capacity of 8 parts and simulations were run for processing a batch of 40 parts sequentially. The part exit conditions of all the parts and the enthalpy change to the system are plotted
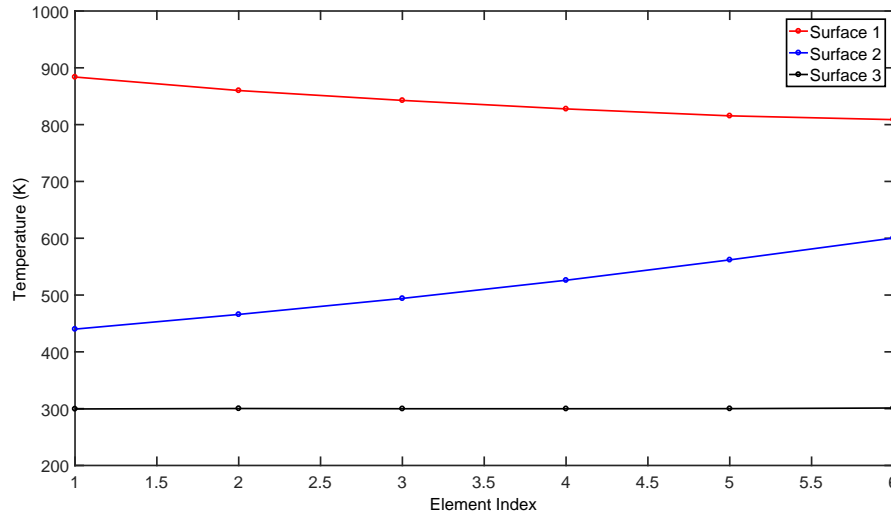
Figure 5.14: The temperatures of surfaces 1, 2, and 3 along the length of the recuperator.

in Figure 5.15. It can be seen that the minimum and average temperatures, represented by green and red lines respectively, attain a constant value within the first 6 parts. There are fewer parts and thus fewer heat sinks in the furnace during the pre- and post-steady state operation (constant input/output of parts). Hence, the temperatures and enthalpy of the first few parts and the last two parts show a slight deviation from the steady state values. The dotted lines represent the average plus and minus the standard deviations in the inhomogeneous part temperatures at the exit of the furnace.

The part temperature and grain size distribution of the "middle-of-the-batch" part (part number 20) as a function of time (thus position) are plotted in Figure 5.16. The part operates under the constant part input/output regime
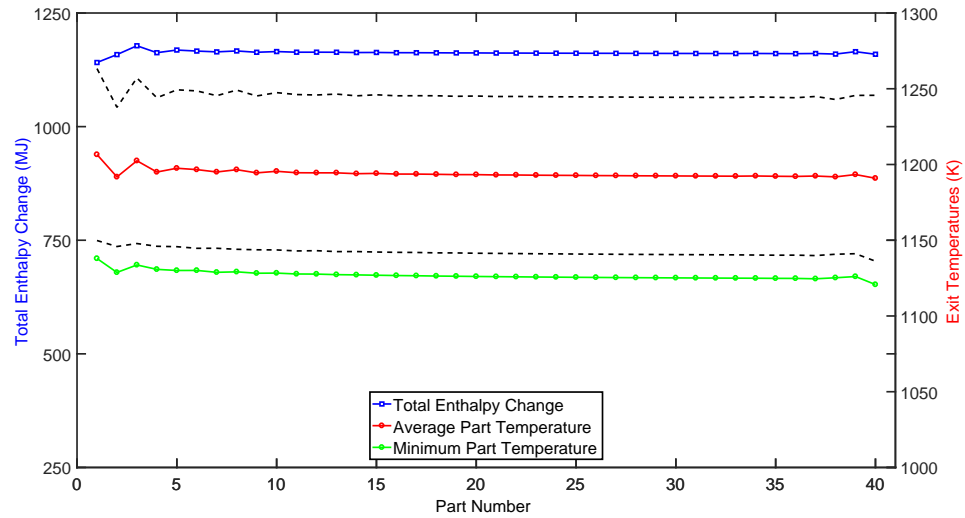
Figure 5.15: The exit conditions of all the 40 parts processed sequentially in the furnace equipped with the recuperators under the heuristic zone temperature set points.

of the furnace and thus represents the trend of the majority of the parts processed. The maximum part temperature occurs at the surface of the part, which is heated by radiation from burners and thus reaches its maximum value within 2 hours of processing. The minimum part temperature, on the other hand, is at the core of the part, which is heated only by conduction from the hot outer part surfaces and thus gradually increases to its maximum value at the exit of the furnace. Considering now the grain size distribution, it can be noted that the grain size of a region increases from zero when the temperature of the region exceeds the austenite transformation temperature as predicted by the model in the 2.3 subsection. The maximum grain size increases from zero at around 0.9 h (3240 s) when the maximum temperature is about the

102

transformation temperature of 1065 K. The maximum grain size then steadily increases to its exit value of 93.6 μm. The minimum grain size is in interior regions. The minimum grain size at the furnace exit is greater than zero indicating complete transformation of the part to austenite.
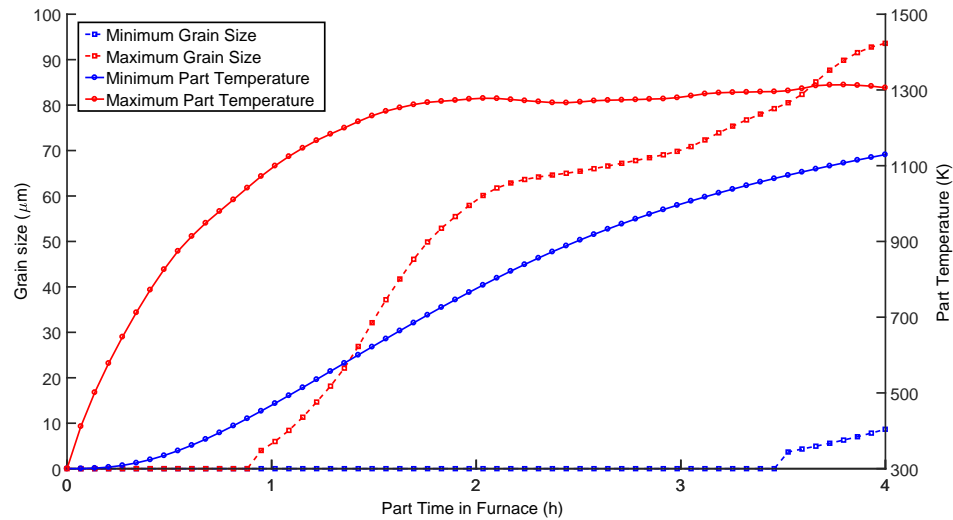
Figure 5.16: The exit part temperature and grain size distribution of the 20th (middle of the batch) part as a function of processing time in the furnace under the heuristic zone temperature set points.

The optimal zone temperature set points obtained from the procedure explained in Chapter 3 are: [1000 K, 1030 K, 1182 K, and 1212 K] for zones 1 to 4 respectively. Figure 5.17 shows the temperature and grain size distribution of part number 20 under optimized furnace operation case. As expected, the profiles are different from the heuristic case since they are dependent on the new zone temperature set points. The maximum grain size increases from zero at about 1.5 h (5400 s) compared to 0.9 h (3240 s) for the heuristic case as the

maximum part temperature crosses the austenite transformation temperature during that time. In this case too, the minimum grain size at furnace exit is greater than zero indicating complete austenite transformation of the part.
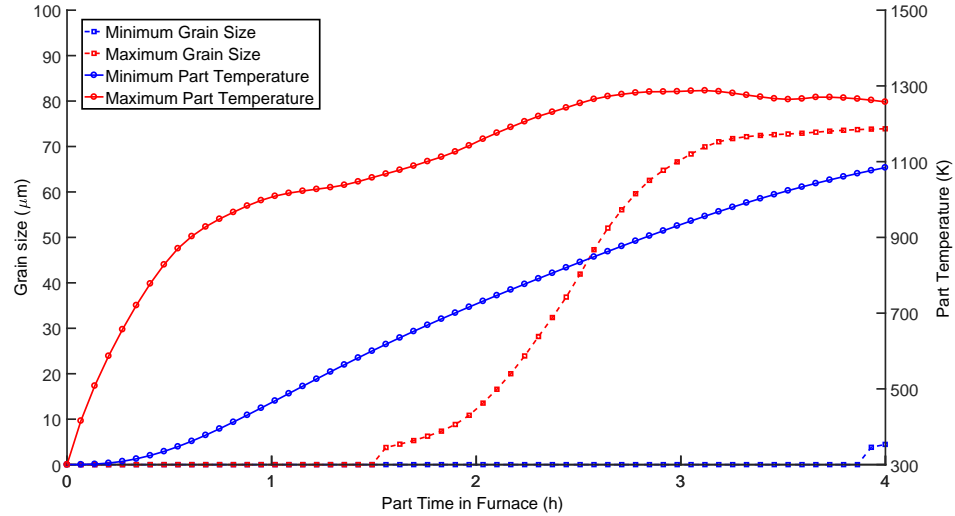
Figure 5.17: The exit part temperature and grain size distribution of the 20th (middle of the batch) part as a function of processing time in the furnace under the optimized zone temperature set points.

5.5.3 Energy efficiency comparison

Finally, the energy input to the system and part exit conditions of the above described operation scenarios ((1) operation of furnace embedded with recuperators under the heuristic zone temperature set points and (2) operation of furnace embedded with recuperators under the optimized zone temperature set points) are compared with the base case of furnace operation without recuperators under heursitic zone temperature set points in Table 5.2.

The furnace equipped with recuperators requires 15.93% less fuel compared to the base case, with minor changes in the part exit conditions since the zone temperature set points remain the same. The optimized operation of the furnace equipped with recuperators requires 20.88% less fuel input to the system compared to the base case. There is an additional 5.87% reduction in fuel input compared to the heuristic case embedded with recuperators. The value is close to the percentage reduction in energy use (3.5%) between the heuristic and optimized cases without recuperators. However, under this optimized operation mode, the part temperatures are lower than the heuristic cases and the energy gains are obtained by operating the furnace at constraints as is often the case in the process industries.

Furnace details	
Length of the furnace	16 m
Height of the furnace/length of the side walls	2 m
Length of each discretized furnace surface except the side walls	0.25 m
Total number of furnace surfaces	130
Length of a part	1.25 m
Ordinate of a part	0.75 m
Height of a part	0.5 m
Process conditions	
Number of parts processed	40
Part residence time	14400 s (4 h)
Simulation time step	240 s (4 min)
Inlet temperature of parts	300 K
Inlet temperature of blanket gas	400 K
Number of points in x-direction for Crank-Nicolson method	6
Number of points in y-direction for Crank-Nicolson method	6
Total time of furnace operation	90000 s (25 h)
Grain growth prediction	
k_1	4.1×10^7
k_2	0.12
Q_o	141 kJ/mol
$T_{austenite}$	1065 K
Number of portions in the x-direction for grain size prediction	3
Number of portions in the y-direction for grain size prediction	6
Recuperator	
r_1	0.07 m
r_2	0.04 m
r_3	0.02 m
Thickness of insulation	0.05 m
Length of the recuperator	0.6 m
Length of a discretized element	0.1 m
Set point optimization	
$T_{sp,lb}$	1000 K
$T_{sp,ub}$	1300 K
$T_{sp,diff}$	30 K
$T_{part,min,lb}$	1100 K
$COV_{part,ub}$	0.05
$d_{\gamma,ub}$	90 μm

Table 5.1: List of parameters for furnace simulation and set point optimization under heat integration using recuperators.

Heat Sources and Sinks	Heuristic (no recuperators)	Optimized (no recuperators)	Heuristic	Optimized
Total Fuel Input Per Part (kg)	9494	9162	7981	7512
Part Minimum Temperature (K)	1126	1088	1126	1082
Coefficient of Variation	0.043	0.044	0.043	0.045
Maximum Grain Size (μm)	93.60	73.80	93.60	73.93
Energy to Parts (%)	54.2%	53.5	54.3%	54.5%
Energy Lost with the Exhaust (%)	42.7%	43.4	42.6%	42.3%
Energy to Flowing Nitrogen (%)	0.5%	0.5	0.5%	0.6%
Energy Through Insulation (%)	2.6%	2.6	2.6%	2.6%

Table 5.2: Comparison of fuel input to the system and part exit conditions for the operation of furnace equipped with recuperators under heurstic and optimized set points with the base case of furnace operation without recuperators.

Chapter 6

Future work and conclusions

This chapter is based on material published in papers "H. S. Ganesh, T. F. Edgar, and M. Baldea. Modeling, optimization and control of an austenitization furnace for achieving target product toughness and minimizing energy use. Journal of Process Control, 2017. doi: 10.1016 j.jprocont.2017.09.008" [36], "H. S. Ganesh, T. F. Edgar, and M. Baldea. Model predictive control of the exit part temperature for an austenitization furnace. Processes, 4 (4):53, 2016" [32], and "H. S. Ganesh, O. A. Ezekoye, T. F. Edgar, and M. Baldea. Heat integration and operational optimization of an austenitization furnace using concentric-tube radiant recuperators. AIChE Journal, 2018; doi: 10.1002 /aic.16414" [39]. I am the primary contributor of the aforementioned papers.

6.1 Future work

6.1.1 Parameter estimation for procedural model

Validation of the model with real-time measurements would be the first step moving forward. Due to the proprietary nature of the data and difficulty in installment and calibration of appropriate sensors, we haven't got all the required information on real-time operation from our industrial partner. Never-

theless, we shared our results with them and they found our model predictions to be reasonable based on their experience. Improving the numerical accuracy of model predictions would require us to estimate the parameters of the model from the real-time measurement data. The multiscale model developed in this work is procedural and hence estimating its parameters is challenging. The solution to the problem is to search through the parameter space to find a point (a set of parameter values) whose corresponding model predictions agree well with experimental observations. The solution found by a direct search method such as the random mutation hill-climbing algorithm [114] is not guaranteed to be a global solution and is slow. To overcome these two problems, Qin and Yang [97] used a genetic-based search method [97], that searches in multiple directions, for estimating the parameters for procedural texturing. The genetic-based search algorithm first initializes randomly a population of search points P_1, P_2, ... P_m. For each P_i, the algorithm generates a temporary output and the calculates the squared errors between the key variables of the temporary output and the target output. If these errors are within a user-specified tolerance limit, the algorithm outputs the matched point P_i as the final estimated parameter values. Else, the algorithm generates the next population of search points using selection, crossover and mutation operations based on previous population of search points and the procedure is repeated until the stopping condition is satisfied.

6.1.2 Data reconciliation and validation

The measured data are never 100% correct due to measurement uncertainties and inaccuracies. Data reconciliation (DR) is a procedure of optimally adjusting measured data such that the estimates satisfy a certain set of conservation laws and process constraints. Several studies of DR are reported in the literature [62, 72, 94]. Some authors suggest that both process states and parameters be estimated simultaneously [4, 77, 88]. Prata *et al.* [95] used particle swarm optimization technique to solve nonlinear dynamic reconciliation problems with simultaneous parameter estimation. We recommend to apply the furnace model developed in this research for DR of the actual heat treating furnace in operation. Also, based on the measurements, the model parameters can also be identified simultaneously when the operating conditions change or there is a disturbance in the process.

6.1.3 Surrogate model improvement

In this work, we observe an offset between the physics-based furnace model and surrogate model predicted outputs. One of the reasons could be the inclusion of the entire input space in the surrogate model development. It would be worth exploring the development of local sub-surrogate models in regions where optimal solutions are likely to be found. Another reason could be the chosen model-form of the surrogate models, which was assumed to be fixed for all output variables. The surrogate model form was selected based on the physics of the system, such as the fourth power dependence of temperature.

110

However, it would be worth investigating the influence of different surrogate model equations and different equations for different output variables based on both the physical relationship between the respective output and input variable and the significance of the model parameters.

6.1.4 Physics-based modeling of microstructure changes

In this work, we used an empirical relation presented in Anelli [7] to calculate the austenite grain size as a function of temperature and history of heating. In the literature, detailed finite element models have been developed to study the metallo-thermo-mechanical behaviors during heat treatment of a part [7, 71, 75, 104]. It would be interesting to study the effects of detailed modeling at the microstructural level on the predictions of the metallurgical properties of the quenched product. Since the model is intended for on-line optimization and control, it is important to look at the computational costs involved in adding details versus the improvement in accuracy of the predictions.

6.1.5 Three-dimensional radiation-based furnace model

The effect of the third dimension (3D) on the system dynamics, optimization and control would be an interesting direction for exploration. Although a 3D model would be computationally more expensive for on-line optimization purposes, it can be used for system redesign and heat integration studies. The 3D model accurately mimics the geometry of the actual sys-

tem and hence we believe that the predictions would also agree much better with the plant observations. Even though the detailed model would not be suitable for on-line optimization, surrogate models can be developed using the detailed model for fast simulation and optimization purposes. It would be worth making a comparison between the results of the surrogate model from the 2D furnace model and that from a 3D furnace model. The surrogate model development using 3D furnace model would be computationally expensive. However, that is only one time computation. Once the surrogate models are developed, they would be of the same size as that developed from a 2D model. In this way, the accuracy of the on-line predictions can be improved without much increase in real-time computational costs.

6.1.6   Heat exchange network optimization

In this thesis, the recuperator (heat exchanger) exchanges heat between the exhaust of a burner and the inlet air to the same burner. It would interesting to explore the impact of exchanging heat with a different burner on energy savings, thereby determining the optimal heat exchange network. Also, it would be worth investigating the heat exchange using various commercially available heat exchangers, suitable for operation under the temperature conditions of the furnace.

6.2 Conclusions

In this work, a previously developed 2D physics-based model of an industrial austenitization furnace, operating under feedback control is improved and extended with an empirical model for predicting austenite grain sizes. The combined model evaluates the energy consumption of the system, part temperature distribution, and microstructural evolution of parts (a key quantity for controlling metallurgical properties) as a function of operating conditions and time of processing. Our objective is to minimize the energy input to the system such that the parts are uniformly heated to the required amount and the the grain sizes of the parts at furnace exit are within an upper limit to ensure toughness of the quenched product. Our findings are interesting from the point of view of energy efficient control, in the sense that accounting for microscopic properties (namely, austenite grain size) that are crucial for product quality results in a completely different control settings. This is reflected in different zone temperature set points, and controlling for microscopic properties results in lower energy use (by 3.5%) for the same quality product and a higher energy use (by 12.57%) for a higher quality product than in the case where only the macroscopic part temperature distribution at the exit of the furnace is controlled. We hope that these findings will encourage further research into incorporating the microscopic realm (e.g., properties of materials) in system models and control algorithms, particularly through time dependent constitutive relations of the type considered in this work.

Model predictive control is then implemented as a supervisory control

113

to limit the part temperature at exit by varying the zone temperature set points of the inner level temperature tracking controller. We first develop a step-response model to predict the future evolution of the output variables. The coefficients of the step-response model are then used to solve a quadratic program subject to input and output constraints to determine the optimal control move at each control time step. The time interval of the model predictive control is longer than that of the regulatory control. A comparison, in terms of energy consumption, is made between the furnace operation under the two-level hierarchical control and under constant heuristic temperature set points reported in Heng *et al.* [48]. We obtain an energy efficiency gain of 5.3% under model predictive control by preventing the parts from overheating. Lastly, when there is a process disturbance in the form of an increased part thermal conductivity, the operation under model predictive control is more energy efficient than that at the constant temperature set points determined by the real-time optimization scheme due to the prevention of excess heating of the parts.

Furnace simulations and observations in the plant show that more than 40% of energy input to the austenitization furnace considered in this work is wastefully discharged in exhaust gases. Hence, an attempt was made to minimize this loss by recovering part of the heat in the burner exhaust gases to preheat the air fed to the burners using a recuperator. A shell and tube-type commercially available recuperator is modeled as a central pipe and two concentric annular ducts. A radiation-based model of the recuperator capturing

114

local convection and long-range radiation interactions was developed. The model was embedded into the furnace model. The furnace operation was optimized using surrogate models. The results showed 15.93% fuel savings for the furnace equipped with recuperators under the heuristic case with minor changes in the part exit conditions compared to the base case without recuperators. Additional energy savings of 5.87% were obtained when the furnace operation (specifically, the set points of the local temperature controllers) was optimized.

Dissemination of research

6.3   Journal publications

1. Ganesh, Hari S., Ofodike A. Ezekoye, Thomas F. Edgar, and Michael Baldea. "Heat integration and operational optimization of an austenitization furnace using concentric-tube radiant recuperators." *AIChE Journal*(2018) doi:10.1002/aic.16414 [39].

2. Korambath, Prakashan, Hari S. Ganesh, Jianwu Wang, Michael Baldea, and Jim Davis. "Use of on-demand cloud services to model the optimization of an austenitization furnace." *ASTM Smart and Sustainable Manufacturing Systems*(2018) doi:10.1520/SSMS20180024 [67].

3. Ganesh, Hari S., Thomas F. Edgar, and Michael Baldea. "Modeling, optimization and control of an austenitization furnace for achieving target product toughness and minimizing energy use." *Journal of Process Control*(2017) doi:10.1016/j.jprocont.2017.09.008 [36].

4. Heng, Vincent R., Hari S. Ganesh, Austin R. Dulaney, Andrew Kurzawski, Michael Baldea, Ofodike A. Ezekoye, and Thomas F. Edgar. "Energy-oriented modeling and optimization of a heat treating furnace." *Journal of Dynamic Systems Measurement and Control* 139.6 (2017): 061014 [48].

5. Ganesh, Hari S., Thomas F. Edgar, and Michael Baldea. "Model predictive control of the exit part temperature for an austenitization furnace." *Processes* 4.4 (2016): 53 [32].

6.4 Conference publications

1. Ganesh, Hari S., Ofodike A. Ezekoye, Thomas F. Edgar, and Michael Baldea. "Improving energy efficiency of an austenitization furnace by heat integration and real-time optimization." *Automation, Quality and Testing, Robotics (ATQR), 2018 IEEE International Conference on*, IEEE, 2018, doi:10.1109/AQTR.2018.8402763 [40].

2. Ganesh, Hari S., Eric M. Taleff, Thomas F. Edgar, and Michael Baldea. "Simultaneous optimization of material properties and energy efficiency of a steel quench hardening process." *American Control Conference (ACC), 2017*, pp. 2219-2224. IEEE, 2017, doi:10.23919/ACC.2017.7963282 [38].

6.5 Technical reports

1. Edgar, Thomas F., Michael Baldea, Ofodike Ezekoye, Hari Ganesh, Ankur Kumar, Dan Wanager, Vincent M. Torres, Jim Davis, Panagiotis Christofides, Prakashan Korambath, Vasilios Manousiouthakis, Robert Graybill, Brian Schott, Larry Megan, Jesus Flores-Cerillo, Gangshi Hu, Tushar Vispute, Joseph Chup, Todd Albertson, Darlene Schuster, Phil Callahan, and Denise Swink. "Industrial scale demonstration of smart

manufacturing, achieving transformational energy productivity gains."
DOE-UT Austin-0005763, United States, doi:10.2172/1454266 [28].

6.6   Conference proceedings

1. Ganesh, Hari S., Thomas F. Edgar, and Michael Baldea. "Implications of heat integration in energy savings during heat treating of steel." *2017 AIChE Annual Meeting*, Minnesota, MN, United States [35].

2. Ganesh, Hari S., Thomas F. Edgar, and Michael Baldea. "Multiscale modeling and model predictive control of an austenitization furnace." *Texas-Wisconsin-California Control Consortium*, Feb 2017, Austin, TX, United States [37].

3. Ganesh, Hari S., Thomas F. Edgar, and Michael Baldea. "Model predictive control and materials property estimation of an industrial heat treating furnace." *2016 AIChE Annual Meeting*, San Francisco, CA, United States [34].

4. Ganesh, Hari S., Thomas F. Edgar, and Michael Baldea. "Modeling and model predictive control of an austenitization furnace." *Texas-Wisconsin-California Control Consortium*, Feb 2016, Austin, TX, United States [33].

Bibliography

[1] R. Abbaschian and R. Reed-Hill. *Physical metallurgy principles*. Cengage Learning, 2008.

[2] H. Akaike. Factor analysis and aic. *Psychometrika*, 52(3):317–332, 1987.

[3] H. Akanuma. The significance of the composition of excavated iron fragments taken from stratum iii at the site of kaman-kalehöyük, turkey. *Anatolian Archaeological Studies*, 14:147–158, 2005.

[4] J. S. Albuquerque and L. T. Biegler. Data reconciliation and gross-error detection for dynamic systems. *AIChE journal*, 42(10):2841–2856, 1996.

[5] V. Alexandrov. Determination of the angular radiation coefficients for a system of two coaxial cylindrical bodies. *Inzh. Fiz. Zh*, 8(5):609–612, 1965.

[6] R. C. Allen. International competition in iron and steel, 1850–1913. *The Journal of Economic History*, 39(04):911–937, 1979.

[7] E. Anelli. Application of mathematical modelling to hot rolling and controlled cooling of wire rods and bars. *ISIJ international*, 32(3):440–449, 1992.

[8] W. S. Association et al. Sustainable steel: At the core of a green economy. *Rue Colonel Bourg*, 120, 2012.

[9] T. Badgwell, T. Breedijk, S. Bushman, S. Butler, S. Chatterjee, T. Edgar, A. Toprac, and I. Trachtenberg. Modeling and control of microelectronics materials processing. *Computers & chemical engineering*, 19(1):1–41, 1995.

[10] E. Bain and M. Grossmann. Principles of heat treatment. *ASM, Materials Park, OH*, page 129, 1964.

[11] L. Balbis, J. Balderud, and M. Grimble. Nonlinear predictive control of steel slab reheating furnace. In *American Control Conference, 2008*, pages 1679–1684. IEEE, 2008.

[12] K. C. Barraclough. *Steelmaking, 1850-1900*, volume 458. Woodhead Pub Ltd, 1990.

[13] T. Beausmeister et al. Marks standard handbook for mechanical engineers, 1978.

[14] H. Bessemer. *Sir Henry Bessemer, FRS: An Autobiography, with a Concluding Chapter*, volume 451. Maney Pub, 1905.

[15] L. Biegler, D. Alkaya, and K. J. Anselmo. Multi-solver modeling for process simulation and optimization. In *AIChE Symposium Series*, pages 125–137. New York; American Institute of Chemical Engineers; 1998, 2000.

[16] H. Brockmann. Analytic angle factors for the radiant interchange among the surface elements of two concentric cylinders. *International journal of heat and mass transfer*, 37(7):1095–1100, 1994.

[17] A. J. Buschman Jr and C. M. Pittman. Configuration factors for exchange of radiant energy between axisymmetrical sections of cylinders, cones, and hemispheres and their bases. 1961.

[18] W. D. Callister and D. G. Rethwisch. *Materials science and engineering: an introduction*, volume 7. Wiley New York, 2007.

[19] E. F. Camacho and C. B. Alba. *Model predictive control*. Springer Science & Business Media, 2013.

[20] J. M. Carrasco, L. G. Franquelo, J. T. Bialasiewicz, E. Galván, R. C. P. Guisado, M. Á. M. Prats, J. I. León, and N. Moreno-Alfonso. Power-electronic systems for the grid integration of renewable energy sources: A survey. *Industrial Electronics, IEEE Transactions on*, 53(4):1002–1016, 2006.

[21] S. C. Chapra and R. P. Canale. *Numerical methods for engineers*, volume 2. McGraw-Hill, 2012.

[22] W. Chen, Y. Chung, and J. Liu. Analysis on energy consumption and performance of reheating furnaces in a hot strip mill. *International Communications in Heat and Mass Transfer*, 32(5):695–706, 2005.

[23] A. Cozad, N. V. Sahinidis, and D. C. Miller. Learning surrogate models for simulation-based optimization. *AIChE Journal*, 60(6):2211–2227, 2014.

[24] C. R. Cutler and B. L. Ramaker. Dynamic matrix control?? a computer control algorithm. In *joint automatic control conference*, number 17, page 72, 1980.

[25] D. Demailly and P. Quirion. European emission trading scheme and competitiveness: A case study on the iron and steel industry. *Energy Economics*, 30(4):2009–2027, 2008.

[26] G. Derrick. A three-dimensional analogue of the hottel string construction for radiation transfer. *Journal of Modern Optics*, 32(1):39–60, 1985.

[27] T. F. Edgar and E. N. Pistikopoulos. Smart manufacturing and energy systems. *Computers & Chemical Engineering*, 2017. doi: 10.1016/j.compchemeng.2017.10.027.

[28] T. F. Edgar, M. Baldea, O. Ezekoye, H. Ganesh, A. Kumar, D. Wanegar, V. M. Torres, J. Davis, P. Christofides, P. Korambath, V. Manousiouthakis, R. Graybill, B. Schott, L. Megan, J. Flores-Cerillo, G. Hu, T. Vispute, J. Chup, T. Albertson, S. Cannizzaro, D. Schuster, P. Callahan, and D. Swink. Industrial scale demonstration of smart manufacturing, achieving transformational energy productivity gains. *DOE-UT Austin-0005763*. doi: 10.2172/1454266.

[29] T. F. Edgar, S. W. Butler, W. J. Campbell, C. Pfeiffer, C. Bode, S. B. Hwang, K. Balakrishnan, and J. Hahn. Automatic control in microelectronics manufacturing: Practices, challenges, and possibilities. *Automatica*, 36(11):1567–1603, 2000.

[30] A. B. Ellis et al. *Teaching General Chemistry: A Materials Science Companion.* ERIC, 1993.

[31] A. A. Fawcett, G. C. Iyer, L. E. Clarke, J. A. Edmonds, N. E. Hultman, H. C. McJeon, J. Rogelj, R. Schuler, J. Alsalam, G. R. Asrar, et al. Can paris pledges avert severe climate change? *Science*, 350(6265): 1168–1169, 2015.

[32] H. S. Ganesh, T. F. Edgar, and M. Baldea. Model predictive control of the exit part temperature for an austenitization furnace. *Processes*, 4 (4):53, 2016.

[33] H. S. Ganesh, T. F. Edgar, and M. Baldea. Modeling and model predictive control of an austenitization furnace. In *Texas-Wisconsin-California Control Consortium, Feb 2016, Austin, TX, United States.* TWCCC, 2016.

[34] H. S. Ganesh, T. F. Edgar, and M. Baldea. Model predictive control and materials property estimation of an industrial heat treating furnace. In *2016 AIChE Annual Meeting, Minnesota, MN, United States.* AIChE, 2016.

[35] H. S. Ganesh, T. F. Edgar, and M. Baldea. Implications of heat integration in energy savings during heat treating of steel. In *2017 AIChE Annual Meeting, Minnesota, MN, United States.* AIChE, 2017.

[36] H. S. Ganesh, T. F. Edgar, and M. Baldea. Modeling, optimization and control of an austenitization furnace for achieving target product toughness and minimizing energy use. *Journal of Process Control*, 2017. doi: 10.1016/j.jprocont.2017.09.008.

[37] H. S. Ganesh, T. F. Edgar, and M. Baldea. Multiscale modeling and model predictive control of an austenitization furnace. In *Texas-Wisconsin-California Control Consortium, Feb 2017, Austin, TX, United States.* TWCCC, 2017.

[38] H. S. Ganesh, E. M. Taleff, T. F. Edgar, and M. Baldea. Simultaneous optimization of material properties and energy efficiency of a steel quench hardening process. In *American Control Conference (ACC), 2017*, pages 2219–2224. IEEE, 2017. doi: 10.23919/ACC.2017.7963282.

[39] H. S. Ganesh, O. A. Ezekoye, T. F. Edgar, and M. Baldea. Heat integration and operational optimization of an austenitization furnace using concentric-tube radiant recuperators. *AIChE Journal*, 2018. doi: 10.1002/aic.16414.

[40] H. S. Ganesh, O. A. Ezekoye, T. F. Edgar, and M. Baldea. Improving energy efficiency of an austenitization furnace by heat integration

and real-time optimization. In *2018 IEEE International Conference on Automation, Quality and Testing, Robotics (AQTR)*. IEEE, 2018. doi: 10.1109/AQTR.2018.8402763.

[41] C. E. Garcia, D. M. Prett, and M. Morari. Model predictive control: theory and practicea survey. *Automatica*, 25(3):335–348, 1989.

[42] R. J. Goldstick and A. Thumann. Principles of waste heat recovery. 1985.

[43] S. P. Gupta. *Solid state phase transformations*. Allied Publishers, Mumbai, India, 2002.

[44] S. Han, D. Chang, and C. Huh. Efficiency analysis of radiative slab heating in a walking-beam-type reheating furnace. *Energy*, 36(2):1265–1272, 2011.

[45] A. Hasanbeigi, W. Morrow, J. Sathaye, E. Masanet, and T. Xu. A bottom-up model to estimate the energy efficiency improvement and co 2 emission reduction potentials in the chinese iron and steel industry. *Energy*, 50:315–325, 2013.

[46] C. Henao and C. Maravelias. Surrogate-based superstructure optimization framework. *AIChE Journal*, 57(5):1216–1232, 2011.

[47] V. R. Heng. Energy focused modeling and optimization of a radiant tube roller hearth austenization furnace. Master's thesis, The University of Texas at Austin, 2015.

[48] V. R. Heng, H. S. Ganesh, A. R. Dulaney, A. Kurzawski, M. Baldea, O. A. Ezekoye, and T. F. Edgar. Energy-oriented modeling and optimization of a heat treating furnace. *Journal of Dynamic Systems, Measurement, and Control*, 139(6):061014–1–061014–13, 2017.

[49] M. I. Hoffert, K. Caldeira, G. Benford, D. R. Criswell, C. Green, H. Herzog, A. K. Jain, H. S. Kheshgi, K. S. Lackner, J. S. Lewis, et al. Advanced technology paths to global climate stability: energy for a greenhouse planet. *science*, 298(5595):981–987, 2002.

[50] A. Holcroft. Conveyor Furnaces: Continuous Conveyor Thermal Treatment System. `http://www.afc-holcroft.com/userfiles/file/pdf/ConveyorFurnace_Brochure.pdf`, 2014. Accessed: 2015-04-09.

[51] J. Hollomon and L. Jaffe. Time-temperature relations in tempering steel. *Trans. AIME*, 162:223–249, 1945.

[52] J. Howell. The monte carlo method in radiative heat transfer. *Journal of Heat Transfer*, 120(3):547–560, 1998.

[53] A. Hu. *The Nature and Behavior of Grain Boundaries: A Symposium Held at the TMS-AIME Fall Meeting in Detroit, Michigan, October 18–19, 1971*. Springer Science & Business Media, 2012.

[54] Z. A. Icev, J. Zhao, M. J. Stankovski, T. Kolemishevska-Gugulovska, and G. M. Dimirovski. Supervisory-plus-regulatory control design for

126

efficient operation of industrial furnaces. *Journal of Electrical & Electronics Engineering*, 4(2):1199–1218, 2004.

[55] F. Incropera. *Fundamentals of heat and mass transfer*. John Wiley & Sons, Hoboken, NJ, 2011.

[56] H. Jacobs. Metallic recuperator and method of operating same, Mar. 19 1974. US Patent 3,797,558.

[57] A. Jaklič, F. Vode, and T. Kolenko. Online simulation model of the slab-reheating process in a pusher-type furnace. *Applied Thermal Engineering*, 27(5):1105–1114, 2007.

[58] D. R. Jones and M. F. Ashby. *Engineering materials 2: an introduction to microstructures, processing and design*. Butterworth-Heinemann, 2005.

[59] S. Kakac, H. Liu, and A. Pramuanjaroenkij. *Heat exchangers: selection, rating, and thermal design*. CRC press, 2012.

[60] D. Kang, Y. Kim, Y. Kim, W. Kim, and K. Kim. Experimental and numerical studies on the thermal analysis of the plate in indirectly-fired continuous heat treatment furnace. *VDI BERICHTE*, 1988:533, 2007.

[61] J. Kang and Y. Rong. Modeling and simulation of load heating in heat treatment furnaces. *Journal of materials processing technology*, 174(1): 109–114, 2006.

[62] I.-W. Kim, M. S. Kang, S. Park, and T. F. Edgar. Robust data reconciliation and gross error detection: the modified mimt using nlp. *Computers & chemical engineering*, 21(7):775–782, 1997.

[63] J. Kim, K. Huh, and I. Kim. Three-dimensional analysis of the walking-beam-type slab reheating furnace in hot strip mills. *Numerical Heat Transfer: Part A: Applications*, 38(6):589–609, 2000.

[64] Y. Kim, K. Moon, B. Kang, C. Han, and K. Chang. Application of neural network to the supervisory control of a reheating furnace in the steel industry. *Control Engineering Practice*, 6(8):1009–1014, 1998.

[65] E. Kintisch. After paris: The rocky road ahead. *Science*, 350(6264): 1018–1019, 2015.

[66] H. S. Ko, J.-S. Kim, T.-W. Yoon, M. Lim, D. R. Yang, and I. S. Jun. Modeling and predictive control of a reheating furnace. In *American Control Conference, 2000. Proceedings of the 2000*, volume 4, pages 2725–2729. IEEE, 2000.

[67] P. Korambath, H. S. Ganesh, J. Wang, M. Baldea, and J. Davis. Use of on-demand cloud services to model the optimization of an austenitization furnace. *Smart and Sustainable Manufacturing Systems*, 2018. doi: 10. 1520/SSMS20180024.

[68] G. Krauss. Principles of heat treatment of steel. *American Society for Metals, 1980,*, page 291, 1980.

[69] S. E. Kruger and E. B. Damm. Monitoring austenite decomposition by ultrasonic velocity. *Materials Science and Engineering: A*, 425(1): 238–243, 2006.

[70] P. Laurinen and J. Röning. An adaptive neural network model for predicting the post roughing mill temperature of steel slabs in the reheating furnace. *Journal of materials processing technology*, 168(3):423–430, 2005.

[71] S.-J. Lee and Y.-K. Lee. Prediction of austenite grain growth during austenitization of low alloy steels. *Materials & Design*, 29(9):1840–1844, 2008.

[72] M. Leibman, T. Edgar, and L. Lasdon. Efficient data reconciliation and estimation for dynamic processes using nonlinear programming techniques. *Computers & chemical engineering*, 16(10):963–986, 1992.

[73] H. Leuenberger and R. Person. Compilation of radiation shape factors for cylindrical assemblies. Technical report, ELECTRO METALLURGICAL CO NIAGARA FALLS NY, 1954.

[74] Y. Liao, M. Wu, and J. She. Modeling of reheating-furnace dynamics using neural network based on improved sequential-learning algorithm. In *Computer Aided Control System Design, 2006 IEEE International Conference on Control Applications, 2006 IEEE International Symposium on Intelligent Control, 2006 IEEE*, pages 3175–3181. IEEE, 2006.

[75] C. Liu, X. Xu, and Z. Liu. A fem modeling of quenching and tempering and its application in industrial engineering. *Finite elements in analysis and design*, 39(11):1053–1070, 2003.

[76] R. Lloyd-Jones and M. Lewis. *British industrial capitalism since the industrial revolution*. Routledge, 2014.

[77] R. MacDonald and C. Howat. Data reconciliation and parameter estimation in plant performance analysis. *AIChE journal*, 34(1):1–8, 1988.

[78] H. E. McGannon, H. H. Uhlig, E. Aguilar, A. Lacaton, J. P. Vassal, J. P. V. Anne Lacaton, K. Kuma, K. Kuma, M. Aguirre, P. Aguirre, et al. *The making, shaping and treating of steel*. Number 669.14. United States Steel, 1970.

[79] S. R. Meder and A. J. White. Air-cooled radiation recuperator, May 27 1969. US Patent 3,446,279.

[80] A. Mochida, K. Kudo, Y. Mizutani, M. Hattori, and Y. Nakamura. Transient heat transfer analysis in vacuum furnaces heated by radiant tube burners. *Energy conversion and management*, 38(10):1169–1176, 1997.

[81] W. R. Morrow, A. Hasanbeigi, J. Sathaye, and T. Xu. Assessment of energy efficiency improvement and co 2 emission reduction potentials in india's cement and iron & steel industries. *Journal of Cleaner Production*, 65:131–141, 2014.

[82] J. A. Moya and N. Pardo. The potential for improvements in energy efficiency and co 2 emissions in the eu27 iron and steel industry under different payback periods. *Journal of Cleaner Production*, 52:71–83, 2013.

[83] K. R. Muske and J. B. Rawlings. Model predictive control with linear models. *AIChE Journal*, 39(2):262–287, 1993.

[84] R. Myers, D. Montgomery, and C. Anderson-Cook. *Response surface methodology: process and product optimization using designed experiments*, volume 705. John Wiley & Sons, 2009.

[85] National Bureau of Statistics (NBS). China energy statistics yearbook 2011. China Statistics Press, Beijing, 2012. Accessed: 2016-06-03.

[86] E. Nederkoorn, P. Wilgen, and J. Schuurmans. Nonlinear model predictive control of walking beam furnaces. In *Proceedings of the 1st International Conference on Energy Efficiency and CO2 Reduction in the Steel Industry*, volume 2, Düsseldorf, Germany, 2011. EECR STEEL.

[87] M. Niederer, S. Strommer, A. Steinboeck, and A. Kugi. A simple control-oriented model of an indirect-fired strip annealing furnace. *International Journal of Heat and Mass Transfer*, 78:557–570, 2014.

[88] A. Pages, H. Pingaud, M. Meyer, and X. Joulia. A strategy for simultaneous data reconciliation and parameter estimation on process flowsheets. *Computers & chemical engineering*, 18:S223–S227, 1994.

[89] J. Pan, Y. Li, and D. Li. The application of computer simulation in the heat-treatment process of a large-scale bearing roller. *Journal of materials processing technology*, 122(2):241–248, 2002.

[90] V. Panjkovic and R. Gloss. Fast dynamic heat and mass balance model of walking beam reheat furnace with two-dimensional slab temperature profile. *Ironmaking & Steelmaking*, 39(3):190–209, 2012.

[91] N. Pardo and J. A. Moya. Prospective scenarios on energy efficiency and co 2 emissions in the european iron & steel industry. *Energy*, 54: 113–128, 2013.

[92] J. Pellegrino, N. Margolis, M. Justiniano, M. Miller, and A. Thekdi. Energy use, loss and opportunities analysis. Technical report, Energetics, Incorporated and E3M, Incorporated, Columbia, MD, 2004.

[93] H. Pike Jr and S. Citron. Optimization studies of a slab reheating furnace. *Automatica*, 6(1):41–50, 1970.

[94] D. M. Prata, E. L. Lima, and J. C. Pinto. Simultaneous data reconciliation and parameter estimation in bulk polypropylene polymerizations in real time. In *Macromolecular Symposia*, volume 243, pages 91–103. Wiley Online Library, 2006.

[95] D. M. Prata, M. Schwaab, E. L. Lima, and J. C. Pinto. Nonlinear dynamic data reconciliation and parameter estimation through particle

swarm optimization: Application for an industrial polypropylene reactor. *Chemical Engineering Science*, 64(18):3953–3967, 2009.

[96] S. J. Qin and T. A. Badgwell. A survey of industrial model predictive control technology. *Control engineering practice*, 11(7):733–764, 2003.

[97] X. Qin and Y.-H. Yang. Estimating parameters for procedural texturing by genetic algorithms. *Graphical Models*, 64(1):19–39, 2002.

[98] H. Ramamurthy, S. Ramadhyani, and R. Viskanta. A thermal system model for a radiant-tube continuous reheating furnace. *Journal of materials engineering and performance*, 4(5):519–531, 1995.

[99] J. B. Rawlings and D. Q. Mayne. *Model predictive control: Theory and design*. Nob Hill Pub., 2009.

[100] S. N. Rea. Rapid method for determining concentric cylinder radiation view factors. *AIAA Journal*, 13(8):1122–1123, 1975.

[101] J. Richalet, A. Rault, J. Testud, and J. Papon. Model predictive heuristic control: Applications to industrial processes. *Automatica*, 14(5):413–428, 1978.

[102] C. Roberts. Effect of carbon on the volume fractions and lattice parameters of retained austenite and martensite. *Trans. AIME*, 197(2):203–204, 1953.

[103] N. Rosenberg. The direction of technological change: inducement mechanisms and focusing devices. *Economic development and cultural change*, 18(1):1–24, 1969.

[104] F. Roters, P. Eisenlohr, L. Hantcherli, D. D. Tjahjanto, T. R. Bieler, and D. Raabe. Overview of constitutive laws, kinematics, homogenization and multiscale methods in crystal plasticity finite-element modeling: Theory, experiments, applications. *Acta Materialia*, 58(4):1152–1211, 2010.

[105] A. Schack. Metallic recuperators. *Waste heat recovery. London; Chapman and Hall Ltd*, pages 107–116, 1961.

[106] H. Schubert. The steel industry. *A History of Technology*, 5:53–57, 1958.

[107] C. Scruby and B. Moss. Non-contact ultrasonic measurements on steel at elevated temperatures. *NDT & E International*, 26(4):177–188, 1993.

[108] D. Seborg, T. Edgar, and D. Mellichamp. *Process dynamics & control*. John Wiley & Sons, 2004.

[109] D. E. Seborg, D. A. Mellichamp, T. F. Edgar, and F. J. Doyle III. *Process dynamics and control*. John Wiley & Sons, 2010.

[110] H. Sharma, A. Kumar, and V. Goel. Performance model of metallic concentric tube recuperator with counter flow arrangement. *Heat and mass transfer*, 46(3):295–304, 2010.

[111] H. Sharma, A. Kumar, et al. Performance analysis of metallic concentric tube recuperator in parallel flow arrangement. *International Journal of Heat and Mass Transfer*, 55(25):7760–7771, 2012.

[112] H. Sharma, A. Kumar, S. Khurana, et al. A review of metallic radiation recuperators for thermal exhaust heat recovery. *Journal of Mechanical Science and Technology*, 28(3):1099–1111, 2014.

[113] Sheĭ. *High temperature equipment*.

[114] D. B. Skalak. Prototype and feature selection by sampling and random mutation hill climbing algorithms. In *Proceedings of the eleventh international conference on machine learning*, pages 293–301, 1994.

[115] W. F. Smith and J. Hashemi. *Foundations of materials science and engineering*. McGraw-Hill, 2011.

[116] G. Speich and W. Leslie. Tempering of steel. *Metallurgical Transactions*, 3(5):1043–1054, 1972.

[117] A. Steinboeck, D. Wild, T. Kiefer, and A. Kugi. A mathematical model of a slab reheating furnace with radiative heat transfer and non-participating gaseous media. *International Journal of Heat and Mass Transfer*, 53(25):5933–5946, 2010.

[118] A. Steinboeck, K. Graichen, and A. Kugi. Dynamic optimization of a slab reheating furnace with consistent approximation of control variables.

Control Systems Technology, IEEE Transactions on, 19(6):1444–1456, 2011.

[119] A. Steinboeck, D. Wild, and A. Kugi. Nonlinear model predictive control of a continuous slab reheating furnace. *Control Engineering Practice*, 21 (4):495–508, 2013.

[120] E. Stones, K. Ferland, and M. Noack. Industrial efficiency. Technical report, NPC Global Oil and Gas Study, 2007.

[121] A. P. Sutton and R. W. Balluffi. Interfaces in crystalline materials. 1995.

[122] Y. Tang, J. Laine, T. Fabritus, and J. Harkki. Different methods obtained by PHOENICS simulation to improve the performance of pusher-type steel slab reheating furnace. Oulu University, 2010.

[123] A. Thekdi. Energy efficiency improvement opportunities in process heating for the forging industry. Canton, NY, 2010. E3M.

[124] K.-E. Thelning. *Steel and its heat treatment*. Butterworth-Heinemann, Oxford, UK, 2013.

[125] R. Tibshirani. Regression shrinkage and selection via the lasso. *Journal of the Royal Statistical Society. Series B (Methodological)*, pages 267–288, 1996.

[126] C. Tichi. *Shifting gears: Technology, literature, culture in modernist America*. UNC Press Books, 1987.

[127] M. Tiwari, A. Mukhopadhyay, and D. Sanyal. Process modeling for control of a batch heat treatment furnace with low NO x radiant tube burner. *Energy conversion and management*, 46(13):2093–2113, 2005.

[128] G. E. Totten. *Steel heat treatment: metallurgy and technologies.* crc Press, Boca Raton, FL, 2006.

[129] D. Triebl, C. Spijker, H. Raupenstrauch, A. Jarosik, and G. Angeli. Cfd-simulation eines direkt befeuerten ofens zur vorbehandlung feuerverzinkter stahlbänder. *BHM Berg-und Hüttenmännische Monatshefte*, 159(7): 310–311, 2014.

[130] C. Tso and S. Mahulikar. View factors between finite length rings on an interior cylindrical shell. *Journal of thermophysics and heat transfer*, 13 (3):375–379, 1999.

[131] United States Energy Information Administration. Monthly energy review November 2014. Accessed Dec 15, 2014, 2014.

[132] G. Van Ditzhuijzen, D. Staalman, and A. Koorn. Identification and model predictive control of a slab reheating furnace. In *Control Applications, 2002. Proceedings of the 2002 International Conference on*, volume 1, pages 361–366. IEEE, 2002.

[133] V. Viswanathan, R. Davies, and J. Holbery. Opportunity analysis for recovering energy from industrial waste heat and emissions. Pacific Northwest National Laboratory, 2005.

[134] A. Wächter and L. Biegler. On the implementation of an interior-point filter line-search algorithm for large-scale nonlinear programming. *Mathematical programming*, 106(1):25–57, 2006.

[135] H. Wadley, S. Norton, F. Mauer, B. Droney, E. Ash, and C. Sayers. Ultrasonic measurement of internal temperature distribution [and discussion]. *Philosophical Transactions of the Royal Society of London A: Mathematical, Physical and Engineering Sciences*, 320(1554):341–361, 1986.

[136] World Steel Association (WSA). Steel statistical yearbook. `http://www.worldsteel.org/statistics/`, 2014. Accessed: 2016-06-03.

[137] World Steel Association (WSA). Steel statistical yearbook. `http://www.worldsteel.org/statistics/`, 2015. Accessed: 2016-08-01.

[138] E. Worrell, L. Price, and N. Martin. Energy efficiency and carbon dioxide emissions reduction opportunities in the us iron and steel sector. *Energy*, 26(5):513–536, 2001.

[139] S. Xuegang, Y. Chao, and C. Yihui. Dynamic modeling of reheat-furnace using neural network based on pso algorithm. In *Mechatronics and Automation, 2009. ICMA 2009. International Conference on*, pages 3097–3101. IEEE, 2009.

[140] Y. Yang and Y. Lu. Development of a computer control model for slab reheating furnaces. *Computers in Industry*, 7(2):145–154, 1986.

[141] Y. Yang and Y. Lu. Dynamic model based optimization control for reheating furnaces. *Computers in industry*, 10(1):11–20, 1988.

[142] S. Yonekura. The japanese iron and steel industry, 1850-1990: continuity and discontinuity st martin's press. *New York*, 1994.

[143] N. Yoshitani, T. Ueyama, and M. Usui. Optimal slab heating control with temperature trajectory optimization. In *Industrial Electronics, Control and Instrumentation, 1994. IECON'94., 20th International Conference on*, volume 3, pages 1567–1572. IEEE, 1994.

[144] B. Zhang, Z. Chen, L. Xu, J. Wang, J. Zhang, and H. Shao. The modeling and control of a reheating furnace. In *American Control Conference, 2002. Proceedings of the 2002*, volume 5, pages 3823–3828. IEEE, 2002.

Vita

Hari Sai Ganesh's ancestral village is in Kanyakumari, Tamil Nadu, the southernmost tip of peninsular India. He was born and raised in Thiruvananthapuram, also known as Trivandrum, the capital city of the southern Indian state of Kerala. He did his schooling (3rd-12th) in a central government school: Kendiya Vidyalaya Army Cantt., Pangode, Trivandrum. He received his B.Tech. in chemical engineering degree from Amrita School of Engineering, Coimbatore in 2011 and M.Sc.(Engg.) in chemical engineering degree from the Indian Institute of Science, Bangalore in 2014, where he worked with Dr. Sudeep Punnathanm. He then moved to Austin to start working towards a Ph.D. degree in the McKetta Department of Chemical Engineering, University of Texas at Austin under the supervision of Drs. Michael Baldea and Thomas F. Edgar.

Permanent address: harisaiganesh2000@gmail.com

This dissertation was typeset with LaTeX[†] by the author.

[†]LaTeX is a document preparation system developed by Leslie Lamport as a special version of Donald Knuth's TeX Program.